Alternative Materials for Next-Generation Transistors:

High-k/Ge-based MOSFET

by

CHIEN-LAN HSUEH

A dissertation submitted to the

Graduate School-New Brunswick

Rutgers, The State University of New Jersey

in partial fulfillment of the requirements

for the degree of

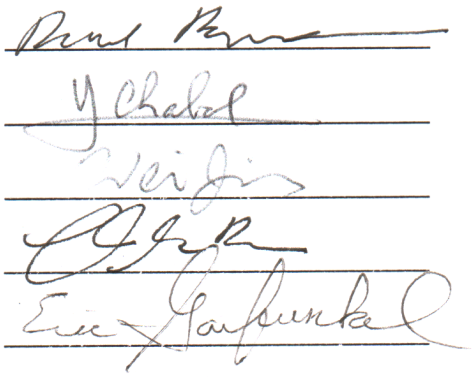
Doctor of Philosophy

Graduate Program in Physics and Astronomy

written under the direction of

Professor Eric Garfunkel

and approved by



New Brunswick, New Jersey

January, 2008

ABSTRACT OF THE DISSERTATION

Alternative Materials for Next-Generation Transistors:

High-k/Ge-based MOSFET

By CHIEN-LAN HSUEH

Dissertation Director:

Professor Eric Garfunkel

Electronic devices that make up 99% of the computer processor and memory market are based on silicon (semiconductor) and silicon dioxide (insulator) technology. Unfortunately the key transistor gate stack structure within the “traditional” technology has reached an intrinsic physical scaling limit; the ultrathin gate oxide, already at 1nm thickness, cannot be made thinner without resulting in an intolerably high leakage current and reduced drive current. This limitation can be avoided by replacing the thin gate dielectric with a thicker film of an alternative material with a permittivity higher than that of SiO_2, an accomplishing that has been realized in production just as this thesis goes to press. To further increase device performance, replacing the Si semiconductor with germanium as an alternative channel material is an attractive option for its high mobility and narrow band gap. However, the lack of a stable insulating oxide with high quality electrical properties prevents the fabrication of competitive Ge-based metal oxide semiconductor field effect transistors (MOSFETs).

This dissertation reports the study of potential future-generation transistors with high-k dielectrics (HfO_2 and Al_2O_3) on Ge substrates. A brief review of current research and development is first given followed by an introduction of the thin film characterization techniques used in this work. Various cleaning treatments as well as surface passivation methods using wet chemistry have been investigated on Ge substrates. Next, thin high-k dielectric films of HfO_2 and Al_2O_3 have been deposited on Ge using atomic layer deposition (ALD). ALD permits films to be grown with monolayer control and excellent film conformality.

Physical, chemical and electrical characterization has been performed on the multilayer film structures. Optimization of the film growth has been developed and we have demonstrated high quality with Au/HfO_2/Ge nMOS devices. Capacitance-voltage electrical measurements show that sulfur passivation methods on Ge greatly decrease the interface state density and improve the device electrical properties. The same improvements have also been observed on the similarly processed Ge-based MOS capacitors with Al_2O_3 dielectric layers.

In memory of my grand mother

Feng-Lan Hsueh

(1937 - 2007)

“When being normal becomes a luxury,

the world is so distorted that I can barely breath.

Only heavenly love can provide the true guidelines,

that help me no longer hide and cry.”

Acknowledgement

I could not have had any better thesis adviser than Prof. Eric Garfunkel. Without his generousness and encouragement, this dissertation would not have been possible. He has not only guided me with his knowledge and wisdom, but also shown me what a true scholar should be.

There is no way for me to come this far without help from people I met these years. Some gave me essential assistance in my graduate study as well as my daily life while some shared with me their valuable wisdom and life experience. I can never express my appreciation enough to all of them. A better way I have figured to return these favors is to pay them forward to people I will meet in the journey of my life while keeping in mind that I am what I am, and I can do what I can do today because of these nice people.

I also owe a lot to my family for their long-lasting patient and support, especially my wife and my lovely little girls who have always enriched my life with their endless trust and love.

Chien-Lan Hsueh

Dec 26, 2007

Abbreviation

AES	Auger Electron Spectroscopy
AFM	Atomic Force Microscopy
ALD	Atomic Layer Deposition
ALE	Atomic Layer Epitaxy
ARPES	Angular Resolved Photoelectron Spectroscopy
BE	Binding Energy
CMOS	Complementary Metal Oxide Semiconductor
CNL	Charge Neutrality Level
CV	Capacitance Voltage
CVD	Chemical Vapor Deposition
DAQ	Data Acquisition
DIW	De-ionized Water
DRAM	Dynamic Random Access Memory
EELS	Electron Energy Lose Spectroscopy
EOT	Equivalent Oxide Thickness
ESCA	Electron Spectroscopy for Chemical Analysis
FCC	Face Centered Cubic
FT-IR	Fourier Transform Infrared Spectroscopy
FWHM	Full Width at Half Maximum
ITRS	International Technology Roadmap for Semiconductors
KE	Kinetic Energy
LCD	Liquid Crystal Display

LED	Light Emitting Diode
LEIS	Low Energy Ion scattering
MEIS	Medium Energy Ion Scattering
ML	Monolayer
MOS	Metal Oxide Semiconductor
MOSFET	Metal Oxide Semiconductor Field Effect Transistors
NRA	Nuclear Reaction Analysis
OLED	Organic Light Emitting Device
PC	Personal Computer
PDA	Post Deposition Annealing
PVD	Physical Vapor Deposition
RBS	Rutherford Backscattering Spectroscopy
RMS	Root Mean Square
RTA	Rapid Thermal Annealing
TFEL	Thin Film Electroluminescence
TMA	Trimethylaluminium
UHV	Ultra High Vacuum
USB	Universal Serial Bus
UV	Ultraviolet
VLSI	Very Large Scaled Integrated Circuit
XPS	X-ray Photoelectron Spectroscopy

Table of Contents

Title Page i

Abstract ii

Acknowledgement v

Abbreviation vi

Table of Contents viii

List of Tables xiii

List of Figures xiv

Chapter 1 Introduction 1

Section 1.1 Scaling in CMOS Technology 1

1.1.1 Moore's Law 1

1.1.2 Origins of MOSFET Scaling 2

Section 1.2 The Need for Alternative Gate Dielectrics 5

1.2.1 Reduction of Leakage Current with High-k Dielectric 5

1.2.2 Effective Oxide Thickness 7

1.2.3 Guidelines for Choosing High-k Dielectric 7

Section 1.3 Germanium-based MOSFET 9

1.3.1 Germanium 9

Section 1.4 Passivation of Germanium 12
1.4.1 Passivation with Hydrogen 13
1.4.2 Passivation with Nitrogen 14
1.4.3 Passivation with Chlorine 14
1.4.4 Passivation with Sulfur 15
Section 1.5 Objectives of This Study 15
Section 1.6 Structure of the Dissertation 16
Section 1.7 Reference 17
Chapter 2 Thin Film Characterization Techniques 21
Section 2.1 X-ray Photoelectron Spectroscopy 21
2.1.1 Principle of XPS 22
2.1.2 Atomic Sensitivity Factor 25
2.1.3 Depth Profiling Using XPS 26
Section 2.2 Rutherford Backscattering Spectroscopy 30
2.2.1 Kinematics of RBS 31
2.2.2 Scattering Cross Section and Areal Density of Target Atoms 34
2.2.3 Depth Profiling Using RBS 36
2.2.4 Channeling 39
2.2.5 SIMNRA 40

Section 2.3 AFM 41
2.3.1 Principle of AFM 41
2.3.2 Quantification of Surface Roughness 42
Section 2.4 FT-IR 43
2.4.1 Absorption Spectroscopy 43
2.4.2 Infrared Spectroscopy 45
2.4.3 FT-IR 46
Section 2.5 Reference 49
Chapter 3 Preparation of Germanium Substrates 51
Section 3.1 Cleaning of Germanium Substrates 51
3.1.1 Native Oxides 52
3.1.2 Removal of Native Oxide and Carbon 55
3.1.3 Protective Chemical Oxides 60
Section 3.2 Passivation on Germanium Substrates 65
3.2.1 Passivation with Hydrogen 66
3.2.2 Passivation with Sulfur 69
Section 3.3 Reference 76
Chapter 4 Atomic Layer Deposition of High-k Dielectrics 78
Section 4.1 Atomic Layer Deposition 78

4.1.1 Advantages of ALD Processes 79
Section 4.2 Metal Precursors 84
4.2.1 Precursors for Al_2O_3 85
4.2.2 Precursors for HfO_2 87
4.2.3 Precursors for ZrO_2 91
Section 4.3 Oxygen Sources 93
Section 4.4 ALD System 95
Section 4.5 Experimental Results of ALD Film Growths 98
4.5.1 ALD of Al_2O_3 98
4.5.2 ALD of HfO_2 101
Section 4.6 Reference 104
Chapter 5 High-k/Ge MOS Capacitors 111
Section 5.1 C-V Measurements 111
5.1.1 Energy Band Diagrams of MOS Stacks and Flat-Band Voltage 111
5.1.2 C-V Curves of MOS Capacitors and Threshold Voltage 118
Section 5.2 Effects of Trapped Charges on C-V Curves 124
5.2.1 Shifts of Flat-Band Voltage and Hysteresis of C-V Curves 124
5.2.2 Determination of Interface Traps 126
Section 5.3 Experimental Results 127

5.3.1 HfO_2/Ge 128

5.3.2 Al_2O_3/Ge 133

Section 5.4 Reference 135

Chapter 6 Conclusion 136

Curriculum Vista 139

List of Tables

Table 1-1: Properties of Si and Ge at 300K. 11

Table 2-1: Values of XPS atomic sensitivity factors used in this work [7]. 26

Table 3-1: Comparison of XPS atomic concentration (%) of S-passivated samples with different cleaning. 75

Table 4-1: List of common Al precursors used in ALD. 86

Table 4-2: List of common Hf precursors used in ALD. 90

Table 4-3: List of common Zr precursors used in ALD. 92

Table 5-1: Comparison of the C-V measurements on Au/HfO_2/p-Ge(100) capacitors. 132

List of Figures

Figure 1-1: Number of transistors within a die over time [10]..... 2

Figure 1-2: The structure of n-channel MOSFET..... 3

Figure 1-3: Equivalent oxide thickness scaling in International Technology Roadmap for Semiconductors [1]. 5

Figure 1-4: Suppression of the direct tunnel leakage current by introducing a high-k gate oxide. 6

Figure 1-5: Bandgap as a function of dielectric constant for several alternative high-k dielectrics [43]. 9

Figure 1-6: Bandgap and lattice constants of the most relevant semiconductor materials related to germanium. 10

Figure 2-1: Schematic drawing of XPS system..... 22

Figure 2-2: Energy-level diagrams showing the electron transitions in XPS..... 23

Figure 2-3: Comparison of XPS (a) and RBS (b) depth profiling on a Ge/SiO_2/Si sample annealed in O_2 [9]..... 27

Figure 2-4: Mean free path of photoelectrons in solid [10]..... 28

Figure 2-5: Geometry of angle resolved XPS setup. 29

Figure 2-6: Rutherford Back Scattering Spectroscopy (RBS). 31

Figure 2-7: The position of RBS peaks reflects the mass difference of targets. . 32

Figure 2-8: Kinematic factor for He+ ions backscattering from different masses at different scattering angles..... 33

Figure 2-9: Kinematic factor for He+ ions backscattering from different targets at different scattering angles. 33
Figure 2-10: The position of RBS peaks reflects the depth distribution of targets. 37
Figure 2-11: Channeling is the guided motion of ions in the open channels of a crystal target. 39
Figure 2-12: Random and channeled spectrum of 270 keV He^+ incident on 25Å SiO_2/Si along <111> [21]. 40
Figure 2-13: A schematic drawing of an AFM system. 42
Figure 2-14: Some normal modes of $–CH_2$ molecular vibrations. The + and – symbols indicate a movement out of and into the plane of the paper respectively. 46
Figure 2-15: Schematic drawing of components of FT-IR and the Michelson interferometer. 47
Figure 3-1: Ge 3d XPS spectrum from as-received Ge(100) wafers. 53
Figure 3-2: Ge 3d XPS spectra of an as-received Ge(100) sample at different take-off angles. 54
Figure 3-3: Calculation of the thickness of the oxide overlayer on Ge(100). 55
Figure 3-4: Ge 3d XPS spectrum from a Ge(100) wafer after DIW rinsing. 56
Figure 3-5: Ge 3d XPS spectrum from a Ge(100) wafer after the 10% HF etching. 57
Figure 3-6: C 1s XPS spectra from as-received, DIW-rinsed and HF-etched Ge(100) samples. 58

Figure 3-7: Ge 3d XPS spectra as a function of annealing temperature [22]..... 59
Figure 3-8: C 1s (left) and O 1s (right) XPS spectra from Ge(100) after UV/ozone exposure and annealing [3]..... 61
Figure 3-9: Ge 3d XPS spectrum from a Ge(100) sample with a chemical oxide formed by concentrated H_2O_2. 62
Figure 3-10: Ge 3d XPS spectrum from a Ge(100) sample with chemical oxide formed by H_2SO_4/H_2O_2. 63
Figure 3-11: Comparison of C 1s XPS peaks with different cleaning methods... 63
Figure 3-12: Intensity changes of C 1s XPS peaks before and after the removal of chemical oxide. 64
Figure 3-13: Etching and chemical oxidization on as-received Ge wafers..... 65
Figure 3-14: FT-IR spectra of a H-terminated Ge(100) sample (blue) vs. H_2SO4/H_2O_2-treated Ge sample followed by a DIW rise (red) using as-received Ge samples as a reference. 66
Figure 3-15: FT-IR spectra of HF-etched Ge(100) after a different wet chemical cleaning is applied. 68
Figure 3-16: FT-IR spectra to show the stability of H-terminated Ge(100) in air and in N2. 69
Figure 3-17: Molecular structure of thioacetamide and thiourea..... 70
Figure 3-18: S 2p XPS spectra from Ge(100) treated in $(NH_4)_2S$, thioacetamide and thiourea solution. 70
Figure 3-19: Ge 3d XPS spectrum from a $(NH_4)_2S$-treated Ge(100) sample. 71

Figure 3-20: Ge 2p XPS spectrum from a S-passivated H_2SO_4/H2O2-treated Ge(100) sample. The inset shows the comparison of the same sample (red line) with an as-received sample (blue line). 73
Figure 3-21: S 2p and C 1s XPS spectra from S-passivated Ge samples with different cleaning pretreatments. 73
Figure 4-1: Schematic drawing of one ALD cycle (adapted from [12]). 80
Figure 4-2: Different types of growth rate vs. precursor pulse time at a constant temperature [12]. 81
Figure 4-3: Factors that prevent full surface coverage of chemisorption: (a) steric hindrance of the ligands, and (b) number of reactive surface sites [10]. 82
Figure 4-4: Factors limiting the self-limiting growth at various temperatures [12]. 83
Figure 4-5: Molecular structure of metal halide. 85
Figure 4-6: Molecular structures of metal alkyls. 87
Figure 4-7: Molecular structures of metal alkyamides. 89
Figure 4-8: The integrated XPS system with ALD and metallization chambers. . 95
Figure 4-9: The schematic drawing of the ALD system. 97
Figure 4-10: RBS random scattering spectrum of Al_2O_3 of the same thickness on Si (left) and Ge (right). 99
Figure 4-11: RBS spectra of Al_2O_3 on ITO (left) and Kapton (right). 100
Figure 4-12: Film thickness of Al_2O_3 vs. number of ALD cycles. 101
Figure 4-13: Random scattering RBS spectrum of HfO_2/GaAs. 102

Figure 4-14: Film thickness of HfO_2 vs. number of ALD cycles. 102
Figure 4-15: Random scattering RBS spectrum of HfO_2/Ge (left) and HfO_2/Si (right). 103
Figure 4-16: Film thickness of HfO_2 on Ge (left) and on Si (right) vs. number of ALD cycles. 103
Figure 5-1: Energy band diagram of an ideal MOS capacitor [1]. 112
Figure 5-2: Space-charge density as a function of the surface potential for p-type Ge with $N_A=2.5x10^{22}$ cm^{-3} at room temperature. 114
Figure 5-3: Band diagrams for an ideal p-substrate MOS structure in different surface-charge conditions (adapted from [1-3]). 115
Figure 5-4: Band diagrams of MOS (a) at separation, (b) at equilibrium and (c) in flat-band condition [3]. 116
Figure 5-5: (a) Charges represented as a sheet of effective charge [2]; (b) interface traps [7]. 118
Figure 5-6: Equivalent circuits including interface-trapped effects (a), at high (b) and low frequency (c). 119
Figure 5-7: Band diagram and distribution of charge density in inversion [1, 3]. 121
Figure 5-8: C-V curve for an ideal p-substrate MOS capacitor at high (HF) and low (LF) frequency [7]. 122
Figure 5-9: C-V curve with nonzero work function difference (dashed) and trapped charges (dotted) [7]. 125
Figure 5-10: Hysteresis of a C-V curve [7]. 126

Figure 5-11: C-V curves at high (solid line) and low (dotted line) frequencies [7]. 127

Figure 5-12: Schematic drawing of the C-V measurement setup. 128

Figure 5-13: C-V curves of a Au dot capacitor with 4 nm HfO_2 on HF-last p-Ge(100)..... 129

Figure 5-14: C-V curves of a Au dot capacitor with 4 nm HfO_2 on HF/DIW/H_2O_2-treated S-passivated p-Ge(100)..... 130

Figure 5-15: C-V curves of a Au dot capacitor with 4 nm HfO_2 on H_2SO_4/H_2O_2 oxidized, HF-etched S-passivated p-Ge(100). 131

Figure 5-16: C-V curves of a Au dot capacitor with 4 nm HfO_2 on H_2SO_4/H_2O_2 oxidized, S-passivated p-Ge(100)..... 132

Figure 5-17: C-V curves of Al dot capacitors with 7.7 nm HfO_2 on S-passivated n-Ge(100) [12]..... 133

Figure 5-18: C-V curves of Au/Al_2O_3/p-Ge(100) with (right) and without (left) the sulfur passivation. 134

Chapter 1 Introduction

Section 1.1 Scaling in CMOS Technology

The key to the growth of the microelectronics industry during the last 30 years has been the drive to ever smaller dimensions using the principles of “device scaling”. The basic idea of scaling is to reduce the dimensions of electronic devices for computation and memory in order to increase the density and speed of integrated circuits, and decrease the cost and power consumption per unit function.

1.1.1 Moore’s Law

The semiconductor industry has been growing and prospering continuously since the early 1970s. Each month smaller and faster electronic products appear on the market due to of the rapid growth of semiconductor technology. In order to satisfy the demand for faster circuits, higher packing density and lower power dissipation, the dimensions of metal–oxide–semiconductor field-effect transistor (MOSFET) devices (complementary MOS, CMOS, in particular) are being scaled down according to the International Technology Roadmap for Semiconductors (ITRS) [1], a guidebook for the field.

Gordon Moore, one of the founders of Intel predicted that the number of transistors on a chip would quadruple every 36 months, later updating his prediction to quadrupling every 24 months [2, 3]. This prediction is known as

Moore's Law. The number of transistors in an integrated circuit was about 2000 at the time he made his observation. By the end of the current decade, one billion transistors (per die) will be achieved. Figure 1-1 illustrates this for a range of processor families [4-9].

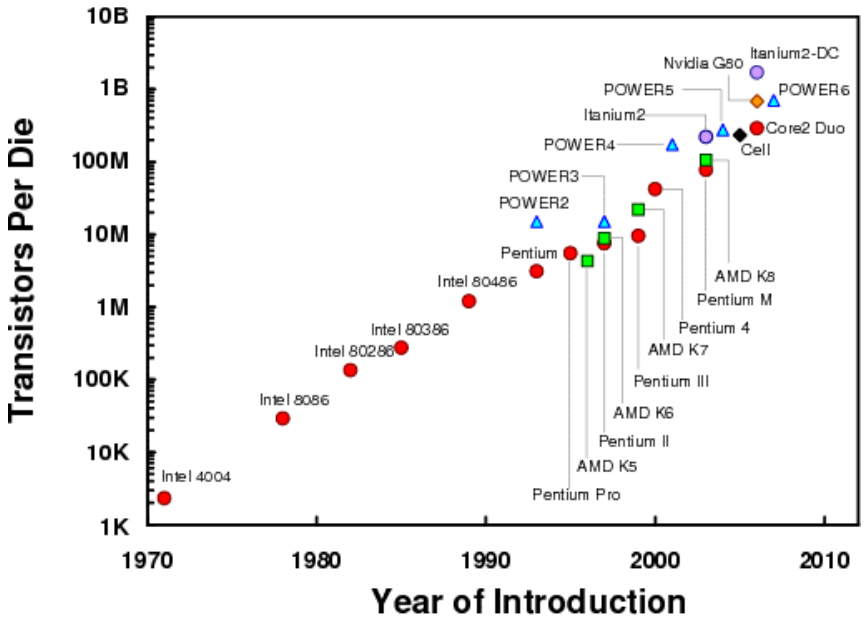


Figure 1-1: Number of transistors within a die over time [10].

1.1.2 Origins of MOSFET Scaling

Figure 1-2 shows the structure of an n-channel MOSFET. In the dorminant Si technology, the main dielectric material of the MOS capacitor, SiO_2 (recently SiON), is sandwiched between doped poly-silicon (the gate) and a Si substrate. While applying a positive bias on the gate, an electric field across the dielectric layer will draw electrons into the region just below the dielectric, forming a conductive channel, the n-channel, and switch on the device.

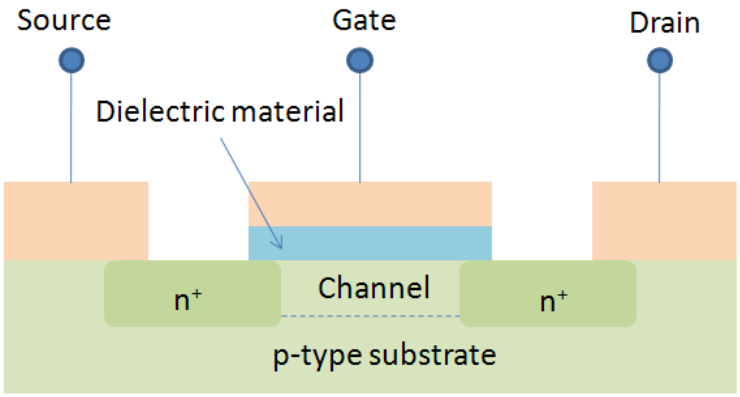


Figure 1-2: The structure of n-channel MOSFET.

The drain-source current for a long-channel MOSFET operating in the saturation region is given by,

$$I_{ds} = \frac{1}{2}\mu C_{ox}\frac{W}{L}\left(V_{gs} - V_t\right)^2$$

where μ is the channel mobility, W and L are the width and length of the channel region, respectively, V_{gs} is the gate-source potential, and V_t is the threshold voltage.

In order to increase the drain-source current I_{ds}, one can optimize the device by (1) reducing the length of the channel L, (2) increasing the channel mobility μ of the substrate, and (3) increasing the MOS capacitance C_{ox}:

(1) Shrinking of the transistor gate length L reduces the carriers travelling distance and hence the time between source and drain; thus the drain-source current increases and the device speed increases. Reducing the gate oxide thickness along with the channel length L also helps to maintain the gates electrode control over deleterious “short channel” effects [11].

(2) Replacing silicon with a higher channel-mobility semiconductor to increase μ will be discussed in detail in Section 1.3.

(3) The capacitance C_{ox} of a MOS capacitor, essentially a parallel plate capacitor, is given as,

$$C_{ox} = k\varepsilon_0 \frac{A}{t_{ox}}$$

where k is the relative permittivity of the gate oxide (dielectric constant), $\varepsilon_0$is the permittivity of vacuum, A is the capacitor area, and t_{ox} is the gate oxide physical thickness. Either reducing the thickness of the gate oxide layer t_{ox} or using dielectric materials with a higher dielectric constant k, will helps increase the gate capacitance C_{ox}. This allows the gate potential to modulate more channel charge and is especially important as the supply voltage scales down.

Much of the progress in Si microelectronics has been driven by the ability to continually shrink the lateral (L and W) and vertical t_{ox} dimensions of the MOSFET to increase performance and decrease die area, a process referred to as scaling [12]. In order to maintain the same transistor parameters such as threshold voltage and capacitance, the shortening of the transistor channel length leads to a corresponding scaling of the gate area and gate oxide thickness [11].

To be able to follow scaling according to the ITRS, the SiO_2 film thickness used in manufacturing should be below 1nm within the next few years as shown in Figure 1-3, or a new dielectric must be used (more details in next section).

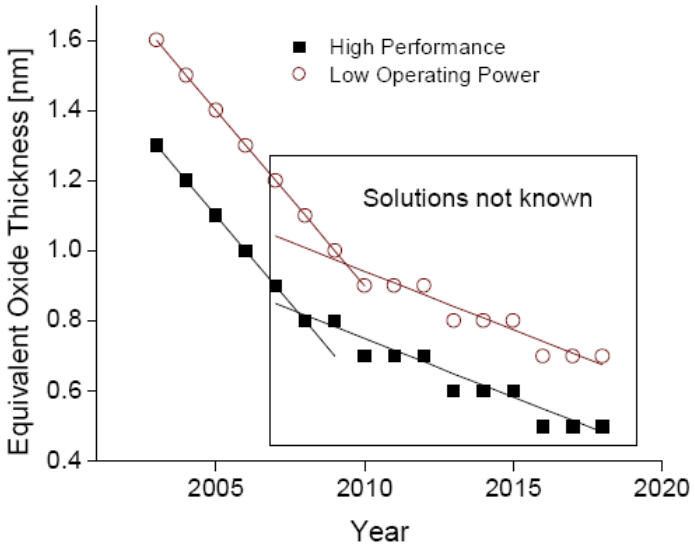


Figure 1-3: Equivalent oxide thickness scaling in International Technology Roadmap for Semiconductors [1].

Section 1.2 The Need for Alternative Gate Dielectrics

Scaling of traditional CMOS technology with SiO_2 results in a dramatic increase in leakage current and degrades the device performance. Higher permittivity (high-k) dielectric materials and metal electrodes are now considered as the best way to solve the leakage problem while continuing to scale devices.

1.2.1 Reduction of Leakage Current with High-k Dielectric

Traditional scaling, which has guided, and in some sense driven the semiconductor industry for the last 30 years, is reaching some fundamental limits when using standard material building blocks of the CMOS process [1, 13-15].

One of the biggest challenges in the traditional process shrinking approach is the SiO_2 gate insulator.

Thermally grown oxide (SiO_2) has been used as a gate dielectric since the introduction of MOSFET devices. Because silicon dioxide has high compatibility with Si substrate, simple grow-process on Si and excellent insulator properties, Si has been the leading semiconductor for decades. However, as this thin SiO_2 gate oxide of only a few atomic layers is scaled below 1.5 nm, it permits a dramatic increase in the direct tunnel leakage current through the insulator and reduces the drive current. Gate leakage current reduces the on-off current ratio of the device, creating heat which could possibly lead to a break-down of the device. This causes the fundamental limitation to further scaling.

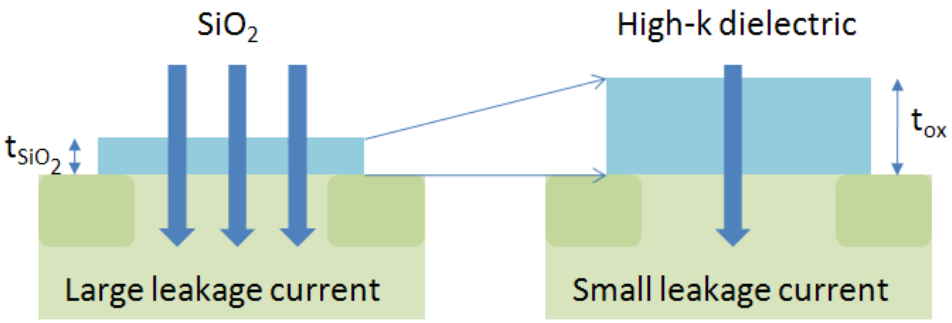


Figure 1-4: Suppression of the direct tunnel leakage current by introducing a high-k gate oxide.

The high leakage current and the inadequate reliability of the SiO_2 layer less than ~1.5 nm thick suggests a need for a replacement of SiO_2 with a thicker dielectric material with a higher permittivity k. High k dielectrics reduce the leakage current by providing a thicker film while electrically behaving as a thinner

equivalent dielectric as illustrated in Figure 1-4. Therefore high-k materials are excellent candidates for replacements to the traditional SiO_2 gate oxide.

1.2.2 Effective Oxide Thickness

By assuming the same capacitance is achieved using SiO_2 as a dielectric, the Equivalent Oxide Thickness (EOT) of an alternative gate dielectric layer is given by:

$$EOT = t_{ox}\frac{\varepsilon_{SiO_2}}{\varepsilon} = t_{ox}\frac{3.9}{k}$$

This equation means that with a high dielectric constant, a thick gate dielectric layer gives an appropriate capacitance value equal to that of an equivalent thin SiO_2 layer. Usually, the gate dielectric consists of several layers, e.g. a lower-k interfacial layer and higher-k layer. In terms of EOT, the series capacitance can be written as:

$$EOT_{total} = EOT_{high-k} + \sum EOT_{low-k}$$

Any low-*k* interfacial layer contributes to the overall EOT value and thus should be minimized in order to achieve as low an EOT as is required.

1.2.3 Guidelines for Choosing High-k Dielectric

Some important properties of high-k dielectrics must meet the requirements of the ITRS in order for the next generation of MOSFET to have a successful performance. For example, in order to reduce the gate leakage

current, a dielectric constant value of 8-30, a barrier height greater than 1.0 eV between the substrate and the dielectric [16, 17] and a sufficient bandgap (>5 eV) [17] are required. If the dielectric constant is too high, a large electric field will exist along the channel edges. If the barrier height is too low, it will increase the tunneling across the gate. A general trend from Clausius-Mosotti relation is that, as the dielectric constant increases, the bandgap decreases. This leads to lower barrier heights and hence greater thermal emission and tunneling.

From a process point of view, candidates of alternative gate dielectrics must meet a set of criteria such as thermodynamic stability, interface quality, and film morphology [18]. Many dielectric materials have been investigated, but very few appear promising with respect to all the guidelines listed above. These include the group IIIB metal oxide Al_2O_3 [19-24], the group IVA metal oxides HfO_2 [25-29], ZrO_2 [30-34] and the group VA oxide Ta_2O_5 [35-37]. Oxides of binary alloys, such as $ZrAl_xO_y$ [38, 39] have also been studied because of the attempt to combine the desirable qualities of the two metal oxides while eliminating the undesirable properties of each individual material. Metal silicates such as Zr and Hf-silicates are also considered as promising materials because they exhibit high thermal stability [40-42].

Furthermore, an alternative gate dielectric should have a low oxygen diffusivity, a low density of defects and a high thermal stability with the substrate so that interfacial reactions with the adjacent layers are minimized. The requirements mentioned above limit the gate dielectric candidates to only a few (Figure 1-5), among which the oxides of Al, Hf and Zr are the most promising.

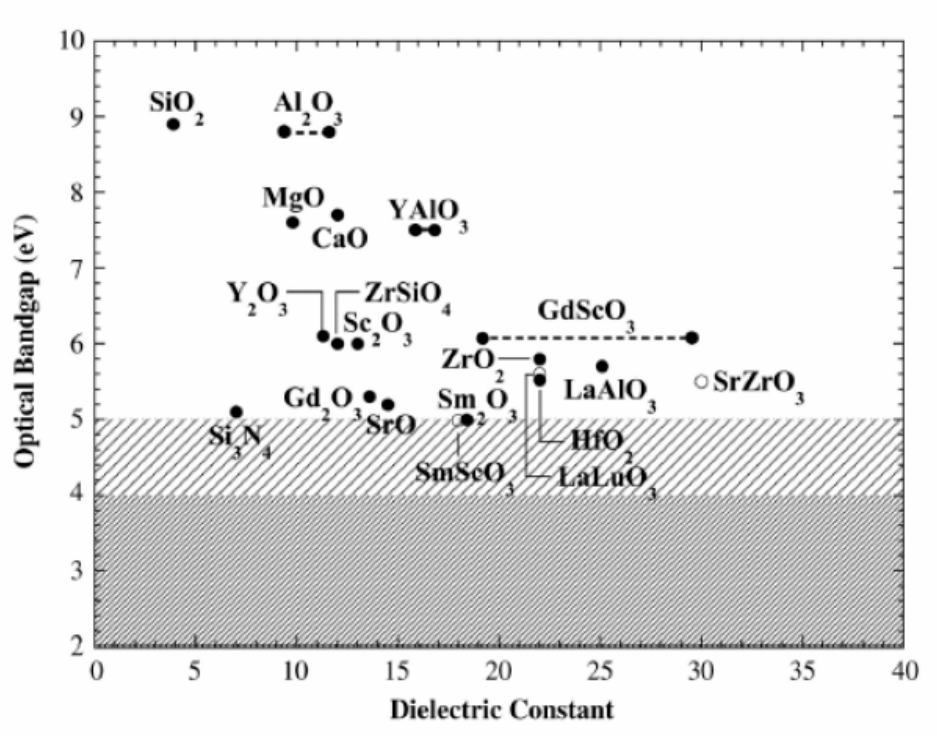


Figure 1-5: Bandgap as a function of dielectric constant for several alternative high-k dielectrics [43].

Section 1.3 Germanium-based MOSFET

Using semiconductors with high channel mobility can also improve the performance of MOSFETs by enabling faster speed and lower power dissipation. Germanium has drawn a lot of attention to replace Si for the next generation of CMOS technology, and is already used in other high performance devices.

1.3.1 Germanium

Germanium, like silicon, is a group IV element which has a diamond lattice composed of two interpenetrating face centered cubic (FCC) lattices, each

displaced 1/4 of a lattice constant in each direction from one another. Each site is tetrahedral coordinated with four other sites in the other sublattice. Among the elements of group IV, only Ge and Si are widely used as semiconductors.

The main uses for Ge are in transistors and as dopant materials in optical fibers. As substrates, Ge is also extensively used in epitaxial growth of III-V compounds. The lattice constant of non-polar Ge is 5.6461 Å at room temperature, having less than 1% difference than the polar GaAs lattice constant of 5.6537 Å. This suitable value of Ge lattice constant enables several semiconductor compounds to be grown on it without a significant strain field.

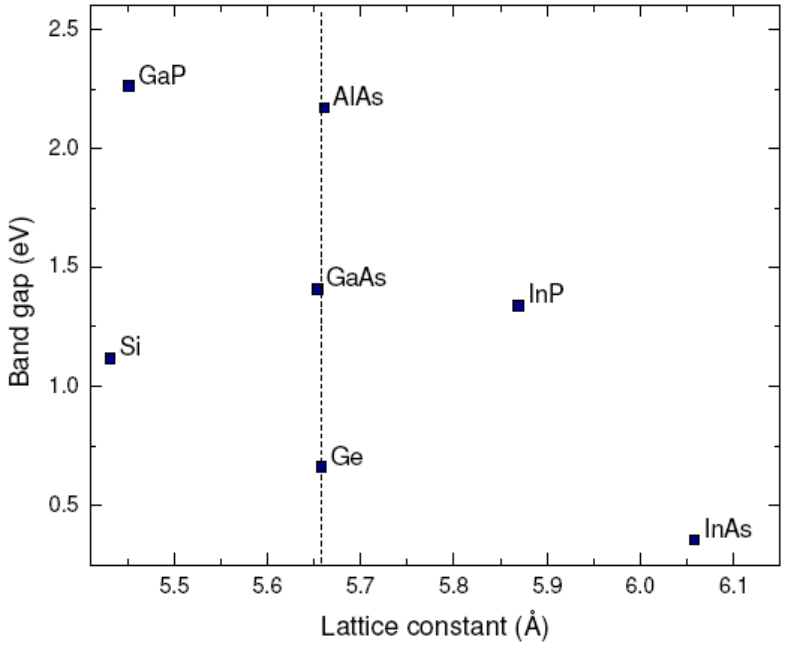


Figure 1-6: Bandgap and lattice constants of the most relevant semiconductor materials related to germanium.

Ge has been considered as a replacement channel material of Si for future high-speed CMOS technology because bulk Ge has higher electron and

hole mobilities than Si (2X higher for the electron mobility and 4X higher for the hole mobility) at room temperature. This enables more efficient source injection and shorter CMOS gate delay, and is due to the low effective electron and hole masses. Its smaller energy bandgap (~1/2X that of Si) can let Ge-based MOSFETs survive V_{DD} scaling. Interestingly, the very first transistor in 1947 was made of Ge. Unfortunately, Ge has suffered from the lack of a high quality native oxide for device applications [44]. The native germanium oxide is hygroscopic and water-soluble which hinders the processing and application of Ge CMOS devices. This is why Si was used to replace Ge as a main channel material in CMOS technology in the past thirty years.

Properties	Si	Ge
Atomic Weight	28.09	72.60
Crystal Structure	Diamond	Diamond
Density (g/cm^3)	2.328	5.3267
Lattice Constant (angstroms)	5.43095	5.64613
Dielectric Constant	11.9	16.0
Effective Density of States in the Conduction Band, Nc (cm^{-3})	2.8×10^{19}	1.04×10^{19}
Effective Density of States in the Valence Band, Nv (cm^{-3})	1.04×10^{19}	6.0×10^{18}
Electron Affinity (V)	4.05	4.0
Energy Gap at 300K (eV)	1.12	0.66
Intrinsic Carrier Concentration (cm^{-3})	1.45×10^{10}	2.4×10^{13}
Mobility (Drift) ($cm^2/V\text{-}s$) μ_n, electrons	1500	3900
Mobility (Drift) ($cm^2/V\text{-}s$) μ_p, holes	475	1900
Melting Point (deg C)	1415	937

Table 1-1: Properties of Si and Ge at 300K.

In potential future Ge-based CMOS and photo detectors, a high quality Ge-dielectric interface is essential to device performance. High-k gate dielectric MOS transistors based on Ge have been investigated in the hope that deposited high-k gate dielectrics may exhibit better electrical characteristics than the poor quality germanium oxide gate dielectric layer. High-k gate insulators made of HfO_2 [45-47], Al_2O_3 [47] and ZrO_2 [48] as well as germanium oxy-nitride [49] have recently been studied for Ge-based MOSFET devices.

Section 1.4 Passivation of Germanium

Ge, like Si, substrates are very reactive toward oxygen and other species, In part because of the dangling bonds on the surface. Surface passivation, the termination of these bonds with elements like H, N and S, helps stabilize the surface. Passivation of Ge substrates is necessary to minimize contamination of the surface. For example, without surface passivation, Ge substrates can be inert-gas ion-sputtered in order to obtain a clean Ge surface, although this degrades the surface severely by inducing damage [50, 51].

A related, in some sense more general, reason to passivate Ge surfaces is to improve the dielectric/Ge interface which greatly affects the performance of the device. When high-k materials are used as the gate dielectric on Ge, serious problems arise during processing. The most challenging one is the formation of an interfacial GeO_x layer between the high-k gate dielectric and the Ge substrate during the deposition of high-k dielectrics or post annealing processes [52]. Since

a high temperature process is required to activate dopants in the source and the drain, it can lead to unwanted reactions: (1) between the dielectric and Ge, (2) in the dielectric, (3) between the dielectric and the metal gate, and/or (4) metal diffusion through the gate dielectric and into the channel. This makes it very difficult to have the ultra thin EOTs needed in future devices. High temperatures also change the film morphology of the dielectric into crystalline or polycrystalline materials. The leakage current increases and the flatband and threshold voltages can shift due to several reasons, including the large grain boundaries associated with a polycrystalline film allowing carriers and dopants to move more easily through the material.

To summarize, an effective passivation treatment should be chemically stable, protect the substrate from unwanted oxidation and contamination, and help minimize interface or surface-induced carrier recombination. In order to achieve these, clean Ge surfaces are usually passivated by saturating the surfaces with H, N, Cl, S, or other species as discussed below.

1.4.1 Passivation with Hydrogen

One possible way to passivate Ge is to saturate dangling bonds on the surface with hydrogen. Because of the success of hydrogen passivation on Si substrates in the development of the semiconductor industry, hydrogen passivation on Ge substrates has been studied [53, 54]. Clean oxygen-free H-terminated Ge surfaces can be obtained with wet chemical treatments. However,

like H-terminated Si, the stability of H-terminated Ge is not good. Bodlaki has reported that the H-terminated Ge(111) surface is very unstable under ambient conditions [55]. Rapid absorption of hydrocarbons has also been observed on H-terminated Ge(100) [56].

1.4.2 Passivation with Nitrogen

Nitrogen addition (nitridation) is also used to improve the reliability of Ge-based MOSFETs through the formation of strong Ge-N bonds [57-60]. The nitrogen incorporation, with Ge to form a Ge oxynitride or Ge nitride layer, provides higher thermal stability and a higher dielectric constant than that of GeO_x. These nitride-based dielectrics can be used not only as a buffer layer for the growth of high-k gate dielectrics on Ge, but also as a gate insulator for Ge-based MOSFET [59-65].

1.4.3 Passivation with Chlorine

Cl-terminated Ge surfaces are prepared usually with hydrogen chloride (HCl) [66, 67]. The etching mechanism is different on Ge(100) and Ge(111) surfaces. On the Ge(111) surface, only Ge mono-chloride is formed [67]. Both Ge mono-chlorides and di-chlorides are found on Ge(100) surfaces [66]. However, the Cl-terminated Ge surfaces are not stable in air; their rapid re-oxidization is thought to be due to incomplete Cl-termination [55].

1.4.4 Passivation with Sulfur

Another promising solution is using sulfur to passivate a Ge substrate before the deposition of high-k gate dielectrics. Similar to nitridation discussed above, this sulfur passivation layer can also form a buffer layer to prevent the formation of interfacial GeOx. Experimental [68-71] and theoretical [72, 73] studies of low pressure adsorption of sulfur on clean Ge(100) have shown that the sulfur is bridge bonded to the surface Ge atoms. Furthermore, for a sulfur coverage of 1 ML, all of the Ge dangling bonds are saturated, resulting in the S/Ge(100)-1x1 surface being ideally terminated [69]. Recently, Ge surface passivation with sulfur using aqueous ammonia sulfide $(NH_4)_2S$ has been demonstrated [74-76]. The S-terminated Ge surface proves to be much more stable in air than H- and Cl-terminated Ge surfaces [55]. Compared to nitridation, sulfur passivation resulting high-k/S-Ge/Ge stacks yields a lower fixed charge and interface state density as well as higher stability [74] and lower Schottky barrier height [75], as will be discussed in more detail below.

Section 1.5 Objectives of This Study

The purpose of this work is to investigate the effects of wet chemical cleaning and sulfur passivation on Ge and show the improvements to performance of high-k dielectric Ge MOSFET, especially the lower interface trapped charges and interface state density. Device parameters will be extracted from electrical property measurements of MOSFET devices.

Section 1.6 Structure of the Dissertation

This dissertation will correlate the material properties (physical and chemical) with device electrical characterization.

Chapter 2 is a description of the surface characterization techniques used in this work.

Chapter 3 investigates the effects of different wet chemical cleaning methods on Ge and optimizes the process of sulfur passivation.

Chapter 4 describes the mechanism of atomic layer deposition used in this work for the deposition of high-k dielectrics, as well as the home-made ALD system that we built.

Chapter 5 provides a detailed introduction to capacitance-voltage measurements as an electrical characterization technique to investigate the improvements of high-k/Ge-based MOSFET with different cleaning and passivation methods on Ge surfaces.

Chapter 6 concludes the thesis and proposes future works.

Section 1.7 Reference

1. *International Technology Roadmap for Semiconductors*. Available from: http://www.itrs.net/home.html.
2. G.E. Moore, *Cramming more components onto integrated circuits.* 1965: p. 114-117.
3. G.E. Moore. *Progress in digital integrated electronics*. in *IEDM*. 1975. Washington D.C., USA.
4. L.A. Barroso, *The price of performance.* ACM Queue, 2005. **3**(7): p. 48-53.
5. N. Corporation, *NVIDIA GeForce 8800 GPU Architecture Overview.* Technical Brief TB-02787-001_v01, NVIDIA Corporation, 2006.
6. J. Friedrich, B. McCredie, N. James, et al., *Design of the POWER6 Microprocessor.* In IEEE International Solid-State Circuits Conference (ISSCC 2007), 2007.
7. M. Golden, S. Arekapudi, G. Dabney, et al., *A 2.6GHz Dual-Core 64b x86 Microprocessor with DDR2 Memory Support.* In IEEE International Solid-State Circuits Conference (ISSCC 2006), 2006.
8. R. Ronen, A. Mendelson, K. Lai, et al., *Coming challenges in microarchitecture and architecture.* Proceedings of the IEEE, 2001. **89**(3): p. 325-340.
9. M.Y. N. Sakran, M. Mehalel, J. Doweck, E. Knoll, and A. Kovacs, *Implementation of the 65nm dual-core 64b merom processor.* In IEEE International Solid-State Circuits Conference (ISSCC 2007), 2007.
10. C. Isci, A. Buyuktosunoglu, and M. Martonosi, *Long-term workload phases: Duration predictions and applications to DVFs.* Ieee Micro, 2005. **25**(5): p. 39-51.
11. S.M. Sze, *Physics of Semiconductor Devices*. 2nd ed. 1981: Joho Wiley & Sons.
12. R.H. Dennard, F.H. Gaensslen, H.N. Yu, et al., *Design of ion-implanted MOSFET's with very small physical dimensions (Reprinted from IEEE Journal of Solid-State Circuits, vol 9, pg 256-268, 1974).* Proceedings of the Ieee, 1999. **87**(4): p. 668-678.
13. D.A. Buchanan, *Scaling the gate dielectric: Materials, integration, and reliability.* Ibm Journal of Research and Development, 1999. **43**(3): p. 245-264.
14. H.S.P. Wong, *Beyond the conventional transistor.* Ibm Journal of Research and Development, 2002. **46**(2-3): p. 133-168.
15. H.S.P. Wong, *Beyond the conventional transistor.* Solid-State Electronics, 2005. **49**(5): p. 755-762.
16. J. Robertson, *Band offsets of high dielectric constant gate oxides on silicon.* Journal of Non-Crystalline Solids, 2002. **303**(1): p. 94-100.
17. J. Robertson, *High dielectric constant gate oxides for metal oxide Si transistors.* Reports on Progress in Physics, 2006. **69**(2): p. 327-396.
18. G.D. Wilk, R.M. Wallace, and J.M. Anthony, *High-kappa gate dielectrics: Current status and materials properties considerations.* Journal of Applied Physics, 2001. **89**(10): p. 5243-5275.
19. G.A. Battiston, G. Carta, G. Cavinato, et al., *MOCVD of Al2O3 films using new dialkylaluminum acetylacetonate precursors: Growth kinetics and process yields.* Chemical Vapor Deposition, 2001. **7**(2): p. 69-74.
20. C.C. Yeh, T.H. Wang, W.J. Tsai, et al., *A novel fully CMOS process compatible PREM for SOC applications.* Ieee Electron Device Letters, 2005. **26**(3): p. 203-204.

21. A.W. Ott, K.C. McCarley, J.W. Klaus, et al., *Atomic layer controlled deposition of Al2O3 films using binary reaction sequence chemistry.* Applied Surface Science, 1996. **107**: p. 128-136.
22. M.D. Groner, J.W. Elam, F.H. Fabreguette, et al., *Electrical characterization of thin Al2O3 films grown by atomic layer deposition on silicon and various metal substrates.* Thin Solid Films, 2002. **413**(1-2): p. 186-197.
23. K.J. Hubbard and D.G. Schlom, *Thermodynamic stability of binary oxides in contact with silicon.* Journal of Materials Research, 1996. **11**(11): p. 2757-2776.
24. W. Koh, S.J. Ku, and Y. Kim, *Chemical vapor deposition of Al2O3 films using highly volatile single sources.* Thin Solid Films, 1997. **304**(1-2): p. 222-224.
25. P.F. Lee, J.Y. Dai, H.L.W. Chan, et al., *Two-step interfacial reaction of HfO2 high-k gate dielectric thin films on Si.* Ceramics International, 2004. **30**(7): p. 1267-1270.
26. E.P. Gusev, C. Cabral, M. Copel, et al., *Ultrathin HfO2 films grown on silicon by atomic layer deposition for advanced gate dielectrics applications.* Microelectronic Engineering, 2003. **69**(2-4): p. 145-151.
27. D.D. Han, J.F. Kang, C.H. Lin, et al., *Reliability characteristics of high-K gate dielectrics HfO2 in metal-oxide semiconductor capacitors.* Microelectronic Engineering, 2003. **66**(1-4): p. 643-647.
28. W. Nieveen, B.W. Schueler, G. Goodman, et al., *Analysis of high-k hfO(2) and HfSiO4 dielectric films.* Applied Surface Science, 2004. **231-2**: p. 556-560.
29. O. Renault, D. Samour, D. Rouchon, et al., *Interface properties of ultra-thin HfO2 films grown by atomic layer deposition on SiO2/Si.* Thin Solid Films, 2003. **428**(1-2): p. 190-194.
30. K. Kukli, K. Forsgren, J. Aarik, et al., *Atomic layer deposition of zirconium oxide from zirconium tetraiodide, water and hydrogen peroxide.* Journal of Crystal Growth, 2001. **231**(1-2): p. 262-272.
31. H.W. Chen, T.Y. Huang, D. Landheer, et al., *Physical and electrical characterization of ZrO2 gate insulators deposited on Si(100) using Zr(O-i-Pr)(2)(thd)(2) and O-2.* Journal of the Electrochemical Society, 2002. **149**(6): p. F49-F55.
32. S. Ferrari, D.T. Dekadjevi, S. Spiga, et al., *Structural and electrical characterization of ALCVD ZrO2 thin films on silicon.* Journal of Non-Crystalline Solids, 2002. **303**(1): p. 29-34.
33. Y.S. Lin, R. Puthenkovilakam, J.P. Chang, et al., *Interfacial properties of ZrO2 on silicon.* Journal of Applied Physics, 2003. **93**(10): p. 5945-5952.
34. X. Wu, D. Landheer, M.J. Graham, et al., *Structure and thermal stability of MOCVD ZrO2 films on Si (100).* Journal of Crystal Growth, 2003. **250**(3-4): p. 479-485.
35. S. Boughaba, M. Islam, J.P. McCaffrey, et al., *Ultrathin Ta2O5 films produced by large-area pulsed laser deposition.* Thin Solid Films, 2000. **371**(1-2): p. 119-125.
36. S. Boughaba, G.I. Sproule, J.P. McCaffrey, et al., *Synthesis of tantalum pentoxide films by pulsed laser deposition: material characterization and scale-up.* Thin Solid Films, 2000. **358**(1-2): p. 104-113.
37. A.Y. Mao, K.A. Son, D.A. Hess, et al., *Annealing ultra thin Ta2O5 films deposited on bare and nitrogen passivated Si(100).* Thin Solid Films, 1999. **349**(1-2): p. 230-237.
38. R.B. van Dover, D.V. Lang, M.L. Green, et al., *Crystallization kinetics in amorphous (Zr0.62Al0.38)O-1.8 thin films.* Journal of Vacuum Science & Technology a-Vacuum Surfaces and Films, 2001. **19**(6): p. 2779-2784.

39. C. Zhao, O. Richard, E. Young, et al., *Thermostability of amorphous zirconium aluminate high-k layers.* Journal of Non-Crystalline Solids, 2002. **303**(1): p. 144-149.
40. W.J. Qi, R. Nieh, B.H. Lee, et al., *Electrical and reliability characteristics of ZrO2 deposited directly on Si for gate dielectric application.* Applied Physics Letters, 2000. **77**(20): p. 3269-3271.
41. G.D. Wilk and R.M. Wallace, *Stable zirconium silicate gate dielectrics deposited directly on silicon.* Applied Physics Letters, 2000. **76**(1): p. 112-114.
42. G.D. Wilk, R.M. Wallace, and J.M. Anthony, *Hafnium and zirconium silicates for advanced gate dielectrics.* Journal of Applied Physics, 2000. **87**(1): p. 484-492.
43. D.G. Schlom and J.H. Haeni, *A thermodynamic approach to selecting alternative gate dielectrics.* MRS Bulletin, 2002. **27**(3): p. 198-204.
44. T.N. Jackson and A.B. Wong, IEEE Electron Dev. Lett., 1991. **12**: p. 605.
45. C.O. Chui, H. Kim, P.C. McIntyre, et al., *Atomic layer deposition of high-kappa dielectric for germanium MOS applications-substrate surface preparation.* Ieee Electron Device Letters, 2004. **25**(5): p. 274-276.
46. N. Wu, Q.C. Zhang, C.X. Zhu, et al., *Alternative surface passivation on germanium for metal-oxide-semiconductor applications with high-k gate dielectric.* Applied Physics Letters, 2004. **85**(18): p. 4127-4129.
47. J.J.H. Chen, N.A. Bojarczuk, H.L. Shang, et al., *Ultrathin Al2O3 and HfO2 gate dielectrics on surface-nitrided Ge.* Ieee Transactions on Electron Devices, 2004. **51**(9): p. 1441-1447.
48. C.O. Chui, S. Ramanathan, B.B. Triplett, et al., *Germanium MOS capacitors incorporating ultrathin high-kappa gate dielectric.* Ieee Electron Device Letters, 2002. **23**(8): p. 473-475.
49. H.L. Shang, K.L. Lee, P. Kozlowski, et al., *Self-aligned n-channel germanium MOSFETs with a thin Ge oxynitride gate dielectric and tungsten gate.* Ieee Electron Device Letters, 2004. **25**(3): p. 135-137.
50. S.M. Gates, D.D. Koleske, J.R. Heath, et al., *Epitaxial Si films on Ge(100) grown via H/Cl exchange.* Applied Physics Letters, 1993. **62**(5): p. 510.
51. D.D. Koleske and S.M. Gates, *Atomic layer epitaxy of Si on Ge(100) using Si2Cl6 and atomic hydrogen.* Applied Physics Letters, 1994. **64**: p. 884.
52. S. Toyoda, J. Okabayashi, H. Takahashi, et al., *Nitrogen doping and thermal stability in HfSiOxNy studied by photoemission and x-ray absorption spectroscopy.* Applied Physics Letters, 2005. **87**(18): p. -.
53. T. Deegan and G. Hughes, *An X-ray photoelectron spectroscopy study of the HF etching of native oxides on Ge(111) and Ge(100) surfaces.* Applied Surface Science, 1998. **123**: p. 66-70.
54. K. Choi and J.M. Buriak, *Hydrogermylation of alkenes and alkynes on hydride-terminated Ge(100) surfaces.* Langmuir, 2000. **16**(20): p. 7737-7741.
55. D. Bodlaki, H. Yamamoto, D.H. Waldeck, et al., *Ambient stability of chemically passivated germanium interfaces.* Surface Science, 2003. **543**(1-3): p. 63-74.
56. S. Rivillon, Y.J. Chabal, F. Amy, et al., *Hydrogen passivation of germanium (100) surface using wet chemical preparation.* Applied Physics Letters, 2005. **87**(25): p. -.
57. J.P. Xu, P.T. Lai, C.X. Li, et al., *Improved electrical properties of germanium MOS capacitors with gate dielectric grown in Wet-NO ambient.* Ieee Electron Device Letters, 2006. **27**(6): p. 439-441.

58. C.X. Li, P.T. Lai, and J.P. Xu, *Improved reliability of Ge MOS capacitor with HfTiON high-k dielelctric by using Ge surface pretreatment in wet NO.* Microelectronic Engineering, 2007. **84**(9-10): p. 2340-2343.
59. S. Takagi, T. Maeda, N. Taoka, et al., *Gate dielectric formation and MIS interface characterization on Ge.* Microelectronic Engineering, 2007. **84**(9-10): p. 2314-2319.
60. P. Batude, X. Garros, L. Clavelier, et al., *In-depth investigation of the mechanisms impacting C-V/G-V characteristics of Ge/GeON/HfO2/TiN stacks by electrical modeling.* Microelectronic Engineering, 2007. **84**(9-10): p. 2320-2323.
61. T. Maeda, M. Nishizawa, Y. Morita, et al., *Role of germanium nitride interfacial layers in HfO2/germanium nitride/germanium metal-insulator-semiconductor structures.* Applied Physics Letters, 2007. **90**(7): p. -.
62. Y.Q. Wang, J.H. Chen, W.J. Yoo, et al., *Formation of Ge nanocrystals in HfAlO high-k dielectric and application in memory device.* Applied Physics Letters, 2004. **84**(26): p. 5407-5409.
63. H. Kim, P.C. McIntyre, C.O. Chui, et al., *Interfacial characteristics of HfO2 grown on nitrided Ge (100) substrates by atomic-layer deposition.* Applied Physics Letters, 2004. **85**(14): p. 2902-2904.
64. T. Maeda, T. Yasuda, M. Nishizawa, et al., *Ge metal-insulator-semiconductor structures with Ge3N4 dielectrics by direct nitridation of Ge substrates.* Applied Physics Letters, 2004. **85**(15): p. 3181-3183.
65. T. Maeda, T. Yasuda, M. Nishizawa, et al., *Pure germanium nitride formation by atomic nitrogen radicals for application to Ge metal-insulator-semiconductor structures.* Journal of Applied Physics, 2006. **100**(1): p. -.
66. S.Y. Sun, Y. Sun, Z. Liu, et al., *Surface termination and roughness of Ge(100) cleaned by HF and HCl solutions.* Applied Physics Letters, 2006. **88**(2): p. -.
67. Z.H. Lu, *Air-stable Cl-terminated Ge(111).* Applied Physics Letters, 1996. **68**(4): p. 520.
68. T. Weser, A. Bogen, B. Konrad, et al., Physics Review B, 1987. **35**: p. 8148.
69. T. Weser, A. Bogen, B. Konrad, et al., Surface Science, 1988. **201**: p. 245.
70. K. T. Leung, L. J. Terminello, Z. Hussain, et al., Physics Review B, 1988. **38**: p. 8241.
71. K. Newstead, A. W. Robinson, S. d'Addato, et al., Journal of Physics: Condensed Matter, 1992. **4**: p. 8441.
72. P. Kru¨ger and J. Pollmann, Physics Review Letters, 1990. **64**: p. 1808.
73. J. Pollmann, P. Kru¨ger, and A. Mazur, Applied Surface Science, 1992. **56-58**: p. 193.
74. M.M. Frank, S.J. Koester, M. Copel, et al., *Hafnium oxide gate dielectrics on sulfur-passivated germanium.* Applied Physics Letters, 2006. **89**(11): p. -.
75. T. Maeda, S. Takagi, T. Ohnishi, et al., *Sulfur passivation of Ge (001) surfaces and its effects on Schottky barrier contact.* Materials Science in Semiconductor Processing, 2006. **9**(4-5): p. 706-710.
76. G.W. Anderson, M.C. Hanf, P.R. Norton, et al., *The S-Passivation of Ge(100)-(1x1).* Applied Physics Letters, 1995. **66**(9): p. 1123-1125.

Chapter 2 Thin Film Characterization Techniques

Several thin film characterization techniques including XPS, RBS, AFM and FT-IR have been used to study the physical properties of high-k films as well as their interfaces with Ge substrates. In this chapter, the principles of each technique will be briefly introduced along with a description of the instruments and settings used in this work.

Section 2.1 X-ray Photoelectron Spectroscopy

X-ray photoelectron spectroscopy (XPS), also known as electron spectroscopy for chemical analysis (ESCA), is a quantitative spectroscopic technique that yields information on the electronic structure, elemental composition and chemical state in the near surface region (< 5 nm) of a material. It has its origins in the discovery of the photoelectric effect by Hertz [1], was given a more precise energetic description by Einstein [2] and was further developed in the work by Robinson and Rawlinson [3] of X-ray photoelectron spectra for different metals. Later, Siegbahn, et al. [4, 5] developed XPS into a sensitive, high resolution method for the determination of the binding energy of the electrons for which he was eventually awarded the Nobel Prize. Today XPS is a standard technique capable of providing valuable information about the electronic structure, the chemical composition and the stoichiometry near the surface of the sample.

2.1.1 Principle of XPS

XPS spectra are obtained by irradiating a material in vacuum with a beam of soft X-rays while simultaneously measuring the kinetic energy and number of electrons that escape from the top several atomic layers of the material being analyzed. XPS requires ultra-high vacuum (UHV) conditions. During analysis, the pressures of chambers that were used in this work were in the 10^{-9}-10^{-10} Torr range. Figure 2-1 shows the schematic drawing of the primary XPS system used in this study.

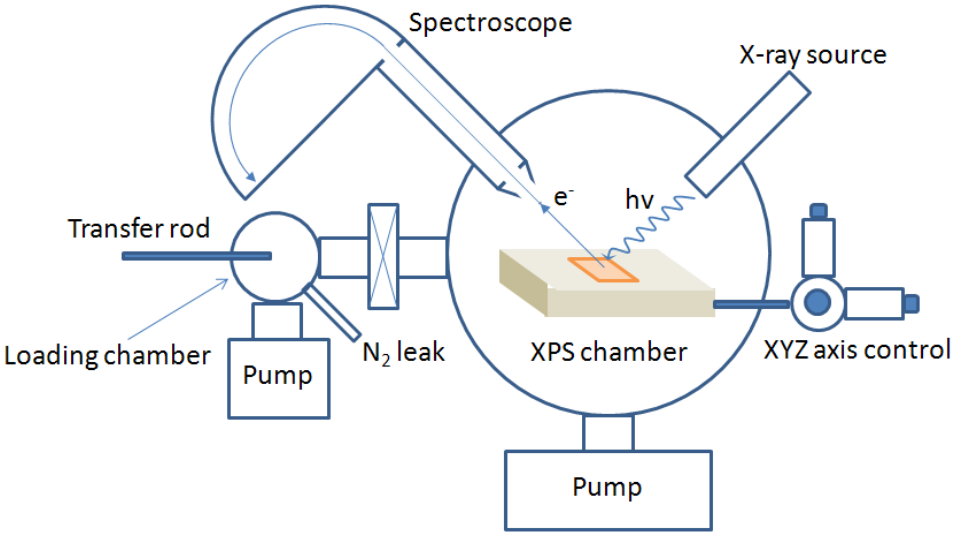


Figure 2-1: Schematic drawing of XPS system.

Photons in the x-ray range of the spectrum can have energies as high as 10 keV and when allowed to interact with atoms will interact with orbiting electrons primarily via a conventional photon absorption process [6]. Both monochromatic aluminum K-alpha x-rays (1486.7 eV) and non-monochromatic

magnesium K-alpha x-ray (1253.6 eV) are commonly used. Typically, monochromatic aluminum x-rays have better energy resolution (0.4-0.6 eV) than non-monochromatic magnesium x-rays (0.9-1.0 eV). For much higher energy resolution, high-intensity, narrow-energy-width synchrotron radiation, is used.

If the photon energy is higher than the binding energy of core electrons in a material, the photons can interact with it and generate a photoelectron. Only those electrons originating from the surface, or a few atomic layers below, can escape from the surface to reach the detector and contribute to an XPS peak. Electrons that scatter on their way out of a solid contribute to the broad secondary electron background. Since the mean free path of electrons in solids is very small, most of the detected electrons come from the top 5 nm of the sample. This makes XPS a surface-sensitive technique for chemical analysis [7].

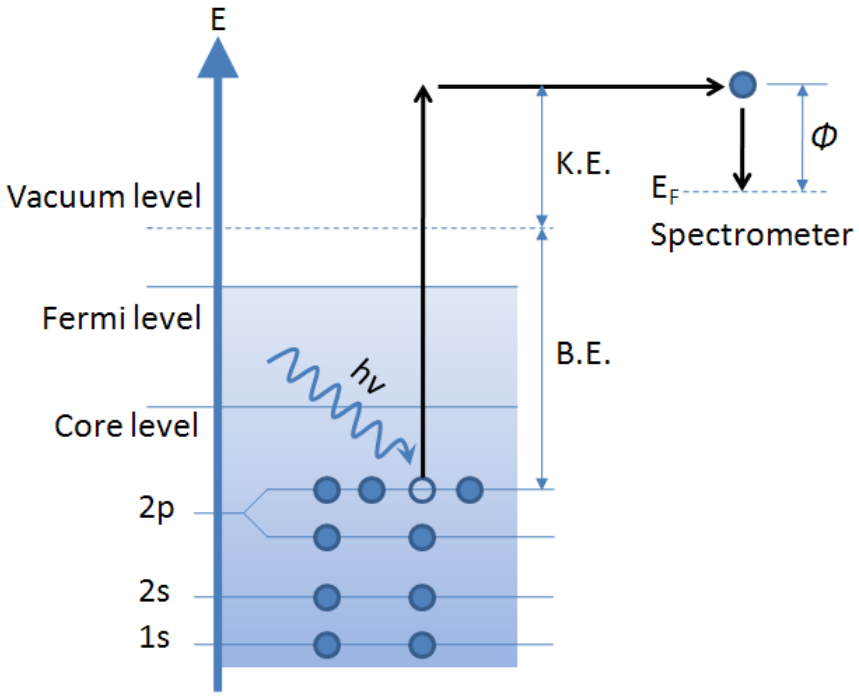


Figure 2-2: Energy-level diagrams showing the electron transitions in XPS.

Figure 2-2 illustrates the electronic transition involved in XPS. First, an electron is ejected from one of the core electronic levels by an incident X-ray photon. The kinetic energy KE of the emitted core electron as measured by the instrument is:

$$KE = h\nu - BE - \phi$$

where $h\nu$ is the energy of the incident X-ray photons, BE is the binding energy of the atomic orbital from which the emitted electron originates, and ϕ is the work function of the spectrometer.

Because each element has a unique set of binding energies, XPS spectra can be used to identify and determine the concentration of the elements in the surface. The binding energy of a core-level electron depends also on the surroundings of the atoms. Variations of binding energies for an element in different chemical compounds can arise for various reasons such as: difference in the oxidation state, difference in the molecular environment, different lattice parameters, etc. Binding energy shifts due to these effects are usually called chemical shifts and can be used to identify the chemical oxidation states of the materials being analyzed [8]. The binding energy shift can be expressed in the following equation:

$$\Delta BE = BE - BE_0 = IA + EA$$

where BE_0 is the binding energy of the core-level electron in the isolated atom. The intra-atomic part IA can be described in terms of the effective charge q of the atom in a molecule or crystal as $IA = kq$, where k is a constant for the chemical element. The extra-atomic part EA is the potential energy produced by the

surroundings. This part is often referred as Madelung potential. Identification of chemical states of an atom can be made from the exact measurement of the peak positions and their chemical shifts.

2.1.2 Atomic Sensitivity Factor

From peak areas of XPS spectra, quantitative data such as the relative concentration of the various constituents can be obtained. In order to calculate the relative concentration for each constituent, a sensitivity factor for each element has to be either known or determined. For a sample that is homogeneous in the analysis volume, the number of photoelectrons per second in a specific spectral peak I is given by [7]:

$$I = nf\sigma\theta y\lambda AT$$

where n is the atomic concentration of the element (atoms/cm^3), f is the x-ray flux (photon/cm^2-sec), σ is the photoelectric cross-section for the atomic orbital of interest (cm^2), θ is the instrumental angular efficiency factor between photo path and detected electron, y is the efficiency in the photoelectric process for formation of photoelectrons of the normal photoelectron energy, λ is the mean free path of the photoelectrons in the sample, A is the area of the sample from which photoelectrons are detected and, T is the detection efficiency for electrons emitted from the sample. The atomic sensitivity factor S is then defined as:

$$S = f\sigma\theta y\lambda AT$$

With sensitivity factors known, the stoichiometric ratio of two elements A and B can be determined from the peak height or peak areas:

$$\frac{n_A}{n_B} = \frac{I_A/S_A}{I_B/S_B}$$

where S_A and S_B are the sensitivity factors for the elements, which are tabulated and listed in literature [7]. The expression may be used for all homogeneous samples if the ratio S_A/S_B is matrix-independent.

	C 1s	O 1s	Ge 3d	S 2p
Sensitivity Factor	0.25	0.66	0.38	0.54

Table 2-1: Values of XPS atomic sensitivity factors used in this work [7].

2.1.3 Depth Profiling Using XPS

XPS can be used for depth profiling, the in-depth distribution analysis of the chemical or elemental composition of a sample. From XPS spectra, the chemical state composition versus depth analysis can be obtained either by destructive or non-destructive techniques.

The destructive depth profiling technique involves removal of the top layer of samples while XPS spectra are analyzed. Usually ion sputtering with a known sputtering rate is used. This method allows for the determination of the composition over a wide range of thickness (from nanometers to microns). However, sputtering can easily lead to a change in surface stoichiometry and structure, and should be used with caution.

Figure 2-3 shows a comparison of XPS and RBS (discussed in Section 2.2) depth profiling on a Ge/SiO_2/Si sample [9]. Ge was ion implanted into the thermally grown SiO_2 layers of about 500 nm thickness. The XPS measurements were done using the following parameters: Al-Kα x-rays, Ge2p peak at 1217 eV, binding energy (BE) = 270 eV kinetic energy, and sputtering with Ar^+ primary ions (3 nm/min). The element depth distributions from both techniques are in good agreement.

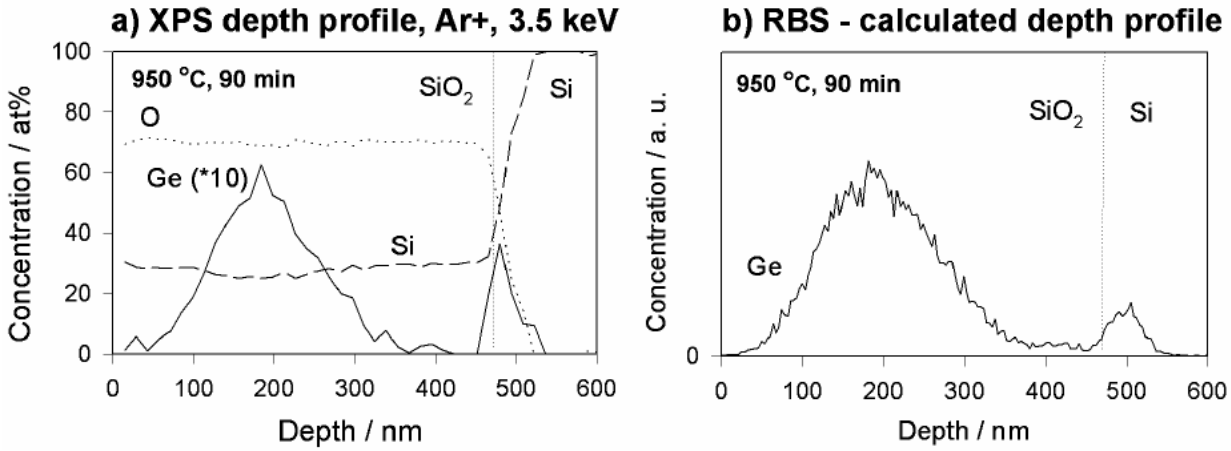


Figure 2-3: Comparison of XPS (a) and RBS (b) depth profiling on a Ge/SiO_2/Si sample annealed in O_2 [9].

After a photoelectron escapes from an atom, it travels some distance inside the solid before it escapes to vacuum or is scattered. On the way, either elastic or inelastic collisions occur within the lattice atoms. Electron kinetic energy remains unchanged in elastic collision but decreases in inelastic collisions. Inelastically scattered electrons will form part of the spectrum background or will not escape from the solid. The probability for photoelectrons to escape from the depth d can be written as:

$$I \propto e^{-d/\lambda \cos \phi}$$

where the parameter λ is called inelastic mean free path and ϕ is the electron take-off angle measured from the normal of the sample plane. Figure 2-4 shows the experimental dependence of the mean free path on electron kinetic energy [10].

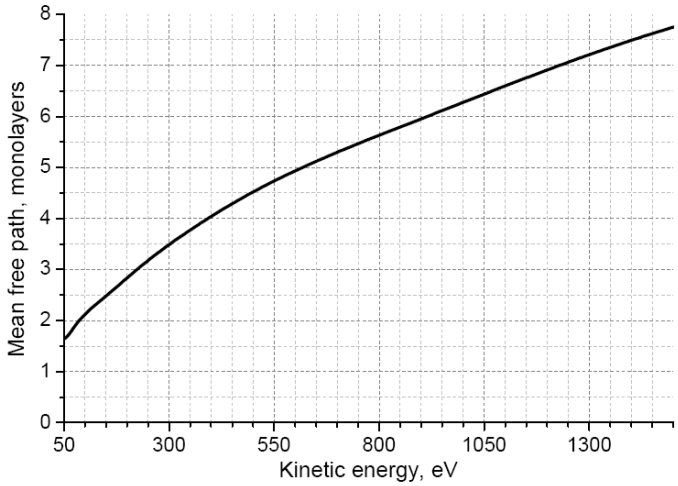


Figure 2-4: Mean free path of photoelectrons in solid [10].

This dependence makes it possible to perform a non-destructive information depth profiling by electron energy dependent analysis. By comparing the intensities of two or more XPS peaks of the same element at low and high kinetic energies, the mean depth of origin of the element signals can be obtained and can be used to determine the thickness of a segregation layer, or an adsorbate layer. For example, if the relative intensities of low kinetic energy I_{LE} and high kinetic energy I_{HE} peaks of a substrate covered by an overlayer and those of the clean surface (I_{LE}^0 and I_{HE}^0, respectively) are obtained in XPS spectra, the thickness d of the overlayer can be estimated from:

$$d = \frac{\lambda_{HE}\lambda_{LE}}{\lambda_{HE} - \lambda_{LE}} \cos\phi \ln \frac{I_{LE}^0 / I_{HE}^0}{I_{LE}/I_{HE}}$$

where λ_{LE} and λ_{HE} are the relevant inelastic mean free paths of the substrate photoelectron signal through the overlayer with low and high kinetic energy respectively, and ϕ is the electron take-off angle measured from the normal of the sample plane.

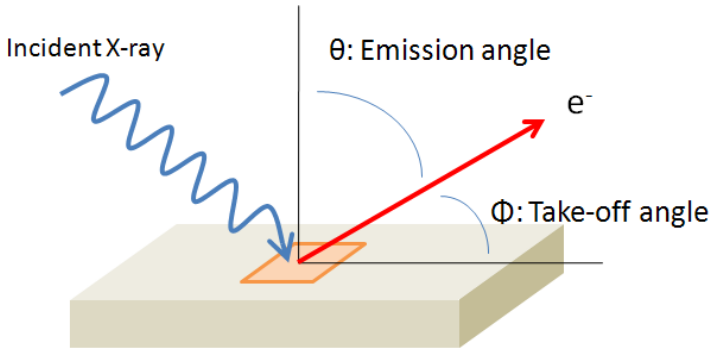


Figure 2-5: Geometry of angle resolved XPS setup.

Another non-destructive method to obtain dependence of information on depth is a form of angular resolved photoelectron spectroscopy (ARPES) [11]. The basics of this method, for a given electron energy, include varying the take-off angle ϕ between the direction of photoelectron detection and the normal of the sample surface. For the case of a smooth homogeneous oxide film A on a substrate B, the thickness d of the oxide film A is given by:

$$d = \lambda \cos\phi \ln\left(1 + \frac{1}{Q}\right)$$

$$Q = \frac{I_B/I_A}{I_B^0/I_A^\infty}$$

where λ is the inelastic mean free path of electrons in the oxide film A, I_B/I_A is the XPS peak ratio of substrate B to the oxide film A and I_B^0/I_A^∞ is that of the

oxide-free substrate B to an infinitely-thick oxide film A. For this method, no excitation energy tuning is necessary and therefore, it can be performed with a conventional single-energy x-ray source.

However, there are several disadvantages of the non-destructive XPS profiling methods. First, there is a limitation to the total probing depth which is about three times the inelastic mean free path (typically < 5 nm). Second, the dependence of the data quality on surface roughness makes it difficult for any structure other than laterally homogeneous films. Third, the presence of angular-dependent effects on valence band of ordered surfaces (e.g. single crystals) often makes it impossible to perform depth profiling based on valence band photoelectrons by this method. The depth resolution is generally limited by the experimental error in the intensity measurement.

Section 2.2 Rutherford Backscattering Spectroscopy

Rutherford backscattering spectroscopy (RBS) [12] is a method to determine the composition of a sample based on bombarding a sample with high energy ions and measuring the energy of the backscattered ions. This ion beam analysis technique allows the determination of both the atomic mass and concentration of each elemental target constituents as a function of the depth from 10nm to a few µm under the surface, as well as the crystal structure in the case of single crystal materials, in a non-destructive manner.

2.2.1 Kinematics of RBS

In RBS measurements, incident monochromatic H^+ or He^+ ions within the range 1- 4 MeV undergo elastic collisions and are backscattered from the near-surface region of the solid targets at various angles. The number and energy distribution of the back-scattered ions are measured and used in the calculation of the target atomic masses, concentrations and depth distributions. Because of the kinematics of the scattering process, this technique is best suited for the detection of impurity or surface elements which are heavier than the constituents of the substrate and for targets having atomic number $Z > 10$. The back-scattering method is illustrated in Figure 2-6.

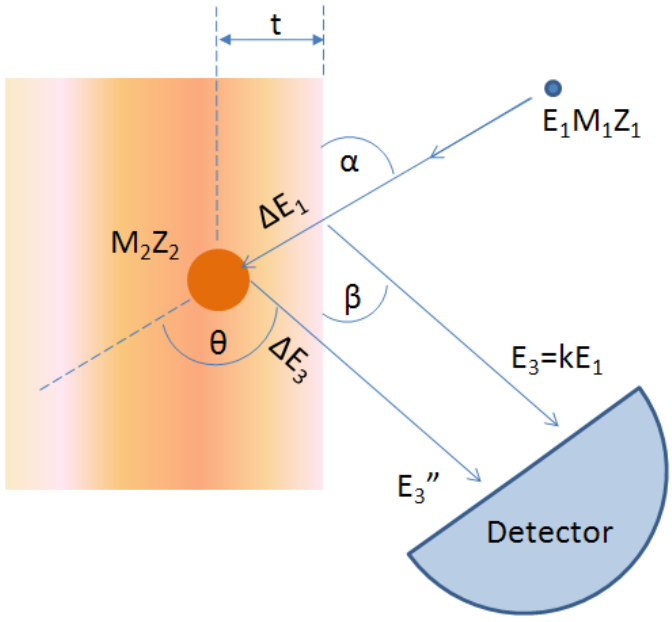


Figure 2-6: Rutherford Back Scattering Spectroscopy (RBS).

In RBS, the mono-energetic particles that comprise the incident beam collide with target atoms. A small fraction of these collisions cause the primary particle to backscatter at a scattering angle θ into a detector which measures

their energies. The energy of the scattered particles E_3 depends on the mass M_1 (atomic number Z_1) and the initial energy E_1 of the projectile, the mass of the target atom M_2 (atomic number Z_2) and the geometry of the scattering event, as shown in Figure 2-6. For an elastic collision, the energy of the projectile after the collision E_3 is directly proportional to the projectile's initial energy E_1.

$$E_3 = KE_1$$

where K is called the kinematic factor and can be determined by applying the principles of the conservation of mass and momentum:

$$K = \frac{\sqrt{M_2^2 - (M_1 \sin\theta)^2} + M_1 \cos\theta}{M_1 + M_2}$$

The kinematic factor K is larger for heavier target atoms and smaller scattering angles.

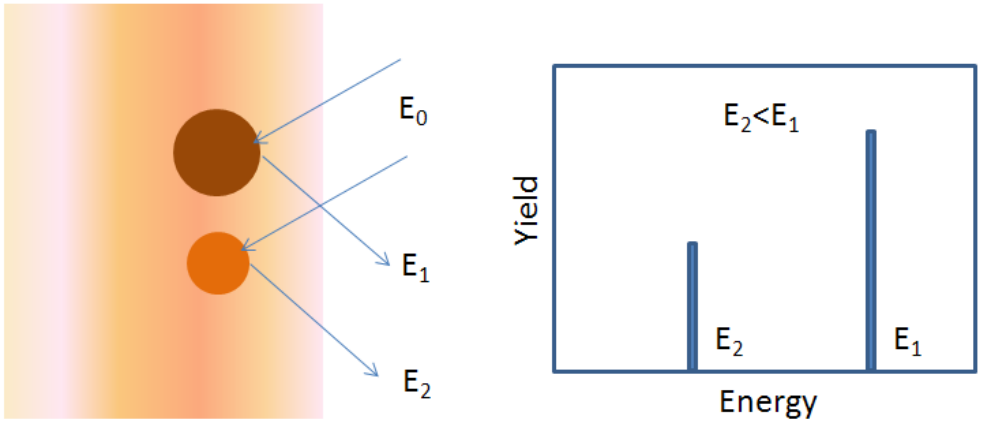


Figure 2-7: The position of RBS peaks reflects the mass difference of targets.

Figure 2-8 presents the kinematic factor as a function of target mass for He^+ ions backscattered at scattering angles of 90°, 120° and 150°. Figure 2-9

plots the kinematic factor for He^+ ions backscattered from O, Al, Ge and Hf at various scattering angles.

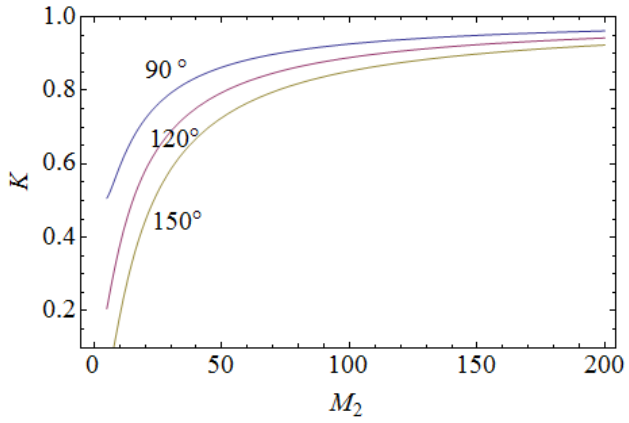


Figure 2-8: Kinematic factor for He+ ions backscattering from different masses at different scattering angles.

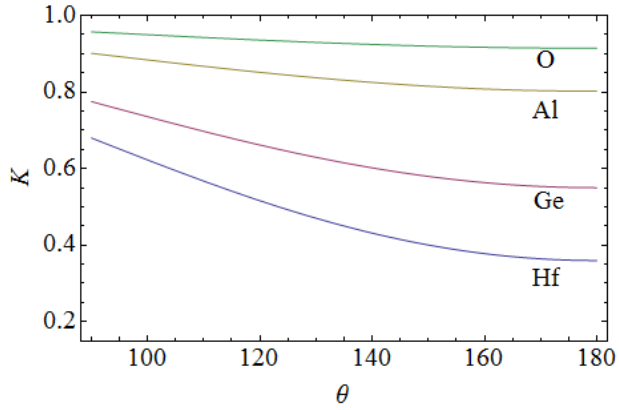


Figure 2-9: Kinematic factor for He+ ions backscattering from different targets at different scattering angles.

The projectile mass must be smaller than that of the target atom ($M_1 < M_2$) for backscattering to occur ($\theta > 90°$). In order to analyze a wide range of target masses, light projectiles such as H^+ and He^+ ions are typically used in backscattering experiments.

The ability of the backscattering system to distinguish between target atoms with a mass difference δM_2, is determined by the ability of the system to resolve energy differences δE of backscattered particles. The mass resolution of the system is given by

$$\delta M_2 = \frac{\delta E}{E_1 \frac{dK}{dM_2}}$$

Mass resolution can be improved by increasing the incident energy E_1, using a larger projectile mass M_1, using scattering angles close to 180°, or by improving the overall energy resolution, δE.

2.2.2 Scattering Cross Section and Areal Density of Target Atoms

The probability P, that a particle will be backscattered from a sample with areal density N_t into the detector solid angle Ω, is given by the ratio of the number of detected particles Y (the yield), to the number of incident particles Q:

$$P = \frac{Y}{Q}$$

The yield Y of backscattered particles depends on the differential cross section. By assuming the Coulomb force between the incident and target nuclei, an unscreened Rutherford cross section may be calculated from the following:

$$\frac{d\sigma(E,\theta)}{d\Omega} = \left(\frac{Z_1 Z_2 e^2}{16\pi E}\right)^2 \frac{4}{(\sin\theta)^4} \frac{\left(\sqrt{1-\left(\frac{M_1}{M_2}\sin\theta\right)^2} + \cos\theta\right)^2}{\sqrt{1-\left(\frac{M_1}{M_2}\sin\theta\right)^2}}$$

where E is the energy of the ion immediately before scattering, e is the electronic charge, and θ is the scattering angle. For small detector solid angles ($\Omega < \sim 10$ msr) and well defined scattering angles θ, the differential cross section $d\sigma/d\Omega$ simplifies to $\sigma(E,\theta)$ [13]:

$$\sigma(E,\theta) = \int \frac{d\sigma(E,\theta)}{d\Omega} d\Omega \approx 4\pi \frac{d\sigma(E,\theta)}{d\Omega}$$

Actual cross sections can deviate from the Rutherford description if nuclear reaction is involved or if the energy is low enough when electron screening of the nucleus is important. Ion beam techniques are termed *Nuclear Reaction Analysis* (NRA, 100 keV ~ 1 MeV) if nuclear reaction happens [14], *Medium Energy Ion Scattering* (MEIS, 20~200 keV) if the beam energy is low enough such that the cross sections deviate from an unscreened Rutherford value by more than about one percent [15, 16], or *Low Energy Ion scattering* (LEIS, 500 eV ~ some keV) if the Rutherford cross section totally breaks down [17].

The areal density $(N_t)_i$ (atoms/cm^2) of the *i*th element with the physical thickness t can be determined with knowledge of σ, Ω, the integrated peak count A_i, and the total charge collected Q by

$$(N_t)_i = \frac{A_i \cos\varphi}{Q.\sigma_i(E,\theta)\Omega}$$

where φ is the angle between the incident beam and target normal. The average atomic ratio for a film containing compound A_mB_n can be calculated by taking the ratio of atomic densities:

$$\frac{n}{m} = \frac{(N_t)_B}{(N_t)_A} = \frac{A_A}{A_B}.\frac{\sigma_A(E,\theta)}{\sigma_B(E,\theta)}$$

This equation can be used to calculate stoichiometric ratios without knowledge of the quantities Q and Ω. The uncertainty of average stoichiometric ratios determined by this is a few tenths of 1% [18].

In the compound A_mB_n, the areal density $(N_t)_i$ of the *i*th element can be converted to a physical film thickness t if the mass density, ρ_{AB} of the film A_mB_n is known:

$$t = \frac{(N_t)_A}{N_A^{AB}} = \frac{(N_t)_B}{N_B^{AB}}$$

The atomic densities are defined as

$$N_A^{AB} = \frac{m\rho_{AB}N_0}{M_{AB}}$$

$$N_B^{AB} = \frac{n\rho_{AB}N_0}{M_{AB}}$$

where N_0 is Avogadro's number and $M_{AB} = mM_A + nM_B$ is the molecular weight of compound A_mB_n. Areal densities obtained from the equation above have an uncertainty of about ±3% [18].

2.2.3 Depth Profiling Using RBS

The energy losses of the incident particles that result when penetrating the sample occur both along the incident path, before the main scattering event (with energy loss ΔE_1) and after backscattering, along the exit path (with energy loss ΔE_3). The energy loss process is due to many kinds of interactions between the projectile ion, target nuclei, and target electrons [18], and can be viewed as an

average over all possible energy dissipative processes activated by the projectile as it passes an atom [19]. The total energy loss ΔE is

$$\Delta E = K\Delta E_1 + \Delta E_3$$

The energy loss extracted from RBS spectra can be used to identify scattering depth and provides a profile of target constituents.

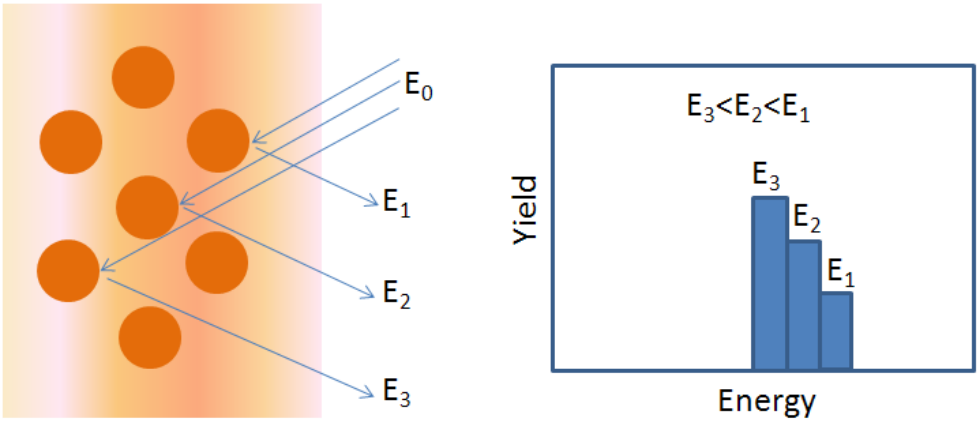


Figure 2-10: The position of RBS peaks reflects the depth distribution of targets.

The amount of energy the ion loses per distance traveled in matter is given by the stopping power of the material, which depends on the energy, the charge and the mass of the ion as well as the material traversed. These interactions are due only to electromagnetic forces and any energy lost to nuclear reactions between the projectile and target nuclei can be ignored in RBS [20].

The stopping cross section ε is the energy loss per unit areal density and is related to the energy loss rate via the physical thickness traversed:

$$\varepsilon = \frac{1}{N}\frac{dE}{dx}$$

where N is the atomic density in atoms/cm^3 and dE/dx is the stopping power. In the low energy regime, the stopping cross section decreases because projectiles may capture electrons from the target and partially neutralize their nuclear charge. The stopping cross section decreases at higher energy because the projectile with larger velocity spends less time in the vicinity of the atom [13].

An approximation called Bragg's rule is used to determine the stopping of ions in compounds. This approximation ignores the effects of chemical bonding in the compound and assumes that each target atom independently contributes to the energy loss process [19]. The compound stopping cross section in terms of energy loss/molecule/cm^2 traversed for a compound A_mB_n can be approximated by

$$\varepsilon^{A_mB_n} = m\varepsilon^A + n\varepsilon^B$$

The energy loss ΔE of ions traversing matter can be calculated by integrating the stopping power dE/dx over the distance travelled. For the case of thin targets, the stopping power can usually be regarded as constant, so energy loss can be approximated using the following:

$$\Delta E = \int \frac{dE}{dx} dx = Nx\varepsilon(E)$$

where E is taken as either the initial beam energy, E_1 (surface energy approximation), or the mean energy of the analysis ion over path length x (mean energy approximation).

2.2.4 Channeling

The arrangement of atoms in single crystals plays an important role in incident ion-target interactions [13]. When the ions enter a crystalline substrate parallel to one of the crystal axes, the backscattering yield is greatly reduced (~0.01x). The resulting spectrum is called a channeling spectrum. Channeling analysis can be used, for example, to increase the sensitivity to light elements in an amorphous overlayer film by channeling through the crystal substrate beneath the film. By reducing the substrate signal, the signal from light elements superimposed on the substrate signal is enhanced, and thus the sensitivity is greatly improved. Channeling spectra can also be used to determine whether or not the sample is crystalline. The percentage ratio of channeling yield Y_{ch} and not channeling (random) yield Y_r reflects the epitaxial growth quality.

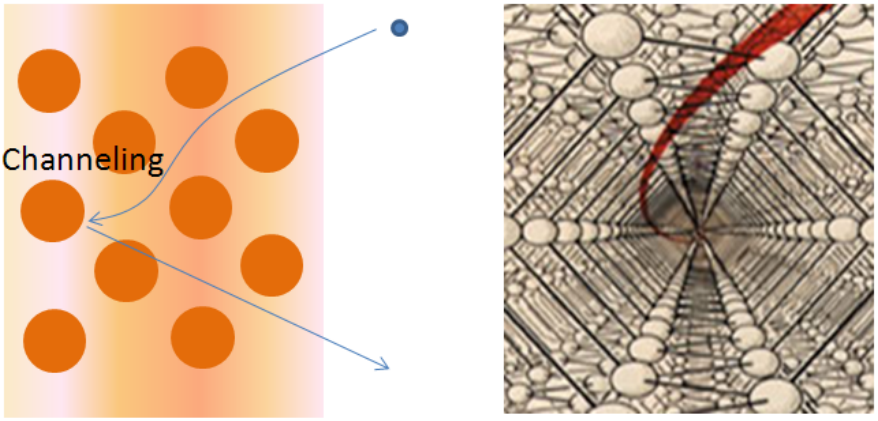


Figure 2-11: Channeling is the guided motion of ions in the open channels of a crystal target.

Figure 2-12 compares simulation of a random and a channeled backscattering spectrum obtained from 270 keV He+ incident on native silicon

oxide on Si(100). The Si peak in the channeled spectrum is due to contributions from the native oxide layer and from the first few monolayers of the Si substrate.

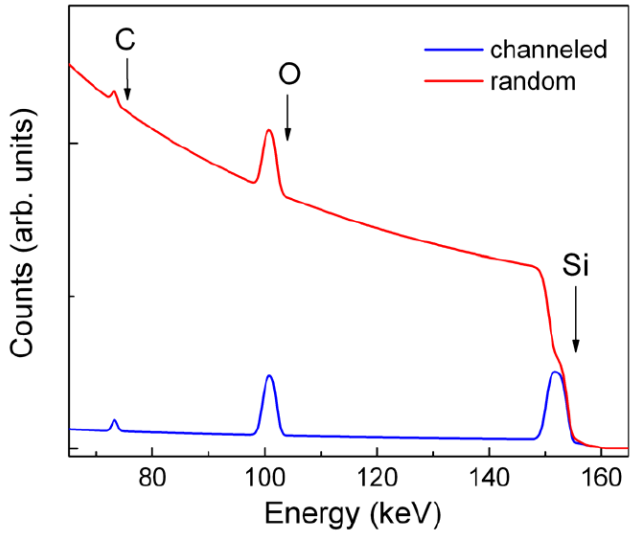


Figure 2-12: Random and channeled spectrum of 270 keV He^+ incident on 25Å SiO_2/Si along <111> [21].

2.2.5 SIMNRA

In this study, the commercial software package SIMNRA [22] is used to model RBS spectra. SIMNRA is a Microsoft Windows based program used to simulate backscattering spectra for ion beam analysis with MeV ions. It can calculate any ion-target combination including incident heavy ions and any geometry including transmission geometry and arbitrary foils in front of the detector. This calculation can give the atomic density d of each layer constructed in the stack model and then the physical film thickness t, can be obtained with the equation:

$$t = \frac{M_{AB}}{(m+n)\rho_{AB}N_0}$$

where N_0 is Avogadro's number, ρ_{AB} is mass density and $M_{AB} = mM_A + nM_B$ is the molecular weight of compound A_mB_n.

Section 2.3 AFM

Atomic force microscopy (AFM) is a type of scanning probe microscopy and is useful for determining the topography of surfaces [23]. It uses a sharp probe to scan across a surface while the interactions between the tip and the sample are monitored.

2.3.1 Principle of AFM

Figure 2-13 shows the schematic drawing of typical commercial AFM equipment. As the cantilever approaches the sample, the force between the cantilever edge and the atoms of the sample surface cause the cantilever to bend. The laser and photo diode are used to detect the bending of the cantilever which gives information of the height of the tip Z above the surface. The cantilever is controlled by a z-direction feedback circuit while a topographic image of the surface results from scanning in the x and y directions.

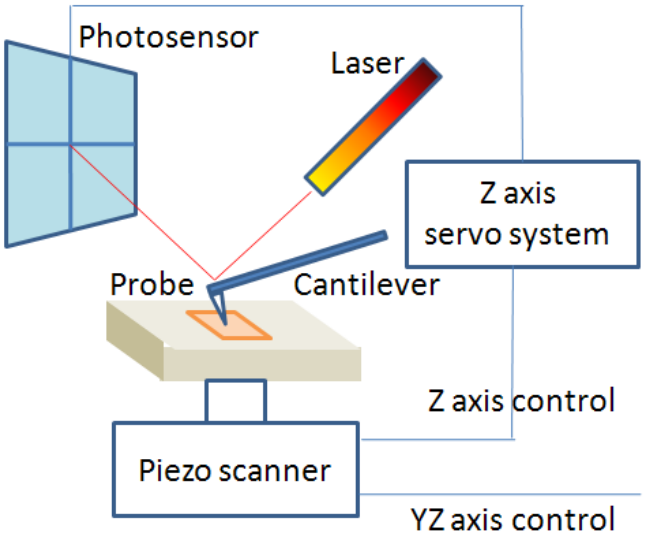


Figure 2-13: A schematic drawing of an AFM system.

There are three primary modes of operating an AFM: contact mode, non-contact mode, and tapping mode. Tapping mode was used for this work. In tapping mode, the cantilever is vibrated by a piezoelectric device, and the probe makes only limited contact to the sample during part of the vibrational cycle. Tapping mode often enables one to measure surface morphology with higher resolution than the other modes, and minimizes damage done to the sample [24].

2.3.2 Quantification of Surface Roughness

To determine the roughness of a sample, an image of the surface is obtained by scanning in the x and y directions. The surface roughness is evaluated by the values of R_{MAX}, the difference between the maximum and minimum height values of the surface and the root mean square (RMS)

roughness. The standard deviation of the height values Z within a given scan area is given by:

$$RMS = \sqrt{\frac{\sum_{i=1}^{N}(Z_i - Z_{avg})}{N}}$$

where Z_{ave} is the average Z value within the given area, Z_i is the current Z value, and N is the number of points within a given area.

AFM measurements should always be performed with high quality, durable, sharp tips. Worn tips produce completely different images and the roughness information obtained is not reliable. One should also take care to avoid multiple tip imaging.

Section 2.4 FT-IR

Fourier transform infrared spectroscopy (FT-IR) [25] is an absorption spectroscopy suitable for identifying chemical bonds by observing the characteristic electromagnetic radiation absorbed by vibrating atoms in molecules or solids in the infrared region.

2.4.1 Absorption Spectroscopy

Absorption spectroscopy is the study of absorption and transmission of light energy in matter. The energy from the photons can be absorbed by electronic, vibrational, or rotational transitions in molecules, corresponding to

electromagnetic radiation in ultraviolet, infrared and micro-wave to mm-wave regions.

In absorption spectroscopy, the reference spectrum I_0, is first measured and another spectrum I is obtained after a change of samples is made. The transmittance T which contains the information on the change of the sample is defined as

$$T = \frac{I}{I_0}$$

When electromagnetic light is absorbed, the power of the transmitted energy decreases exponentially with the path length. The relation between the fraction of light intensity absorbed and the path length is given by:

$$T = e^{-k'd}$$

where d is the path length and k' is a constant. Transmittance also shows similar dependence on the concentration C of the absorbance:

$$T = e^{-k''C}$$

where k'' is another constant. Combine these two equations with the definition of absorbance A as $-\log T$ to give Beer-Lambert law:

$$A = -\log T = adC$$

The constant a is known as absorptivity and is dependent on the wavelength and fundamental physical properties of the molecules. A plot of the transmittance versus wavenumber is called the transmittance spectrum and can be converted into a absorbance spectrum.

2.4.2 Infrared Spectroscopy

When light interacts with matter, the vibrational mode of the chemical bonds in the molecules changes if the vibrating dipole is in phase with the electric vector of the incident radiation. Each chemical bond in a molecule vibrates at a frequency which is characteristic of that bond. The vibrational frequencies of most molecules correspond to the frequencies of infrared light. This is why infrared (wavenumber of 4000–400 cm^{-1}) is usually used in vibrational spectroscopy.

Only those vibrations that result in the change of the molecular, with absorption frequencies in the infrared region, absorb infrared radiation. For example, gas molecules such as H_2 and O_2 do not have dipoles and therefore do not give infrared spectra.

The frequency of these vibrations depends on the mass of the atom and the length and strength of the bonds because the bonds have to absorb radiation of the same frequency as their natural vibrational frequency. For each molecule, a variety of vibrations are possible and each corresponds to a different frequency (Figure 2-14).

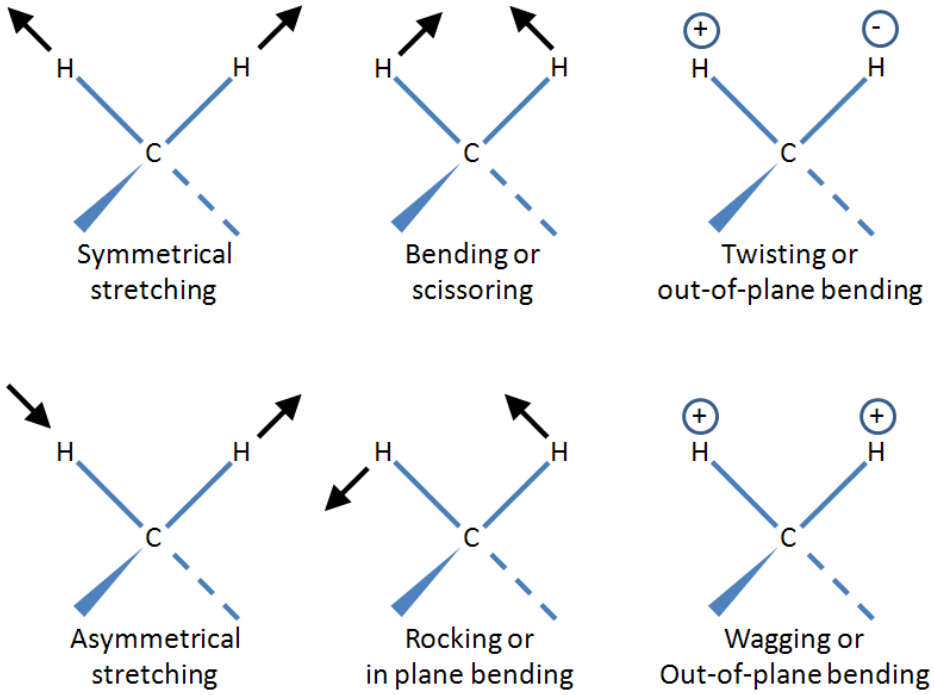


Figure 2-14: Some normal modes of $-CH_2$ molecular vibrations. The + and – symbols indicate a movement out of and into the plane of the paper respectively.

For a given bond or functional group, the absorption occurs within the same wavenumber range regardless of the rest of the structure of the molecule. For instance, the C=O stretch of a carbonyl group occurs at ~1700 cm^{-1} in ketones, aldehydes and carboxylic acids. Therefore infrared absorption spectroscopy is very useful for chemical identification.

2.4.3 FT-IR

Fourier Transform Infrared Spectroscopy (FT-IR) is based on absorption spectroscopy with a significant improvement over traditional infrared spectroscopy. In conventional infrared spectroscopy, the frequency of the infrared light passing through samples is varied using a monochromator. The

amount of energy absorbed is recorded with one frequency at a time. In FT-IR, the infrared light is guided through an interferometer and all the required frequencies pass through the instrument at once. It is called FTIR spectroscopy because a mathematical Fourier transformation is used to interpret the data and produce a spectrum. The measured signals using an interferometer are called interferograms. A Fourier transform is performed on the interferogram to obtain a spectrum identical to that of conventional infrared spectroscopy, although with a better signal to noise ratio for a given data collection time.

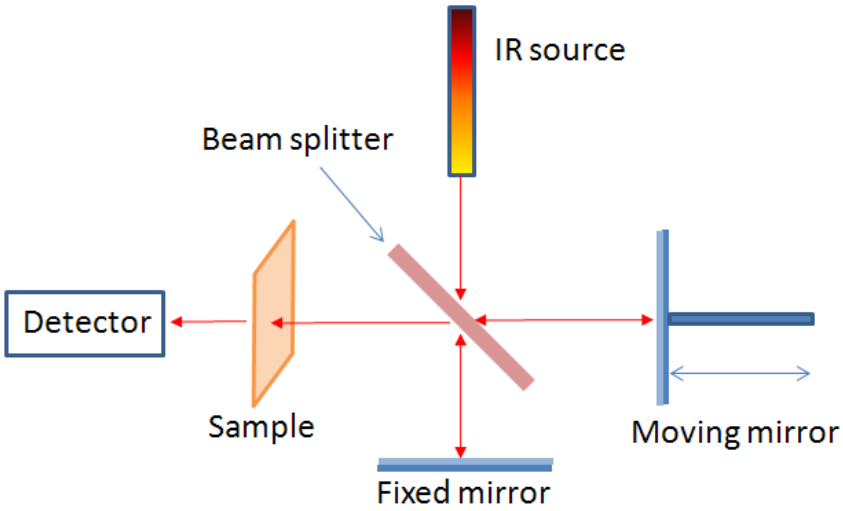


Figure 2-15: Schematic drawing of components of FT-IR and the Michelson interferometer.

Figure 2-15 shows a schematic drawing of an FT-IR spectrometer. A Michelson Interferometer is built around the sample chamber. Radiation from an infrared source is directed through the sample cell to a beam splitter. Half of the infrared beam is reflected from a fixed mirror while the other half is reflected from a mirror which moves continuously over a certain distance. Since the maximum path difference of the two split beams determines the spectral resolution, the

longer the distance the moving mirror moves the better the resolution. When the two beams are recombined at the detector, an interference pattern (interferogram) is produced and stored in a computer. A helium-neon laser is simultaneously directed through the Michelson Interferometer and the interference pattern of the laser is used as a frequency reference.

FT-IR is cheaper, faster and more sensitive than conventional infrared spectroscopy. It is cheaper because building a interferometer is easier than the fabrication of a monochromator. In addition, measurement of a single spectrum is faster for the FT-IR technique because the information at all frequencies is collected simultaneously. Multiple scans can be collected and averaged together resulting in an improvement in sensitivity. Because of these advantages, FT-IR instruments are now used in most modern chemical laboratories.

In this work, the FT-IR measurements were done with the help of Prof. Yves Chabal and his group members. The absorbance Fourier transform infrared spectra were recorded at room temperature on a Nicolet FT-IR spectrometer [26] with OMNIC software [27] at frequencies from 4000 to 400 cm^{-1}, with a resolution of 4 cm^{-1}, gain = 1, and 100 to 500 scans.

Section 2.5 Reference

1. H. Hertz, *On an effect of ultraviolet light upon electric discharge.* Sitzungsber. d. Berl. Akad. d. Wiss., 1877.
2. A. Einstein, *On a heuristic viewpoint concerning the production and transformation of light.* Annalen der Physik, 1905. **17**: p. 132.
3. H. Robinson and W.F. Rawlinson, Phil. Mag., 1914. **28**: p. 277.
4. K. Siegbahn, Philosophical Transactions of the Royal Society of London Series A - Mathematical and Physical Sciences, 1970. **268**: p. 33.
5. K. Siegahn, C. Nordling, A. Fahlman, et al., Nova Acta Regiae Soc. Sci Upsaliensis, 1967: p. 20.
6. L.C. Feldrnan and J.W. Mayer. Fundamentals of Surfce and Thin Film Analysis. 1986, New York: North-Holland.
7. J.F. Moulder, W.F. Stickle, P.E. Sobol, et al., *Hand Book X-ray Photoelectron Spectroscopy*. 2nd ed. 1992, Eden Prairie, MN: Perkin-Elmer Corp., Physical Electronics Division.
8. K. Siegbahn, C. Nordling, G. Johansson, et al., *ESCA Applied to Free Molecules*. 1969: North-Holland Publishing Company.
9. S. Oswald, B. Schmidt, and K.H. Heinig, *Influence of sputtering conditions and electron energy on XPS depth profiling of Ge in SiO2.* Crystal Research and Technology, 2005. **40**(12): p. 1134-1138.
10. M.P. Seah, Surf. Interface Anal, 1986. **9**: p. 85-98.
11. S. H¨ufner, *Photoelectron Spectroscopy*. 1996, Berlin: Springer-Verlag.
12. J.R. Bird and J.S. Williams, in *Ion Beams for Materials Analysis*. 1989, Academic Press. p. 104-106.
13. L.C. Feldman and J.W. Mayer, in *Fundamentals of surface and thin film analysis*. 1986, Elsevier Science Publishing Co., Inc: New York. p. 352.
14. C.W. Magee, Nucl. Instr. and Meth., 1981. **191**: p. 297.
15. R.A. Weller, in *Methods in Materials Research*. 2000, Wiley. p. 12b.1-15.
16. R.G. Smeenk, R.M. Tromp, H.H. Kerson, et al., Nucl. Instr. and Meth., 1982. **195**: p. 581.
17. J.W. Rabalais, *Principles and Applications of Ion Scattering Spectrometry: Surface Chemical and Structural Analysis*. 2003, New York: John Wiley & Sons, Inc.
18. J.A. Leavitt, L.C. McIntyre, and M.R. Weller, in *Handbook of modern ion beam materials analysis*, J.R. Tesmer and M.A. Nastasi, Editors. 1995, Mater. Res. Soc.: Pittsburg. p. 5-19.
19. W.K. Chu, J.M. Mayer, and M.A. Nicolet, *Backscattering Spectrometry*. 1978, New York: Academic Press.
20. J.F. Ziegler, *Stopping of energetic light Ions in elemental matter.* Journal of Applied Physics, 1999. **85**(3): p. 1249-1272.
21. R.D. Geil, *Analysis of high-k dielectric thin films with time-of-flight medium energy backscattering*. 2005, Vanderbilt University: Nashville, Tennessee.
22. M. Mayer. *SIMNRA 6.0*. Available from: http://www.rzg.mpg.de/~mam/.
23. C.R. Blanchard and J.B. Campbell, *Atomic-force microscopy.* Advanced Materials & Processes, 1995. **148**(2): p. 62-62.
24. D.A. Bonnell, in *Scanning Probe Microscopy and Spectroscopy: Theory, Techniques, and Applications*. 2001, Wiley: New York. p. 493.

25. J. Sherma, *Fourier transform infrared (FT-IR) spectrometry*. Journal of Aoac International, 2004. **87**(4): p. 113a-118a.
26. Nicolet. *Nicolet FT-IR Spectrometer*. Available from: http://www.thermo.com/com/cda/product/detail/0,1055,115542,00.html.
27. Thermo. *OMNIC Software*. Available from: http://www.thermo.com/com/cda/product/detail/0,1055,1000001344622,00.html.

Chapter 3 Preparation of Germanium Substrates

The cleanliness of germanium substrates is very crucial in the fabrication of Ge-based MOSFET devices as it would be for any state of the art semiconducting material. In addition to impurities, some oxides of Ge affect the quality of high-k film growth as well as the electrical properties of the resulting device. In this chapter, we compare the results of different wet chemical cleaning methods and study surface passivation with hydrogen and sulfur in order to find a better way to prepare Ge substrates for high-k ALD growth and subsequent fabrication of high quality Ge-based MOSFETs.

Section 3.1 Cleaning of Germanium Substrates

The surface cleaning process has been one of the obstacles to film growth on Ge. For Si and III-V substrates like GaAs, the procedures to prepare a clean surface usually involve three steps: (1) degreasing, (2) chemical etching to remove native oxide and other impurities and (3) growth of a protective oxide layer (which is often removed, for example by annealing, in a controlled environment right before the film growth) to ensure a clean substrate. However, with the exception to the first step, which is usually performed with successive ultrasonic baths in acetone and methanol, step 2 and 3 are quite challenging for Ge. The removal of native oxides and other impurities from Ge substrates is not as easy as it is for Si. The standard “RCA clean” method [1], commonly used on

Si, is not suitable on Ge because it is inefficient in removing carbon, the most common impurity found on Ge, and it leaves noticeable marks on the surface. Moreover, the formation of a non-permeable protective oxide layer on germanium has been considered impractical because GeO_2 has a high water-solubility (5.2 g/L) and can even be dissolved with moisture from air [2].

Many different wet-chemistry recipes have been utilized in order to remove the native oxide layer and impurities from Ge surface. So far none of these recipes has given satisfactory results [3-5] in the production of MOSFET quality surfaces and many of them have resulted in significant residual carbon [4]. XPS is a very useful technique to investigate the effects of different wet chemical treatments on Ge surface; my XPS results are presented below. In this study, all photoelectron peaks are fitted with a Gaussian band after the inelastic background intensity is subtracted. In the following discussion, all Ge samples are first degreased in ultrasonic baths of acetone and methanol, for 15 minutes (each), and then different wet chemical treatments are applied. After each treatment, the Ge samples are blown dry with nitrogen (N_2) and analyzed.

3.1.1 Native Oxides

Figure 3-1 shows the XPS Ge 3d core-level spectrum of an as-received Ge(100) sample and the number in parenthesis for each peak denotes the corresponding chemical shift in eV. The major peak at 29 eV is responsible for the elemental Ge originating from the substrate [3, 6, 7]. The peak at 32.5 eV,

with a chemical shift of 3.5 eV toward higher binding energies, is in good agreement with previous studies for GeO_2 [7, 8]. In order to obtain the best fit, one also needs to include two small peaks at 31.2 eV and 30.5 eV. The peak at 31.2 with a chemical shift of +2.2 eV suggests that this corresponds to GeO [3, 7, 8]. The other peak at 30.5 eV with a +1.5 eV chemical shift is then assigned to GeC [9-11]. The decomposition of the Ge 3d XPS peaks shows that the native oxide consists mostly of GeO_2 and a small amount of GeO.

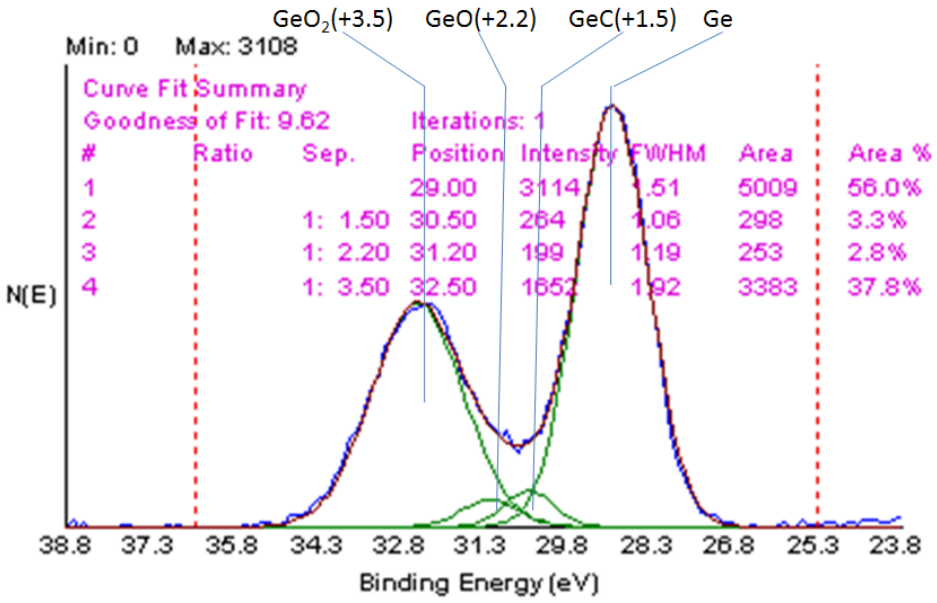


Figure 3-1: Ge 3d XPS spectrum from as-received Ge(100) wafers.

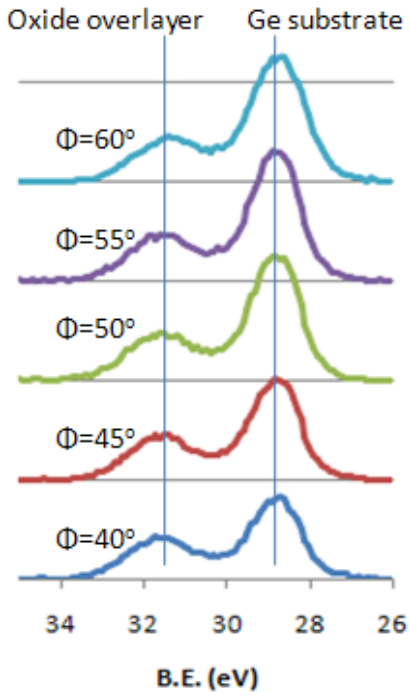


Figure 3-2: Ge 3d XPS spectra of an as-received Ge(100) sample at different take-off angles.

The thickness of the native oxide is determined by angular resolved photoelectron spectroscopy (ARPES) as discussed above in Section 2.1. Figure 3-2 shows a set of Ge 3d XPS spectra at different photoelectron take-off angles. The small take-off angle measurements detect the photoelectron originating from the surface. Therefore, the peak intensity ratio of the overlayer to the substrate becomes larger when the take-off angle decreases. The thickness of the overlayer can be calculated from this ratio and the take-off angle as shown in Section 2.1.3. For simplicity, one can assume that the oxide overlayer consists only of GeO_2 because the amount of GeO and GeC is much less than that of GeO_2. In the calculation, the inelastic mean free path λ of Ge 3d photoelectrons in GeO_2 is 3.3 nm, which is the average of the reported experimental values [3, 12, 13]. The calculated thickness of the native oxide is 1.53 nm on Ge(100)

(Figure 3-3), and 2.75 nm on Ge(111) (not shown) which are in good agreement with the previous studies: 1.8 nm on Ge(100) [3, 10] and 2-3 nm on Ge(111) [14].

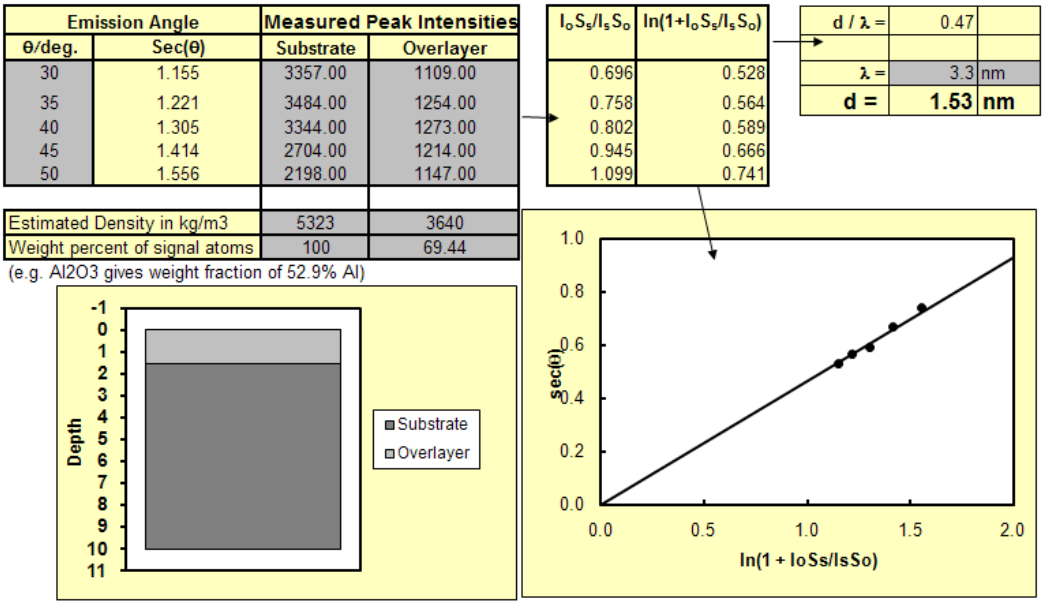


Figure 3-3: Calculation of the thickness of the oxide overlayer on Ge(100).

3.1.2 Removal of Native Oxide and Carbon

Because water is often present in chemical solutions and GeO_2 has a high water-solubility, the effects of water on a Ge surface need to be well understood. A degreased Ge sample was rinsed with running de-ionized water (DIW, 18.2 MΩ cm) for 1 minute and then blow-dried with N_2 before being loaded into the XPS chamber. The Ge 3d XPS spectrum in Figure 3-4 shows that the GeO_2 component completely disappears due to the DIW rinse. This implies that the majority of the Ge native oxide must be either amorphous or hexagonal GeO_2 which are both highly water-soluble but not the insoluble tetrahedral specie [2].

However, the two small GeO and GeC peaks are still present and the DIW rinse alone cannot remove all of the germanium sub-oxide and carbides.

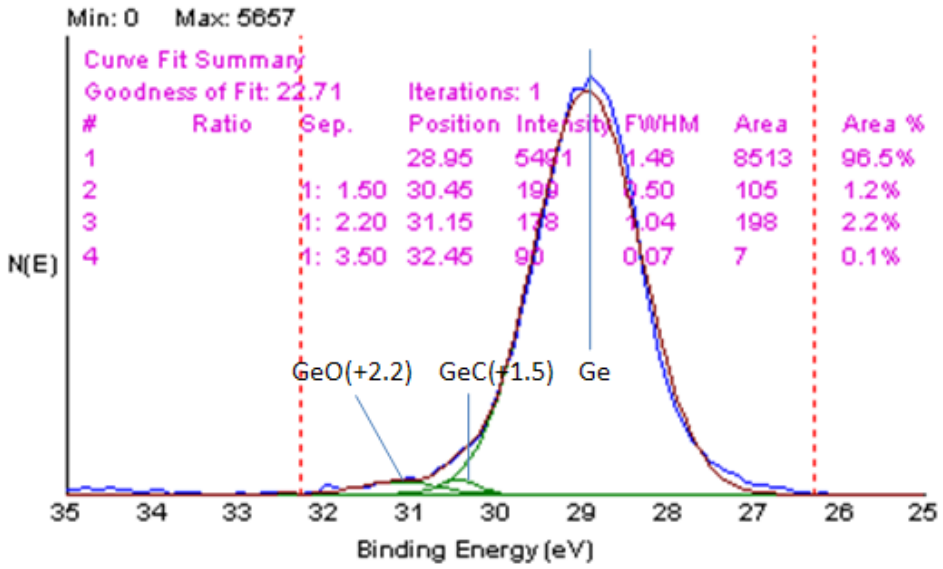


Figure 3-4: Ge 3d XPS spectrum from a Ge(100) wafer after DIW rinsing.

Hydrofluoric acid (HF) is often used to etch the native oxide layer and produce hydrogen terminated surfaces on Si and Ge wafers. The use of concentrated HF acid solutions (49%) on Ge should be avoided because such concentrated HF solutions increase the roughness of the surface [15, 16] without further decreasing the amount of sub-oxide [17]. The formation of the rougher surface is due to the Ge back-bond breaking during HF etching [15]. To reduce this effect, HF is diluted to a concentration of 2% to 10% with either DIW or hydrogen peroxide (H_2O_2). It has been determined that cyclic HF/DIW rinses are effective in removing the native oxide [14]. For the treatment of cyclic HF/DIW rinses, Ge samples are rinsed in DIW, dipped in HF acid solution and rinsed in DIW again. This procedure is repeated for 3 to 5 times in order to peel off the

oxide layer and/or to remove several atomic layers of Ge. Figure 3-5 shows the Ge 3d XPS spectrum from a Ge(100) sample etched in 10% HF solution for 10 minutes. Although GeO_2 is completely removed, the peaks of GeO and GeC are still present. In fact, it has been shown that HF treatment always leaves behind sub-oxides and carbides [15, 17].

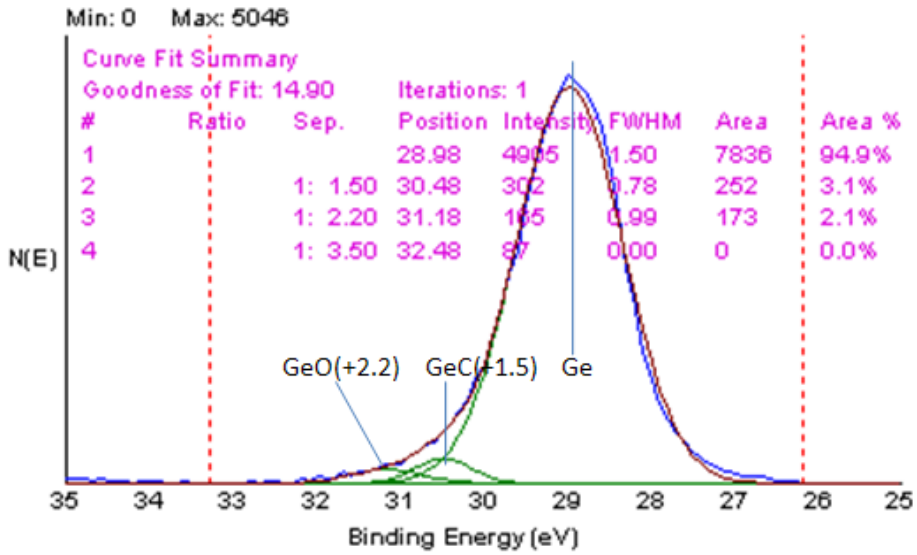


Figure 3-5: Ge 3d XPS spectrum from a Ge(100) wafer after the 10% HF etching.

The C 1s XPS spectra of the as-received, DIW-rinsed and HF-etched Ge samples are shown side-by-side in Figure 3-6. The most intense peak at 285.5 eV represents the C-C and C-H bonds [11, 18, 19]. The C-O bond is reported to induce a +1.1 eV chemical shift and is responsible for the broad peak at 286.6 eV [18]. The large full width at half maximum (FWHM) of this peak indicates that the chemical composition is complicated. Because of the small amount of GeC on the sample and the high carbon background, the peak corresponding to Ge carbides with a chemical shift of --1.7 to -3 eV [11] with respect to the C-C peak

is not observed. However, this does not imply the absence of Ge carbides. The C 1s peaks are reduced on both the DIW-rinsed and HF-etched sample. This is because when GeO_2 is removed, the hydrocarbon trapped inside is also removed from the surface.

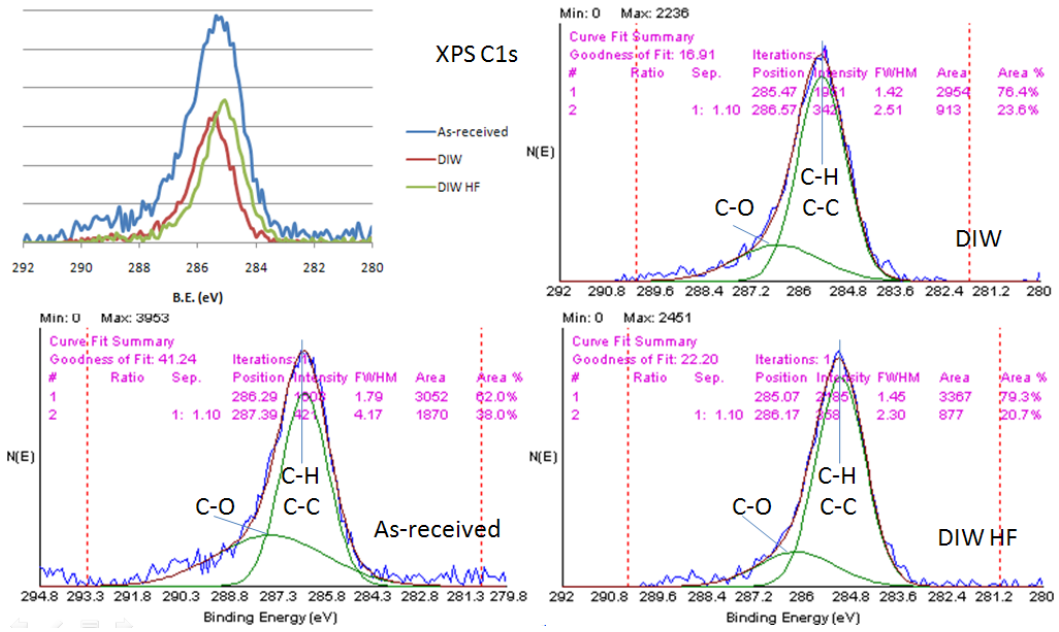


Figure 3-6: C 1s XPS spectra from as-received, DIW-rinsed and HF-etched Ge(100) samples.

Other common chemicals used to etch the Ge native oxide include ammonia (NH_4OH), hydrochloric acid (HCl), and sulfuric acid (H_2SO_4). The advantage of NH_4OH and HCl is the preservation of the original morphology/roughness [16, 20, 21]. A very uniform surface can be attained by a 5-minute NH_4OH (27%) etch because NH_4OH has a slow etching rate of which is even slower than DIW [16, 21]. Concentrated HCl (20%) is more effective at remove metal contamination than HF (2-20%) [17], but HCl-treated surfaces attract more contaminants than HF-treated ones [15]. A diluted H_2SO_4 solution (H_2SO_4:DIW = 1:7) is reported to remove metals as well as hydrocarbons

effectively [21]. However, none of these etch processes alone can lead to an oxygen and carbon free surface without further vacuum annealing [15].

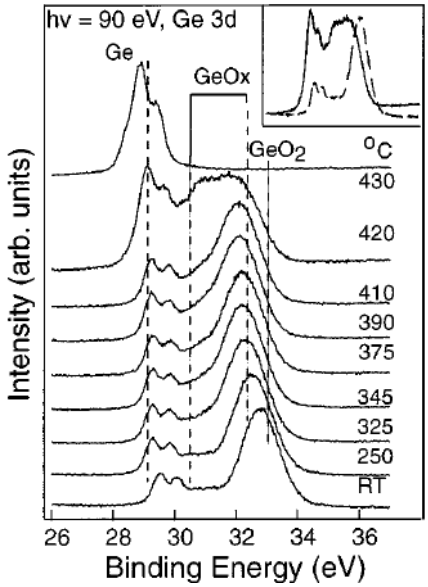


Figure 3-7: Ge 3d XPS spectra as a function of annealing temperature [22].

Vacuum annealing is a common cleaning method to desorb oxygen and carbon from the surface. However, even with annealing in UHV, to obtain a smooth sub-oxides- and carbides-free Ge surface is not as easy as it is for Si. Figure 3-7 shows Ge 3d XPS spectra as a function of annealing temperature. As the annealing temperature is raised, the amount of GeO_2 decreases and the amount of GeO increases. This suggests the occurrence of the following surface transformation: $GeO_2 + Ge \rightarrow GeO$ [7, 8, 22, 23]. Even though the oxygen is totally removed after vacuum annealing at 450-480 ℃ for 30 minutes, there is always some carbon left on the surface from XPS [3, 15], AES (Auger Electron Spectroscopy) and EELS (Electron Energy Lose Spectroscopy) [3] studies.

3.1.3 Protective Chemical Oxides

Since it is difficult to completely remove oxide and carbon from Ge substrates, different approaches involving the transformation of these into other chemical species which are easier to remove have been investigated, for example: (1) GeO → GeO_2 and (2) GeC → CO_2 [3, 16, 21, 24]. This is usually done with either UV/ozone or wet chemical oxidation. In UV/ozone oxidation, degreased Ge samples are first rinsed with DIW to remove GeO_2 and then oxidized in the presence of ozone, produced from an ultraviolet (UV) lamp, in either a vacuum chamber or a closed oxygen-purging box [3, 24]. The thickness of the oxides formed by UV/ozone is reported to be 1 nm [24] to 1.8 nm [3] determined by angular resolved photoelectron spectroscopy (ARPES). XPS spectra show that the complete oxide desorption takes place after a vacuum annealing at 350 ℃ for 30 minutes and C 1s, O 1s and chemically shifted Ge 3d oxide peaks are not detectable resulting in a clean Ge surface (Figure 3-8).

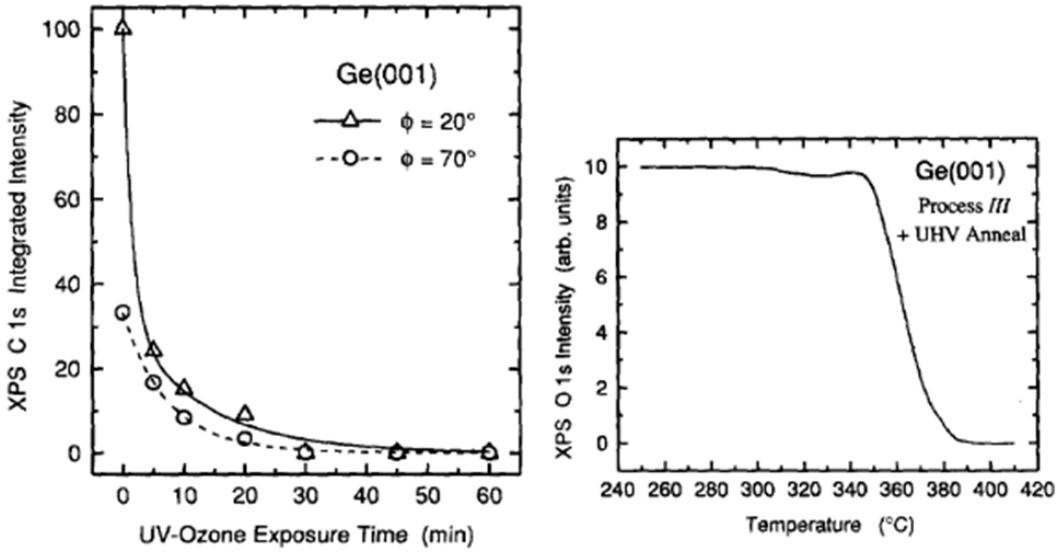


Figure 3-8: C 1s (left) and O 1s (right) XPS spectra from Ge(100) after UV/ozone exposure and annealing [3].

H_2O_2 is often used in wet chemical oxidation on a Ge surface. Since H_2O_2 usually contains some impurities, including organic compounds, H_2O_2 should be diluted with either a base or an acid [25]. Okumura has compared the oxidation effect on Ge using H_2O_2/H_2O (1/10) and $NH_4OH/H_2O_2/H_2O$ (0.5/1/10) [16]. It is shown that no protective oxide can be formed with H_2O_2 solution diluted in H_2O (H_2O_2:H_2O=1:10) because water etches the chemical oxide. On the other hand with the addition of NH_4OH, chemical oxide remains due to the slower etching rate of NH_4OH than that of DIW. In this work, we have compared chemical oxides formed by concentrated H_2O_2 and a mixture of H_2SO_4/H_2O_2 (4/1). The reasons for using H_2SO_4 with H_2O_2 for oxidation are: (1) H_2SO_4 helps remove hydrocarbon [21] and (2) the oxidation in the acid-base reaction is stronger and more effective in converting GeO and GeC. Degreased Ge samples were first rinsed in DIW to remove GeO_2 and then dipped into either concentrated H_2O_2 or

a mixture of H_2SO_4/H_2O_2 (4/1) for 10 minutes. The Ge 3d XPS spectra from the Ge samples with chemical oxides formed by these two solutions are shown in Figure 3-9 and Figure 3-10.

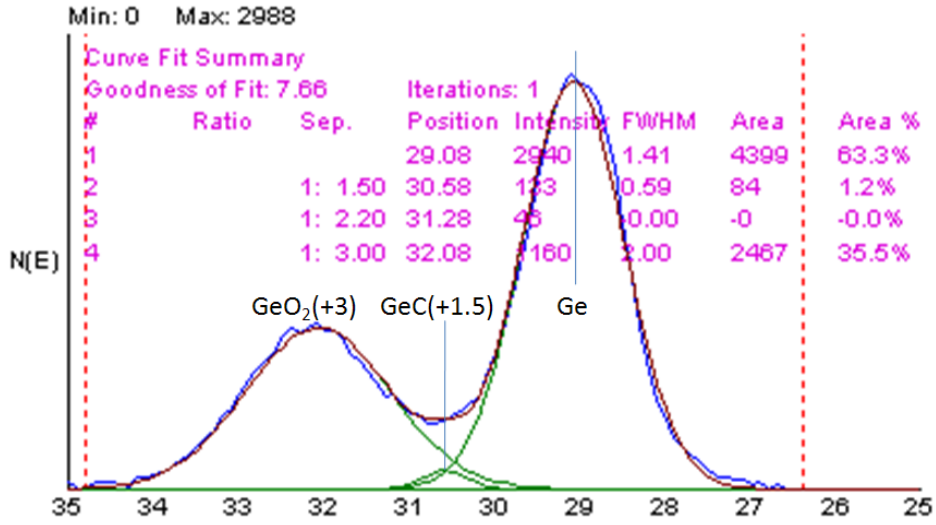


Figure 3-9: Ge 3d XPS spectrum from a Ge(100) sample with a chemical oxide formed by concentrated H_2O_2.

Comparing Figure 3-9 and Figure 3-10, GeO signals are not detectable and the intensities of the GeC peaks are small. One of the major differences between these two methods is the thickness of the chemical GeO_2 layer. ARPES has been performed to determine the thickness of the chemical oxides in each case. While the thickness of the GeO_2 layer formed by the concentrated H_2O_2 is 2.1 nm, compared to 1.9 nm reported in the previous studies [16, 21], the H_2SO_4/H_2O_2 mixture grows a much thicker GeO_2 layer (~12.4 nm). Another difference is the amount of remaining carbon on the surface. The intensity of the C 1s peak, from a cyclic HF/DIW/H_2O_2 treated Ge sample, is still ~38% larger compared to that of a H_2SO_4/H_2O_2 treated sample.

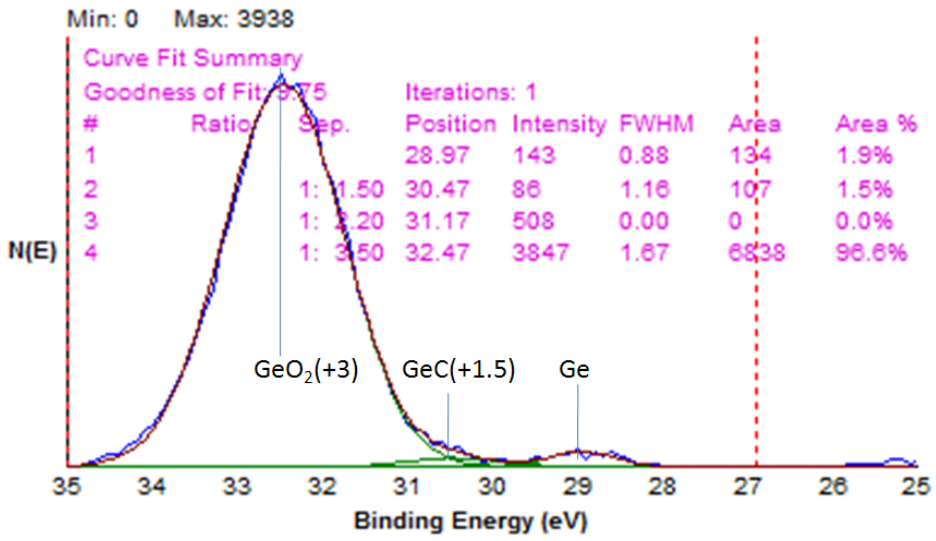


Figure 3-10: Ge 3d XPS spectrum from a Ge(100) sample with chemical oxide formed by H_2SO_4/H_2O_2.

The comparisons of the C 1s peaks from the Ge samples undergoing different wet chemical cleaning methods are shown in Figure 3-11. The H_2SO_4/H_2O_2-treated Ge samples appear to contain the least amount of carbon.

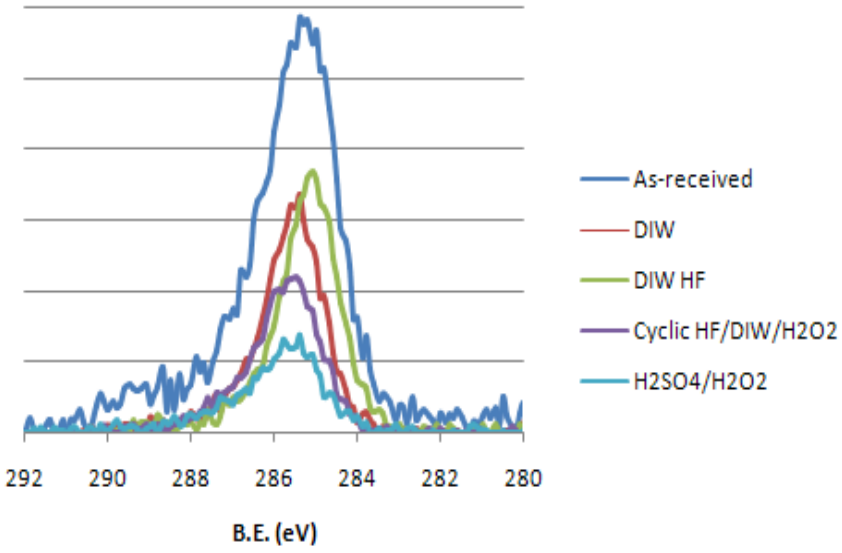


Figure 3-11: Comparison of C 1s XPS peaks with different cleaning methods.

The formation of a chemical oxide not only reduces the amount of carbon on the Ge surface but also helps protect the surface from further carbon contamination. Figure 3-12 shows C 1s XPS spectra from two sets of Ge samples which have a chemical oxide formed on the surface using two different treatments: cyclic HF/DIW/H_2O_2 and H_2SO_4/H_2O_2. If the chemical oxide is removed either by a DIW rinse or by HF etching, the intensity of the C 1s peak will increase. Interestingly, after the chemical oxides are removed, the intensity of the C 1s peak from the H_2SO_4/H_2O_2-treated Ge sample increases much more (~120%) than that from the cyclic HF/DIW/H_2O_2 rinsed sample (26%). This is most likely due to H_2SO_4/H_2O_2 oxidation removing more carbon from the Ge surface than cyclic HF/DIW/H_2O_2 rinses. Once the protective oxide is removed, the amount of carbon increases to the same saturated level due to environmental contamination.

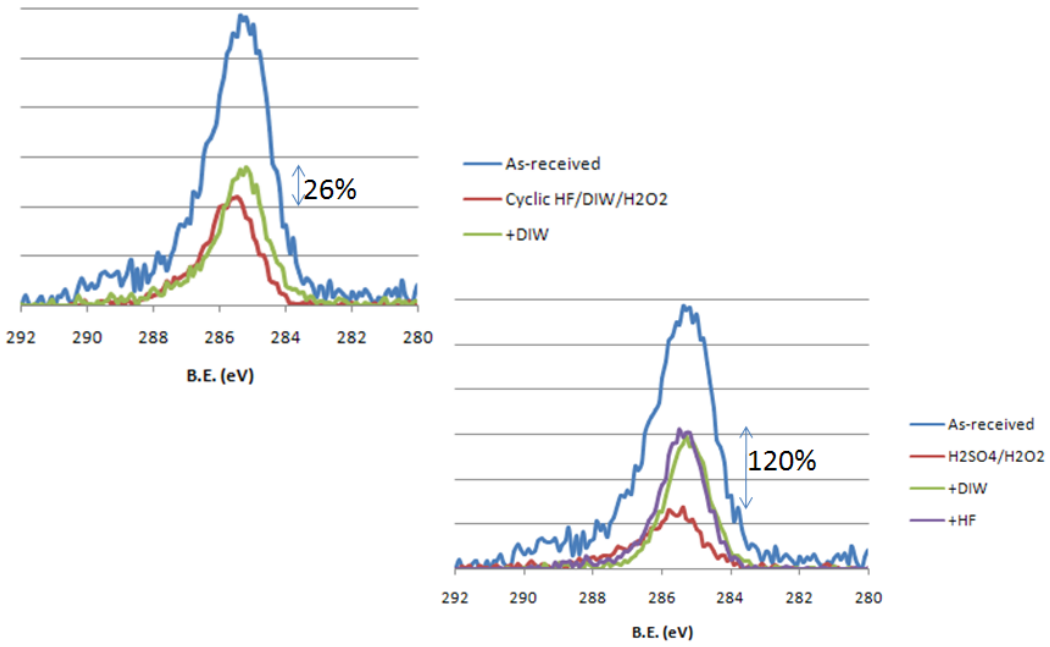


Figure 3-12: Intensity changes of C 1s XPS peaks before and after the removal of chemical oxide.

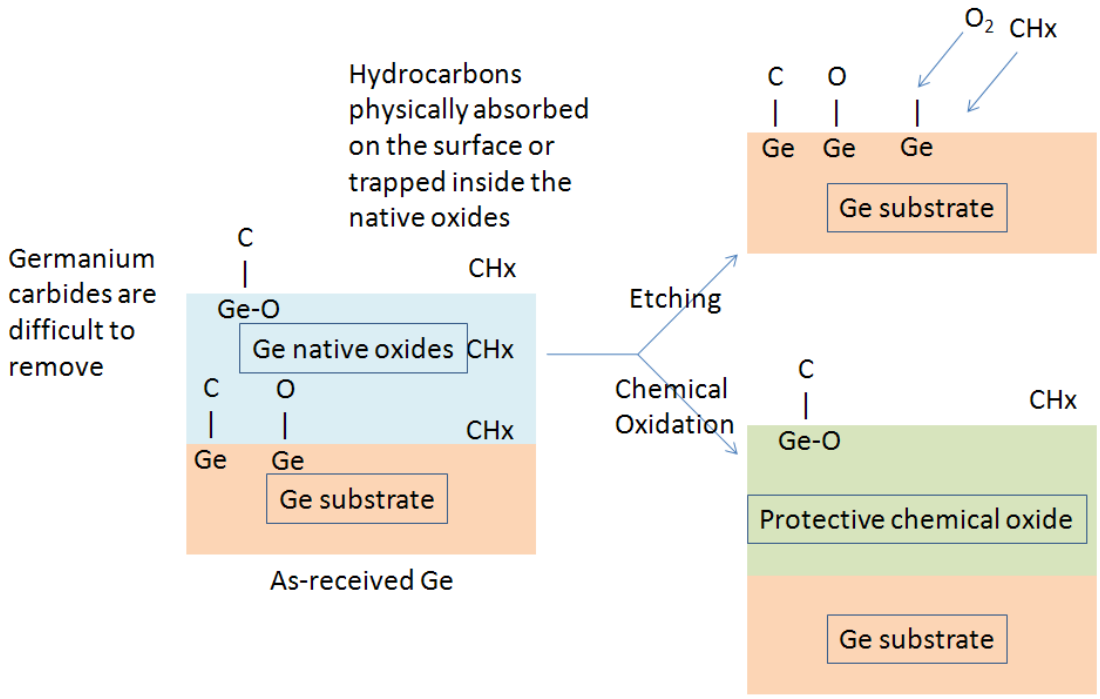


Figure 3-13: Etching and chemical oxidization on as-received Ge wafers.

Section 3.2 Passivation on Germanium Substrates

In this work, two different methods of passivating Ge substrates have been investigated: hydrogen-termination and sulfur passivation. Both of these methods are accomplished with wet chemistry, because it is more desirable in industry for the simplicity of this method, as well as its lower cost. Hydrogen terminated Ge surface produced by HF etch cleaning is studied as a comparison to sulfur passivation which is reported to be more stable in ambient [26].

3.2.1 Passivation with Hydrogen

A hydrogen-terminated Ge surface can be prepared in an HF solution [14, 27]. Fourier Transform Infrared Spectroscopy (FT-IR) is a useful technique to study the formation of H-Ge as well as the quality of the H-terminated surface.

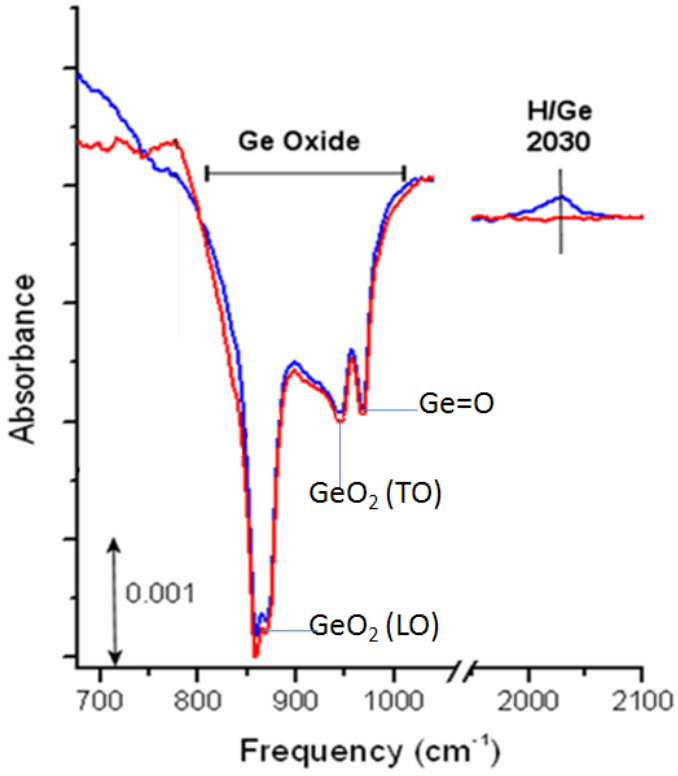


Figure 3-14: FT-IR spectra of a H-terminated Ge(100) sample (blue) vs. H_2SO4/H_2O_2-treated Ge sample followed by a DIW rise (red) using as-received Ge samples as a reference.

After two H_2SO_4/H_2O_2-oxidized Ge samples were prepared, one of them was etched with dilute HF (10%) for 10 minutes to produce a hydrogen-terminated surface and the other was rinsed with DIW to remove the chemical oxide. The FT-IR spectra using as-received samples as a reference are shown in Figure 3-14. A strong negative feature appears between 750 and 1050 cm^{-1}, corresponding to the removal of the Ge oxides. The three downward peaks in

this region are assigned to the LO and TO phonon modes of GeO_2 and the Ge=O stretch (980 cm^{-1}) [10]. The significant overlap of these two spectra implies that the chemical oxide formed after H_2SO_4/H_2O_2 must be soluble GeO_2 so that a DIW rinse can produce the same effect as the HF etch. This FT-IR result shows that H_2SO_4/H_2O_2 oxidation, together with HF etches or a DIW rinse, can effectively remove GeO_2 and GeO from the as-received Ge surface and is in good agreement with the previous XPS studies from Section 3.1. The positive peak around 2030 cm^{-1} confirms the formation of an H-terminated surface. However, the broadness and asymmetry of this absorbance band resulting from the stretching vibration of H-Ge, H_2-Ge and H_3-Ge implies that the H-terminated surface is atomically rough [10, 27].

To further understand the advantage of H_2SO_4/H_2O_2 oxidation on the Ge surface, H-terminated Ge samples were prepared with different cleaning methods: cyclic DIW/HF and H_2O_2 rinses. The comparison of absorbance FT-IR spectra is plotted in Figure 3-15. After 10 minutes in dilute HF, all three spectra show strong negative features between 750 and 1050 cm^{-1} corresponding to the removal of the Ge oxide. The downward peaks in the range of 1350-1550 cm^{-1} reflect the absence of hydrocarbon and only appear for H_2SO_4/H_2O_2- and H_2O_2-treated samples. Therefore, chemical oxidation methods with either H_2SO_4/H_2O_2 or H_2O_2 prove to be more effective in removing hydrocarbon from the as-received Ge surface than the cyclic DIW/HF rinses. Comparison of the integrated area shows that H_2SO_4/H_2O_2 removes more hydrocarbon than H_2O_2 alone. The positive peak around 2030 cm^{-1} is due to the H_x-Ge stretching vibration. In our

study, the H_x-Ge peak only appears on the HF-etched Ge samples with prior H_2SO_4/H_2O_2 oxidation. This suggests that how the Ge surface is cleaned determines the amount of remaining hydrocarbon on the surface and therefore affects the formation of H-Ge bonds.

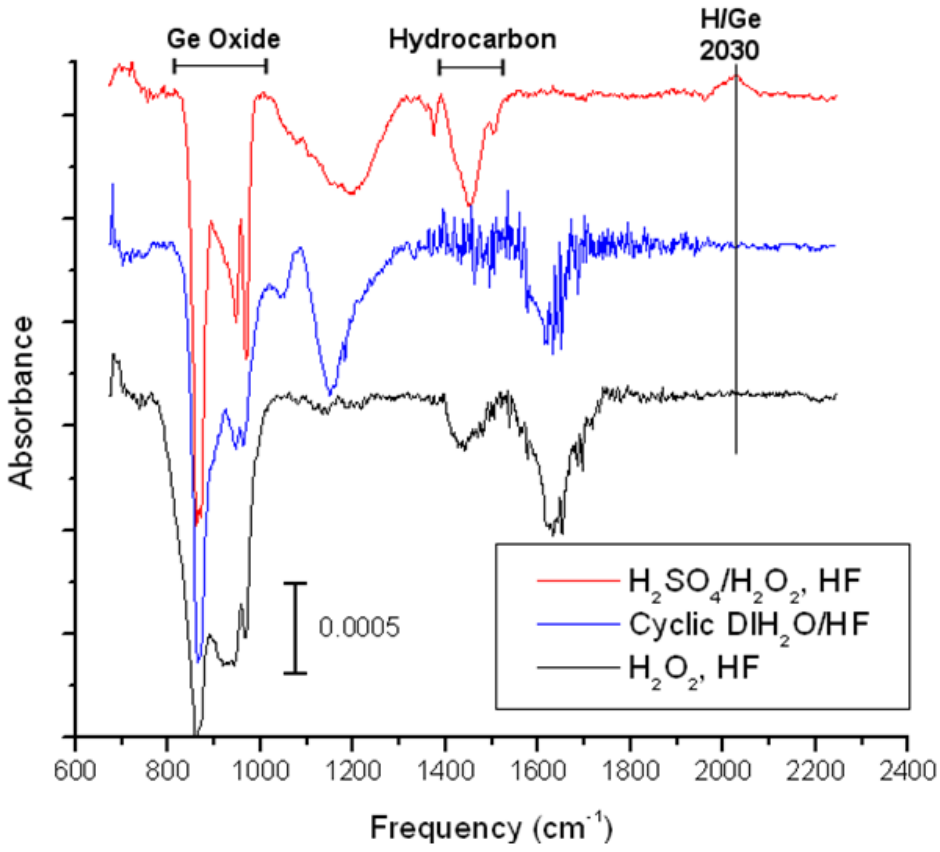


Figure 3-15: FT-IR spectra of HF-etched Ge(100) after a different wet chemical cleaning is applied.

Successive FT-IR spectra were taken in order to study the stability of an H-terminated Ge(100) surface both in air and in N_2 (Figure 3-16). Nearly all H_x-Ge bonds are removed in the first 100 minutes in air, and therefore the H-terminated surface is very unstable which has also been observed in a previous study [26]. In the N_2 environment, the H-terminated surface can be preserved for

a longer period. Although it decreases slowly, the H_x-Ge peak is still present 800 minutes after the H-terminated sample was prepared.

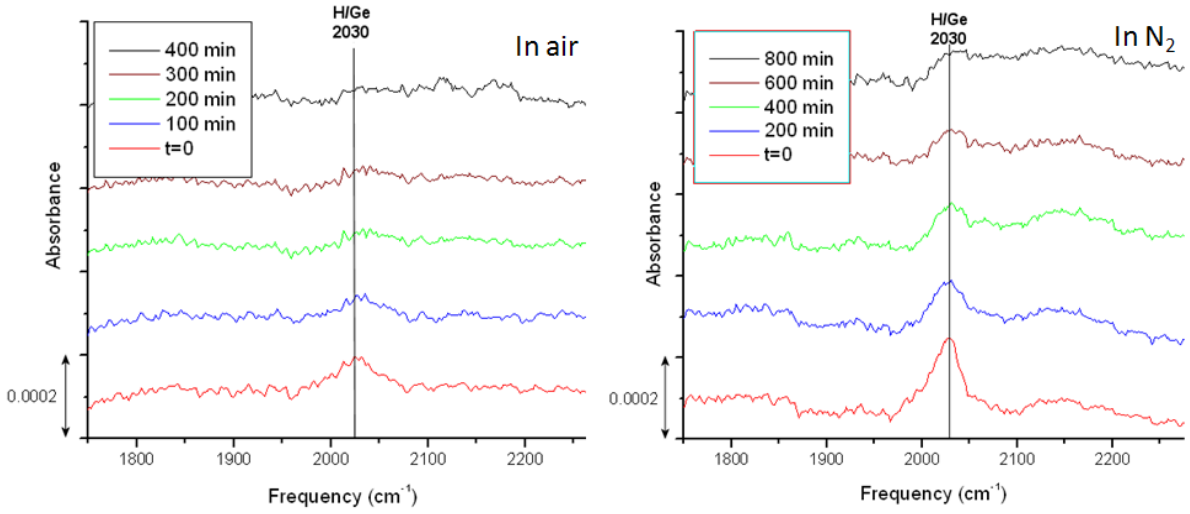


Figure 3-16: FT-IR spectra to show the stability of H-terminated Ge(100) in air and in N2.

3.2.2 Passivation with Sulfur

It has been demonstrated that 1 ML of elemental sulfur can be deposited on Ge(100) to form an ideal 1x1 S-terminated surface in UHV [28, 29]. To prepare a sulfur passivated Ge surface with wet chemistry, aqueous ammonia sulfide $(NH_4)_2S$ (50%) is used [30, 31]. After being heated to 70 ℃ for 15 minutes, the Ge sample is rinsed with methanol to remove excess $(NH_4)_2S$ and blown dry with N_2. Saturated solutions of thioacetamide and thiourea (Figure 3-17) were also used in an attempt to obtain a S-passivated Ge surface. However, only the $(NH_4)_2S$-treated sample shows a significant S 2p peak in Figure 3-18. Even with a longer heating duration (up to 30 minutes) at a higher

temperature (100 ℃), neither thioacetamide nor thiourea can produce S-passivated Ge surfaces.

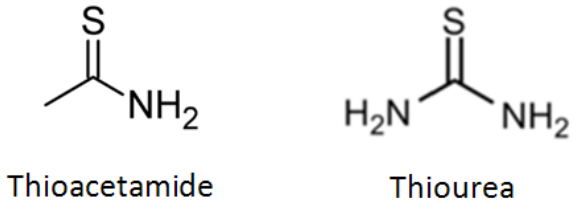


Figure 3-17: Molecular structure of thioacetamide and thiourea.

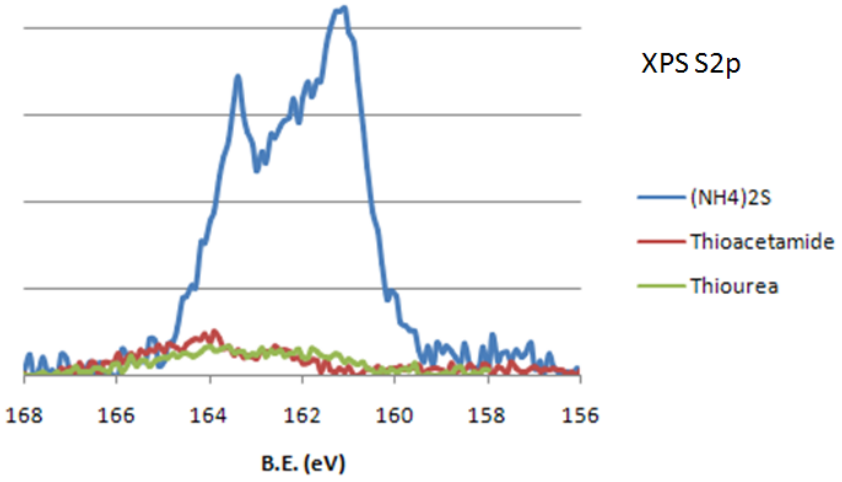


Figure 3-18: S 2p XPS spectra from Ge(100) treated in $(NH_4)_2S$, thioacetamide and thiourea solution.

In our study, Ge samples which are later used for high-k ALD growth in Ge-based MOSFETs are first pretreated with H_2SO_4/H_2O_2 to remove the native oxide and grow a protective chemical oxide, and then heated in a $(NH_4)_2S$ solution to form a sulfur passivation layer on the surface. The advantages of doing so will become clear later in this section. Figure 3-19 shows Ge 3d XPS spectrum of a Ge sample which has undergone such a treatment. Two major differences are observed in Figure 3-19 when comparing the Ge 3d spectrum

from a H_2SO_4/H_2O_2-treated sample. First, the peak with a 3 eV chemical shift corresponding to GeO_2 disappears which implies that the chemical oxide is completely removed by a hot aqueous $(NH_4)_2S$ solution. Second, a broad peak with a chemical shift of 0.66 eV is present due to the surface Ge atoms bonded to S atoms. In previous studies, this has been attributed to one layer of bridge-bonded S atoms on the Ge surface [28, 29].

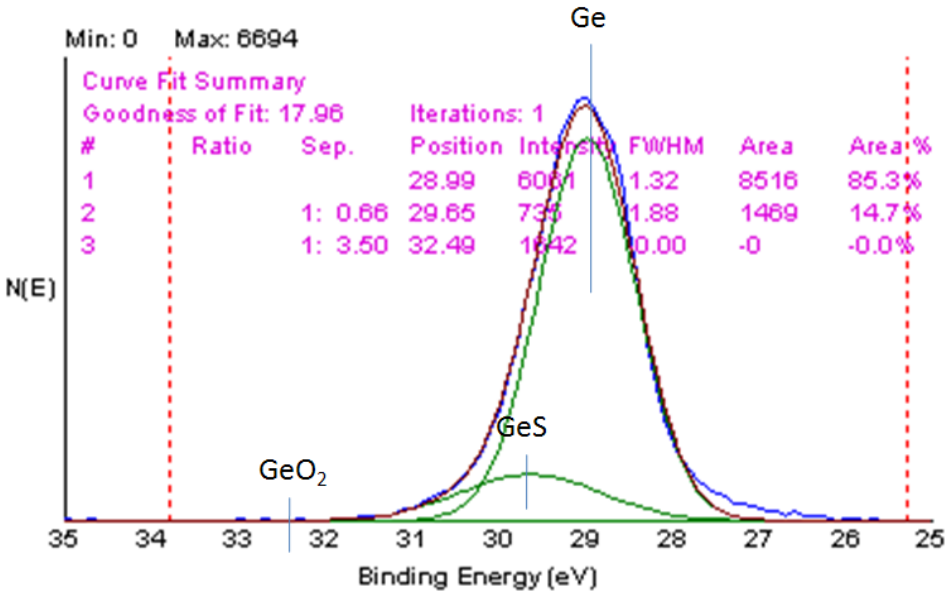


Figure 3-19: Ge 3d XPS spectrum from a $(NH_4)_2S$-treated Ge(100) sample.

Because the mean-free-path associated with the Ge 2p core-level photoelectrons is smaller, the Ge 2p peak is more sensitive to the surface change than the Ge 3d peak. Therefore, the Ge 2p region of XPS spectra is used to study the removal of Ge oxides and the change of chemical states on the surface. Figure 3-20 shows the Ge 2p XPS spectra from the same S-passivated Ge sample. In the inset in the lower right corner of Figure 3-20, a Ge 2p spectrum of the S-passivated Ge sample is compared to that of an as-received

sample. The GeO_2 peak disappears after the successive wet chemical treatments in H_2SO_4/H_2O_2 and $(NH_4)_2S$. The numerical deconvolution of the Ge 2p peak shows that three peaks with non-zero chemical shifts exist in addition to the elemental Ge in the bulk. The one with the largest chemical shift (+2.8 eV) is due to GeO_2 [26] and accounts for 2.5% of the total integrated peak area. Because of the strong S 2p peak (Figure 3-18) and the negligible O 1s peak (not shown), the other two peaks which have smaller chemical shifts must correspond to Ge atoms that are bonded to S atoms on the surface. According to Weser, each S-Ge bond induces a chemical shift of 0.33 eV in the binding energy of Ge 2p photoelectrons [28]. Therefore, these two peaks with chemical shifts of +0.66 and +1.28 eV are assigned to the doubly sulfur coordinated Ge (GeS) and the quadruply sulfur coordinated Ge (GeS_2) respectively. The thickness of the sulfur passivation layer is estimated to be 0.16 nm with ARPES and indicates that about a monolayer of S has been formed on the Ge surface. The mean free path of Ge 2p photoelectrons in GeS_2, $\lambda = 0.51$ nm [28], was used in the calculation.

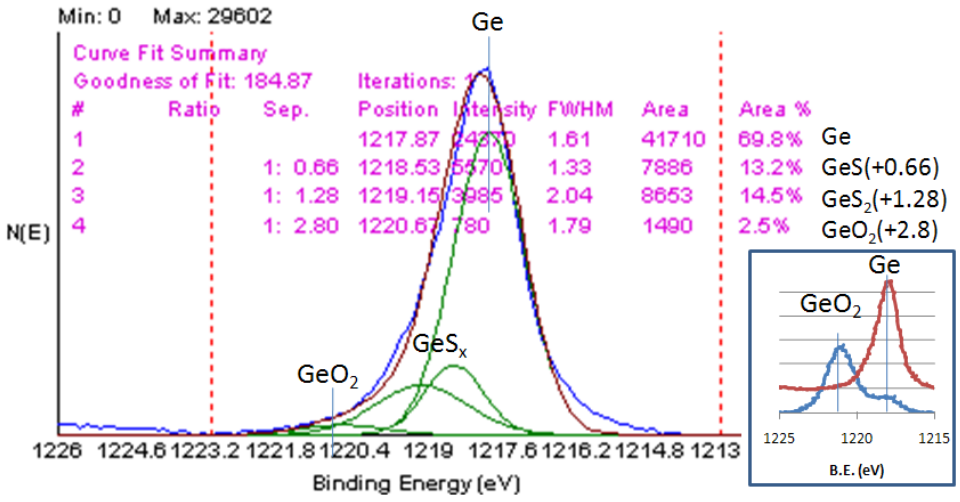


Figure 3-20: Ge 2p XPS spectrum from a S-passivated H_2SO_4/H2O2-treated Ge(100) sample. The inset shows the comparison of the same sample (red line) with an as-received sample (blue line).

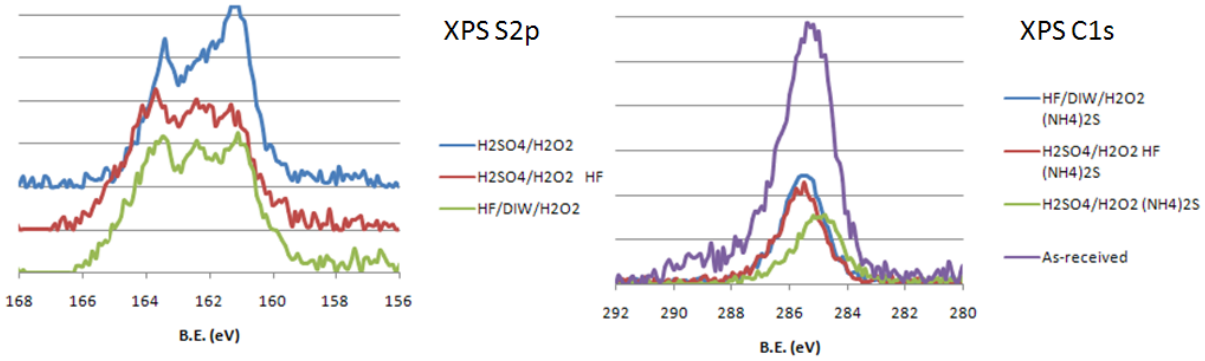


Figure 3-21: S 2p and C 1s XPS spectra from S-passivated Ge samples with different cleaning pretreatments.

To show the advantage of using H_2SO_4/H_2O_2 to clean the Ge surface, the following cleaning treatments are applied to as-received Ge samples before S-passivation with $(NH_4)_2S$: cyclic HF/DIW/H_2O_2 rinses, H_2SO_4/H_2O_2 oxidation followed by HF etches and H_2SO_4/H_2O_2 oxidation without following HF etches. The XPS S 2p and C 1s spectra are shown in Figure 3-21. All three show strong

S 2p signals with similar intensities, but the amount of carbon is different. Table 3-1 lists the atomic concentration (%) of carbon, oxygen, germanium and sulfur for these samples obtained from their XPS C 1s, O 1s, Ge 3d and S 2p peaks with the XPS atomic sensitivity factors used in the calculation: 0.25, 0.66, 0.38 and 0.54 respectively [32].

The S-passivated Ge sample pretreated with H_2SO_4/H_2O_2 oxidation has the least amount of carbon, 10% lower than the other two. We believe the remaining carbon, which accounts for 20.4% on the sample, might come from the surface hydrocarbons absorbed during the sample transfer and the background in the XPS system. But, if HF etches are applied after H_2SO_4/H_2O_2 oxidation, the carbon amount increases. This has been seen in the previous section, because the removal of the protective chemical oxide makes the cleaned Ge surface more vulnerable to carbon contamination. Since it has been shown that $(NH_4)_2S$ can remove the chemical oxide, this HF etch should be avoided. In the case of cyclic $HF/DIW/H_2O_2$ rinses, more carbon is left on Ge surface, as seen in the previous section, and follow-up sulfur passivation using $(NH_4)_2S$ does not help in removing carbon.

	C1s	O1s	Ge3d	S2p
HF/DIW/H_2O_2 $(NH_4)_2S$	30.2%	5.5%	51.8%	12.5%
H_2SO_4/H_2O_2 HF $(NH_4)_2S$	29.6%	6.2%	51.5%	12.7%
H_2SO_4/H_2O_2 $(NH_4)_2S$	20.4%	6.5%	61.5%	11.6%

Table 3-1: Comparison of XPS atomic concentration (%) of S-passivated samples with different cleaning.

In this chapter, we have demonstrated that H_2SO_4/H_2O_2 oxidation is the best method to remove the native oxides and reduce the Ge carbides from an as-received Ge surface because of its strong oxidation. It also forms a thick protective chemical oxide, mainly GeO_2, on the surface to prevent further carbon contamination. Sulfur passivation using hot $(NH_4)_2S$ solution not only removes this chemical oxide but also forms about one ML of S/Ge which helps passivate the Ge surface. These two wet chemical treatments together prepare a clean S-passivated Ge substrate for high-k ALD and fabrication of Ge-based MOSFETs.

Section 3.3 Reference

1. W. Kern and D.A. Puotinen, RCA Rev, 1970. **31**: p. 197.
2. J.C. Bailar, H.J. Emeieus, and R. Nyholm, *Comprehensive inorganic chemistry*. Vol. 2. 1973, Pergamon, Oxford: Elsevier.
3. X.-J. Zhang, G. Xue, A. Agarwal, et al., *Thermal desorption of ultraviolet–ozone oxidized Ge(001) for substrate cleaning.* The Journal of Vacuum Science and Technology A, 1993. **11**: p. 2553.
4. D.A. Kiewit, I.J. d'Haenens, and J.A. Roth, *Germanium surface cleaning—an Auger analysis.* Journal of The Electrochemical Society, 1974. **121**: p. 310.
5. K. Prabhakarana, T. Ogino, R. Hull, et al., *An efficient method for cleaning Ge(100) surface.* Surface Science, 1994. **316**(1-2): p. L1031-L1033.
6. T.-C. Chiang, *Core-level photoemission studies of surfaces, interfaces, and overlayers.* Critical Reviews in Solid State and Materials Sciences, 1988. **14**(3): p. 269.
7. K. Prabhakaran and T. Ogino, *Oxidation of Ge(100) and Ge(111) Surfaces - an Ups and Xps Study.* Surface Science, 1995. **325**(3): p. 263-271.
8. D. Schmeisser, R.D. Schnell, and F.J.H. A. Bogen, D. Rieger, G. Landgren and J. F. Morar, *Surface oxidation states of germanium.* Surface Science, 1986. **172**(2): p. 455.
9. J. Vilcarromero and F.C. Marques, *XPS study of the chemical bonding in hydrogenated amorphous germanium-carbon alloys.* Applied Physics a-Materials Science & Processing, 2000. **70**(5): p. 581-585.
10. S. Rivillon, Y.J. Chabal, F. Amy, et al., *Hydrogen passivation of germanium (100) surface using wet chemical preparation.* Applied Physics Letters, 2005. **87**(25): p. -.
11. C.Q. Hu, W.T. Zheng, H.W. Tian, et al., *Effects of the chemical bonding on the optical and mechanical properties for germanium carbide films used as antireflection and protection coating of ZnS windows.* Journal of Physics-Condensed Matter, 2006. **18**(17): p. 4231-4241.
12. J. Szajman, J.G. Jenkins, J. Liesegang, et al., Journal of Electron Spectroscopy and Related Phenomena, 1978. **14**: p. 41.
13. H. Gant and W. Monch, *Electron escape depths in germanium.* Surface Science, 1981. **105**(1): p. 217.
14. T. Deegan and G. Hughes, *An X-ray photoelectron spectroscopy study of the HF etching of native oxides on Ge(111) and Ge(100) surfaces.* Applied Surface Science, 1998. **123**: p. 66-70.
15. S.Y. Sun, Y. Sun, Z. Liu, et al., *Surface termination and roughness of Ge(100) cleaned by HF and HCl solutions.* Applied Physics Letters, 2006. **88**(2): p. -.
16. H. Okumura, T. Akane, and S. Matsumoto, *Carbon contamination free Ge(100) surface cleaning for MBE.* Applied Surface Science, 1998. **125**(1): p. 125-128.
17. J. Kim, S. Liu, S. Tan, et al., *Germanium surface cleaning with hydrochloric acid.* ECS Transactions, 2006. **3**(7): p. 1191.
18. Y.J. Zhu, N. Olson, and T.P. Beebe, *Surface chemical characterization of 2.5-mu m particulates (PM2.5) from air pollution in salt lake city using TOF-SIMS, XPS, and FTIR.* Environmental Science & Technology, 2001. **35**(15): p. 3113-3121.
19. P. Benzi, E. Bottizzo, C. Demaria, et al., *Amorphous nonstoichiometric Ge1-x-C-x : H compounds obtained by radiolysis-chemical vapor deposition of germane/ethyne or germane/allene systems: A bonding and microstructure investigation performed by x-ray*

photoelectron spectroscopy and Raman spectroscopy. Journal of Applied Physics, 2007. **101**(12): p. -.

20. T. Akane, J. Tanaka, H. Okumura, et al., *Preparation of high-quality Ge substrate for MBE.* Applied Surface Science, 1997. **108**(2): p. 303-305.
21. T. Akane, H. Okumura, J. Tanaka, et al., *New Ge substrate cleaning method for Si1-x-yGexCy MOMBE growth.* Thin Solid Films, 1997. **294**(1-2): p. 153-156.
22. K. Prabhakaran, F. Maeda, Y. Watanabe, et al., *Distinctly different thermal decomposition pathways of ultrathin oxide layer on Ge and Si surfaces.* Applied Physics Letters, 2000. **76**(16): p. 2244-2246.
23. K. Prabhakaran, F. Maeda, Y. Watanabe, et al., *Thermal decomposition pathway of Ge and Si oxides: observation of a distinct difference.* Thin Solid Films, 2000. **369**(1-2): p. 289-292.
24. S. Gan, L. Li, T. Nguyen, et al., *Scanning tunneling microscopy of chemically cleaned germanium (100) surfaces.* Surface Science, 1998. **395**(1): p. 69-74.
25. C.H. Bjorkman, H. Nishimura, T. Yamazaki, et al. *Ultraclean semiconductor processing technology and surface chemical and passivation*. in *Material Research Society Symposium Proceedings*. 1995. Pittsburgh, PA.
26. D. Bodlaki, H. Yamamoto, D.H. Waldeck, et al., *Ambient stability of chemically passivated germanium interfaces.* Surface Science, 2003. **543**(1-3): p. 63-74.
27. K. Choi and J.M. Buriak, *Hydrogermylation of alkenes and alkynes on hydride-terminated Ge(100) surfaces.* Langmuir, 2000. **16**(20): p. 7737-7741.
28. T. Weser, A. Bogen, B. Konrad, et al., *Photoemission surface core-level study of sulfur adsorption on Ge(100)* Physics Review B, 1987. **35**(15): p. 8184.
29. T. Weser, A. Bogen, B. Konrad, et al., *Chemisorption of sulfur on Ge(100).* Surface Science, 1988. **201**(1-2): p. 245.
30. G.W. Anderson, M.C. Hanf, P.R. Norton, et al., *The S-Passivation of Ge(100)-(1x1).* Applied Physics Letters, 1995. **66**(9): p. 1123-1125.
31. T. Maeda, S. Takagi, T. Ohnishi, et al., *Sulfur passivation of Ge (001) surfaces and its effects on Schottky barrier contact.* Materials Science in Semiconductor Processing, 2006. **9**(4-5): p. 706-710.
32. J.F. Moulder, W.F. Stickle, P.E. Sobol, et al., *Hand Book X-ray Photoelectron Spectroscopy*. 2nd ed. 1992, Eden Prairie, MN: Perkin-Elmer Corp., Physical Electronics Division.

Chapter 4 Atomic Layer Deposition of High-k Dielectrics

Because of its ability to control the thickness and conformality of deposited films (in principle to the monolayer level), atomic layer deposition is the main method used in this work to deposit thin films of high-k dielectrics on Ge and other seminconductor substrates. In this chapter, the criteria of choosing appropriate precursors are presented together with the experimental results from the films deposited in our home-made ALD system.

Section 4.1 Atomic Layer Deposition

Atomic Layer Deposition (ALD) technology, originally known as Atomic Layer Epitaxy (ALE), was developed and patented by Finnish researchers Suntola and Antson in the middle of 1970s for the fabrication of thin film electroluminescence (TFEL) displays where high quality insulating and luminescent films on large area substrates were required [1]. Today, ALD has become a useful tool in microelectronics for high permittivity (high-k) film growth for CMOS devices and dynamic random access memory (DRAM) capacitors, as well as for ferroelectrics, barrier materials, conductors such as metal gates [2, 3], catalysis, magnetic recording head technology, and protective and antireflective coatings [4].

4.1.1 Advantages of ALD Processes

The ALD processes and their applications have been frequently reviewed [5-9], recently by Puurunen [10, 11], as well as by Ritala and Leskelä [4]. Different from chemical vapor deposition (CVD) and physical vapor deposition (PVD), ALD is based on sequential and saturating surface reactions of the alternately applied precursors. To minimize gas phase reactions between the two precursor pulses, the precursor pulses are separated by inert gas purging and/or by evacuation of the reaction chamber. The growth in a cyclic manner easily enables thickness control and makes the film growth rate directly proportional to the number of reaction cycles instead of the reactant concentration or time of growth as in CVD and PVD.

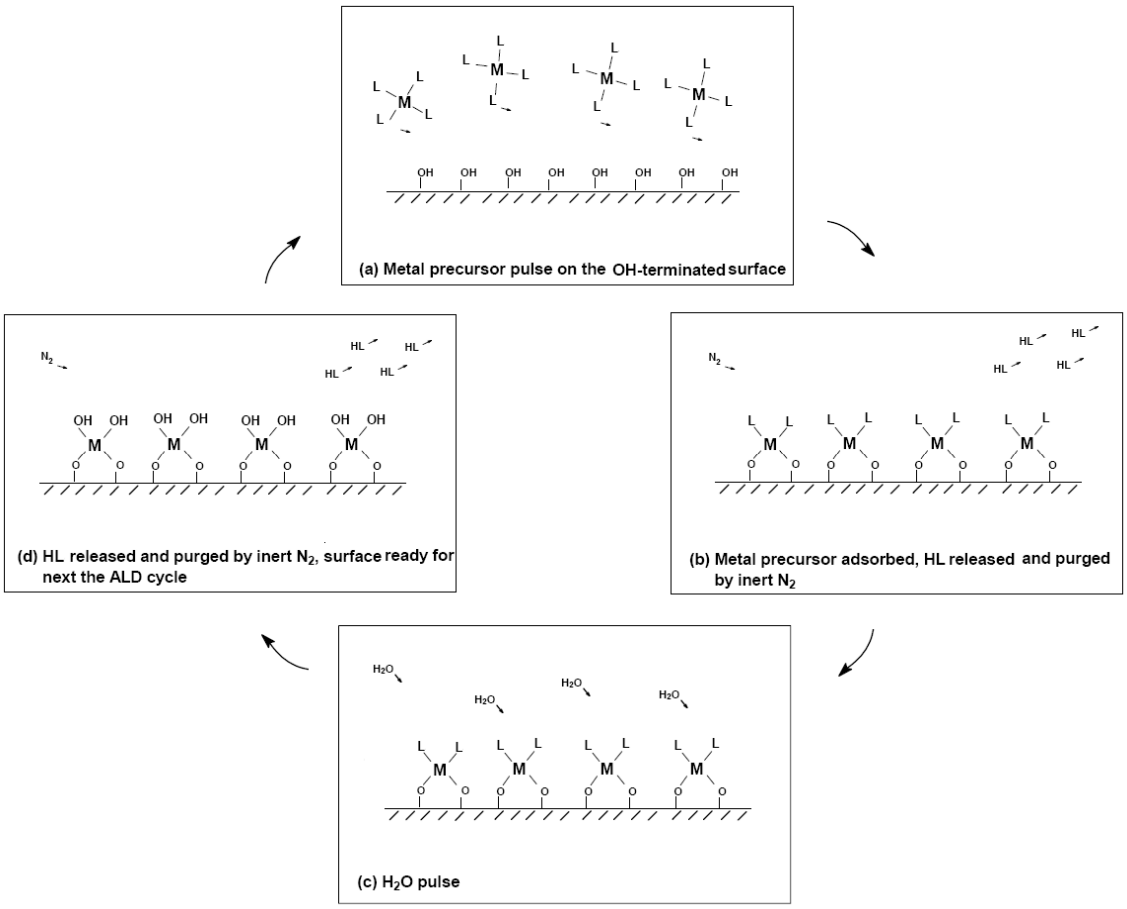


Figure 4-1: Schematic drawing of one ALD cycle (adapted from [12]).

In Figure 4-1, one simplified ALD cycle of a metal oxide deposition is shown to illustrate the principle of ALD. The substrate surface is first exposed to the vapor of a metal precursor and is saturated with the metal precursor on the available surface sites (assumed to be –OH groups) through chemisorption (a). After inert gas purging (here N_2) or evacuation to remove the excess precursor and ligand-exchange by-products (b), the surface is then exposed to the oxygen source (here H_2O) (c). The surface reaction produces the desired oxide film and is ready for the next ALD cycle after inert gas purging or evacuation of excess precursor and ligand-exchange by-products (d).

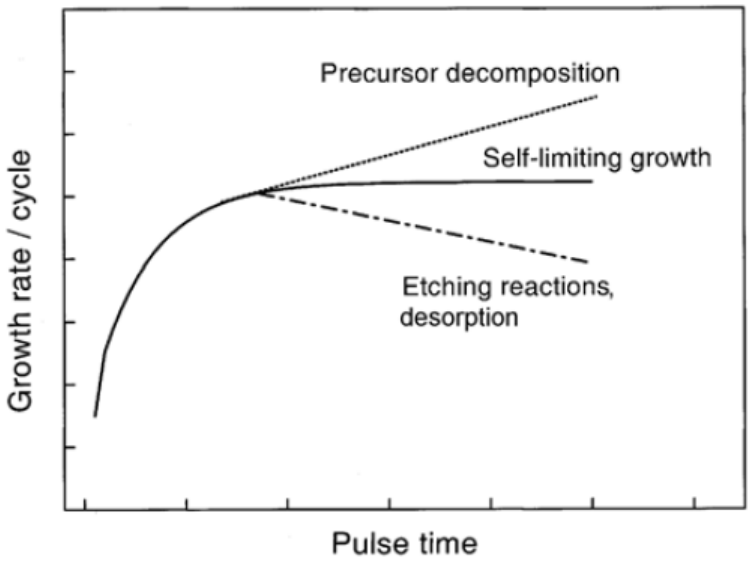


Figure 4-2: Different types of growth rate vs. precursor pulse time at a constant temperature [12].

The adsorption reaction in ALD of the precursors is a self-limiting process. The amount of deposited precursor molecules on the substrate surface is determined only by the number of reactive sites and is independent of the precursor exposure after the surface becomes saturated with the precursor. By working at a relatively low temperature, the precursor decomposition leading to a CVD-type growth mode can be avoided, the adsorption designed to saturate at a fractional monolayer, and the growth rate should then be independent of the precursor dose, assuming saturation (Figure 4-2). Ideally, the maximum growth rate is exactly one atomic layer per cycle. However, in most cases, the growth rate is a fraction of a monolayer (ML) due to steric hindrance by the absorbed precursor molecules and possibly by a limitation in the number of reactive surface sites (Figure 4-3). As the growth proceeds in a cyclic manner and the purging periods take some time, the ALD technique is rather slow compared to

CVD and PVD. In the application of ultrathin-film depositions, this is not a critical issue, although for films thicker than 10 nm, it may limit production speed.

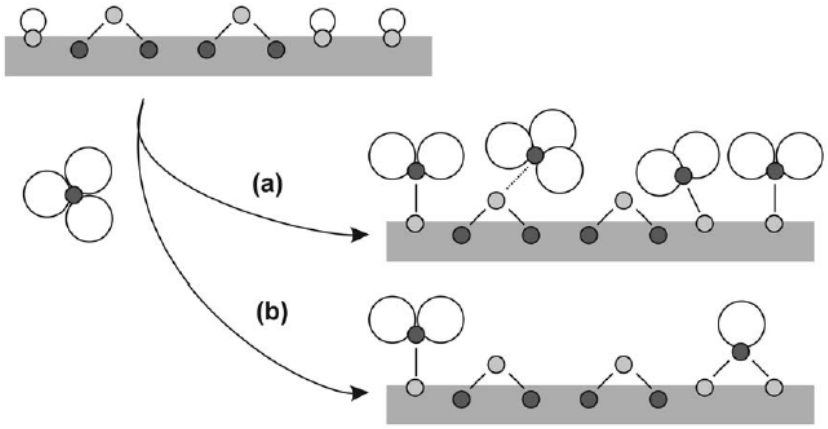


Figure 4-3: Factors that prevent full surface coverage of chemisorption: (a) steric hindrance of the ligands, and (b) number of reactive surface sites [10].

Another advantage of ALD is that the deposition can be performed at lower substrate temperatures. Since the adsorption of the precursor to the surface is mainly thermally driven, a so-called ALD temperature window with a constant deposition rate is usually observed [7, 13]. The substrate temperature must be high enough to prevent condensation of any of the reactants and to provide sufficient reactivity of the precursor. If condensation occurs during an ALD cycle, undesirable or uncontrollable reactions may occur during the second half cycle, resulting in the formation of porous and impure films. Therefore, a minimum substrate temperature is also required to proceed with the ALD process. There also exists a maximum substrate temperature for ALD. If the temperature is too high, the undesirable decomposition of a reactant may occur and CVD reactions will result, leading to rapid, uncontrolled deposition of a film.

Desorption of the precursor may also become more likely at higher temperatures and can result in a decreasing growth rate versus temperature. The ALD window is not a requirement for an ALD-type growth mode, but it is a desirable feature that leads to reproducibility of the film growth. The relations between the growth rate and temperature in ALD processes are shown in Figure 4-4.

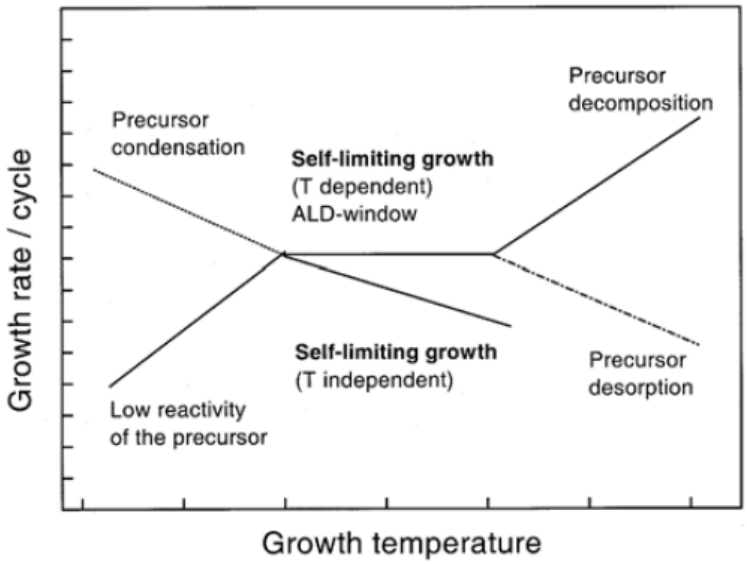


Figure 4-4: Factors limiting the self-limiting growth at various temperatures [12].

The successful industrial applications of ALD are still expanding. The current interest in ALD in the microelectronics industry stems from the unique characteristics that this method offers: high-quality, dense, and pinhole-free ultrathin films can be deposited on large substrates with excellent uniformity and conformality and control of the thickness and composition at the atomic level [4, 6, 14]. These characteristics are now especially needed for the processing of high-k dielectrics.

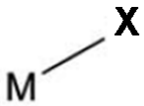
Section 4.2 Metal Precursors

Careful selection of the precursor is very important for a successful ALD process. There are several main requirements for a good ALD precursor. First, the vapor pressure of the precursor must be sufficient for easy delivery into the reactor. Thus, liquid or gaseous precursors are generally preferred over the solid ones. Second, the precursor must not undergo significant self-decomposition at deposition temperature in order to avoid CVD-type reactions. Third, the precursor must adsorb or react with the surface sites (in our case its reactivity towards the oxidizing agent, H_2O, must be sufficient). Furthermore, the precursor and its reaction by-products should not etch the surface or the growing film. In contrast to CVD, the Gibbs free energy ΔG for the reaction should be as negative as possible [4]. Other important considerations also include practical aspects, such as safety and economic requirements [4, 7].

As mentioned in Section 1.2, some leading candidates for alternative high-k dielectrics are the oxides of Al, Hf and Zr (in Nov. 2007, the first commercial high-k gate dielectric was introduced by Intel and is based on HfO_2). Since the selection of the precursor has an effect on the characteristics of the deposited film, this section emphasizes processes for Al_2O_3, HfO_2 and ZrO_2 that are deposited with different types of precursors.

4.2.1 Precursors for Al_2O_3

Aluminum halides such as $AlCl_4$, $AlBr_4$ and AlI_4 were the first ALD reactants and had been studied in the 1960s [15, 16]. Recently they have been extensively investigated for the deposition of Al_2O_3 as an alternative high-k dielectric [17, 18]. There are many benefits of using these halide precursors including the availability of volatile halides for many metals, high reactivity, small ligand size and thermal stability. The high reactivity makes halides very useful for the growth of a variety of materials including oxides, nitrides, sulfides, etc. The small size of the halide ligands can be regarded as advantageous because the steric hindrance effects related to ligands are then minimized [19, 20]. In addition, the aluminum halides usually have a higher thermal stability compared to metal organic precursors and offer a wider window for the growth temperature.



Halide

Figure 4-5: Molecular structure of metal halide.

Precursor		**T_{growth}**		
Metal	Oxygen	Range,	Preferred,	Ref.
Precursor	source	^0C	^0C	
$AlCl_3$	H_2O	400-600	500	[21-27]
	H_2O+	350-400	383	[21, 28]

	O_2	500	500	[21]
$AlMe_3$	H_2O	250-400	300	[25]

Table 4-1: List of common Al precursors used in ALD.

Despite the many favorable aspects of aluminum halides for ALD of Al_2O_3, there are several drawbacks. Since these halides are solids, sometimes vaporizing solid reactants is challenging. This is because particles are easily transported into the films resulting in particle contamination in the film. In addition, the products of the halide ligands after the growth can be another source of impurities. The gaseous reaction by-products with hydrogen-containing nonmetal reactants like H_2O, NH_3 and H_2S are HF, HCl, HBr, and HI. These gases are acidic, corrosive and can etch the film constituents or the reactor wall itself [29-31]. The gaseous reaction products may also re-adsorb on the surface after their formation and block reactive sites. This can cause undesired thickness gradients and leads to non-uniform films [32].

Alkyl ligands bound to metals were introduced as ALD reactants in the mid-1980s and today they are often used as reactants, especially for aluminum and zinc [33-39]. Since alkyls are very reactive organometallic compounds, a variety of materials including oxides, nitrides and sulfides can be grown from them. The alkyl ligands are also rather small which minimizes the steric hindrance effects. The growth rate in alkyl-reactant-based processes is often rather high [19, 20]. In the $AlMe_3$ (TMA, Trimethylaluminium) and H_2O process at 300 ℃, the growth rate is about 0.9 Å per cycle, which corresponds to about

30% of a monolayer of Al_2O_3 [40-45]. The reactions are truly self-terminating. Unlike the processes of aluminum halides with hydrogen-containing nonmetal reactants like H_2O, the gaseous byproducts are typically saturated hydrocarbons, which are generally inert and eliminate problems with readsorption or corrosion. The atomic concentrations of carbon and hydrogen residues in Al_2O_3 films were reported to be very low [41]. Although $AlMe_3$ decomposes above 300℃, which is lower than aluminum halides [46], this does not cause many problems. The main drawback to the use of alkyls is that the selection of elements available is rather limited. Overall, the $AlMe_3/H_2O$ system is a rather ideal ALD process.

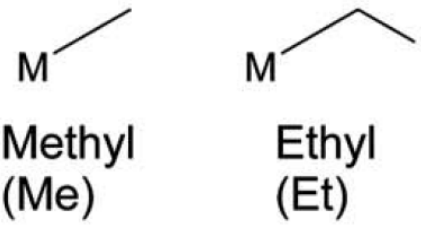


Figure 4-6: Molecular structures of metal alkyls.

4.2.2 Precursors for HfO_2

Because HfO_2 has been considered one of the most promising high-k dielectrics [2], the $HfCl_4/H_2O$ process, first introduced some 10 years ago [47], is one of the most thoroughly studied ALD processes. The $HfCl_4/H_2O$ process has many attractive features including: a wide growth temperature range - from 160 to 940 ℃ [48, 49], optimized film quality and unif ormity over a large surface area

[11, 50], very low carbon incorporation from the precursor into the films, and good electrical properties such as low leakage current [11, 50, 51].

Nevertheless, there are some major drawbacks of using $HfCl_4$. The chlorine content is found near the HfO_2 film/substrate (Ge or Si) interfacial region [11, 51, 52]. During post-deposition annealing, the chlorine causes etching of the substrate and is responsible for void defect formation [53]. It was shown that the amount of chlorine at the bottom interface is higher in Ge than in Si [11]. The formation of a thin oxide interfacial layer is also observed and the thickness has been reported to be about 0.3 nm in $HfO_2/GeO_x/Ge$ [11, 54] and 1.0-1.2 nm in $HfO_2/SiO_x/Si$ [51, 55].

Additional problems with $HfCl_4$ include formation of particles from the solid $HfCl_4$ precursor in the gas phase and poor nucleation of HfO_2 when deposited directly on clean Ge [11] and clean Si [50]. To overcome the problems related to the poor nucleation on clean Ge/Si, a thin chemically or thermally grown GeO_2/SiO_2, nitrided GeO_x/SiO_x, or interfacial layer of Al_2O_3 is used as a barrier layer before the deposition of HfO_2 [11, 50, 54]. However, this additional interfacial layer not only increases the EOT value, but also makes an ideal sharp interface between the HfO_2 and substrate impossible.

The use of HfI_4 instead of $HfCl_4$ has been suggested to obtain Cl-free films [56-58]. The HfI_4/H_2O process at 300 ℃ yields slightly lower halide content in the films than the $HfCl_4/H_2O$ process [58]. Using the iodide precursor with molecular oxygen requires higher temperatures (500-755 ℃) [56, 57] and this has to be taken into account for deposition on Ge since it has a lower melting point than Si.

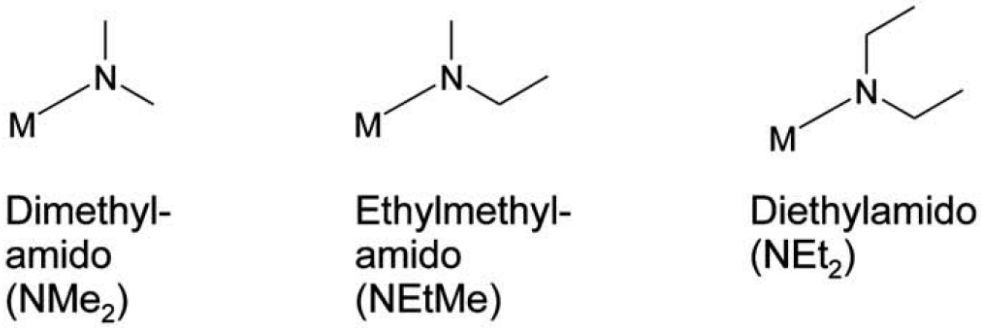


Figure 4-7: Molecular structures of metal alkyamides.

Volatile liquid hafnium alkylamides such as tetrakis(ethylmethylamido) hafnium ($Hf(NEtMe)_4$), tetrakis(dimethylamido) hafnium ($Hf(NMe_2)_4$) and tetrakis(diethylamido) hafnium ($Hf(NEt_2)_4$) are also used in the ALD of HfO_2 because they give excellent thickness uniformity and conformality [59] and good nucleation without significant interfacial layer formation [60].

The maximum suitable ALD growth temperature for the $Hf(NEtMe)_4/H_2O$ process is 350 ℃ [59] with water and is 275 ℃ [61] with ozone. Slight decomposition of the precursor that affects the growth rate occurs around 300℃ [62]. The thickness of the interfacial layer between HfO_2 and H-terminated Si has been reported to be exceptionally low, ~0.5 nm for the $Hf(NEtMe)_4/H_2O$ process compared to 1.0-1.2 nm in $HfCl_4/H_2O$ process and problems in nucleation at early stages of the growth were not detected [55, 60].

Precursor		**T_{growth}**		
Metal Precursor	Oxygen source	Range, ^0C	Preferred, ^0C	Ref.
$HfCl_4$	H_2O	160-940	300	[11, 51, 54]

	O_3	300	300	[63]
	O_2	250-650	550-650	[64]
	$Hf(NO_3)_4$	150-190	150-190	[65]
HfI_4	H_2O	225-500	300	[58]
	O_2	400-755	550-755	[56, 57]
$Hf(NEtMe)_4$	H_2O	100-350	250	[59, 62]
	O_3	100-275	250	[61, 66]
$Hf(NMe_2)_4$	H_2O	100-500	250	[59, 67, 68]
	O_3	160-420	200-300	[66]
$Hf(NEt_2)_4$	H_2O	100-500	<450	[59]
	O_2	250	250	[69]
	O_2	250	250	[69]

Table 4-2: List of common Hf precursors used in ALD.

As compared with $Hf(NEtMe)_4$, $Hf(NMe_2)_4$ precursors showed signs of thermal decomposition at lower temperatures (around 250 ℃ [67]), and the surface roughness increased more rapidly [70]. In addition, higher impurity levels were detected in films obtained from $Hf(NMe_2)_4$ and water [67] or ozone [66]. In the $Hf(NMe_2)_4/H_2O$ process, a relatively thick 1.5-2.0 nm interfacial silicon oxide layer was observed between Si and amorphous HfO_2 [67]. In another study, a SiN_x interfacial layer yielding a very promising EOT of 1.8 nm with low leakage current density was reported [71].

Another hafnium alkylamide precursor, $Hf(NEt_2)_4$, has been used occasionally, together with either water [59, 72], oxygen [69], or an oxygen

plasma [69, 73-75] as the oxygen source. The growth of interfacial Hf-silicate layers can be significant, especially in the case of an oxygen plasma [69, 74].

4.2.3 Precursors for ZrO_2

In the first ALD study of ZrO_2 with the $ZrCl_4/H_2O$ process, the applied growth temperature was 500℃ and it gave a growth r ate of 0.53 Å/cycle [76]. Since then, a wide temperature range of 180 to 600 ℃ has been used in the same process [77-82]. The optimized temperature is 300 ℃, showing well saturated growth with a growth rate of 0.5-1.0 Å/cycle.

Similarly, as in the case of the $HfCl_4/H_2O$ process, some obvious drawbacks of $ZrCl_4/H_2O$ are identified, including significant chlorine impurity levels at 300℃ [80], corrosive by-product HCl [83] , and particle contamination coming from the fine solid precursor $ZrCl_4$. Annealing at high (900-1050 ℃) temperatures could reduce the chlorine level [84], but it also caused crystallization even in very thin layers [85]. The chlorine residues tend to accumulate at the interface [86].

Another Zr halide, ZrI has been used as an alternative of $ZrCl_4$ [87-90] to reduce the halide content with post deposition annealing because of its weaker metal-halogen bond [91]. Unfortunately, ZrI_4 does not improve the problem significantly. In addition, it was observed that desorption of iodine caused problems for saturation of growth at 300 ℃ [88].

In addition to the problems mentioned above, the use of Zr halides as precursors has another challenge, island-type growth [78, 92]. A common solution to overcome this is to use a thin thermal or chemical oxide or a nitrided oxide layer as a starting layer. However, these introduce a lower k interfacial layer and increase EOT. For these reasons, an alternative precursor for the ALD of ZrO_2 is needed.

Precursor		**T_{growth}**		
Metal Precursor	Oxygen source	Range, ^0C	Preferred, ^0C	Ref.
$ZrCl_4$	H_2O	180-600	300	[76, 80]
	H_2O+ O_2	180-600 500	300 500	[80, 81] [93, 94]
ZrI_4	H_2O+	230-500	275-325	[87, 89, 90]
$Zr(NEtMe)_4$	H_2O	<250	<250	[59]
	O_2	110-250	200-250	[95]
$Zr(NMe_2)_4$	H_2O	<300	<300	[59]
$Zr(NEt_2)_4$	H_2O	<350	<350	[59]
	O_2	250	250	[96]

Table 4-3: List of common Zr precursors used in ALD.

Using Zr alkylamides, such as $Zr(NMe_2)_4$, $Zr(NEtMe)_4$, and $Zr(NEt_2)_4$ has many benefits. Because they are liquid at the evaporation temperature, the

particle contamination problem is eliminated [59]. The alkylamides are reactive towards water and give reasonably low impurity levels [59]. However with Zr alkylamides, higher carbon contents have been reported when oxygen or oxygen plasmas were used as the oxygen source [95-98]. The main issue with the use of alkylamides is their thermal stability. The decomposition of these precursors limits the maximum growth temperature to 250℃. If smooth films are desired, the growth temperature must be low [70].

The reported ALD processes for ZrO_2 are listed in Table 4-3, where the alternative processes, as expected, are very similar to the previously described alternative HfO_2 processes (Table 4-2).

Section 4.3 Oxygen Sources

In the ALD of metal oxide thin films, there are many different oxygen sources including H_2O, O_2, O_3, H_2O_2, oxygen plasmas, and metal alkoxides [4, 10]. Among them, water is the most common oxygen source. The order of the oxidation power of these commonly used oxygen sources from high to low is oxygen plasma > ozone > hydrogen peroxide > water.

In practice, the selection of oxygen precursor is more complicated. Generally speaking, a strong oxidizer, like an oxygen plasma or ozone, can produce denser films with lower impurity levels and enhanced electrical properties [63, 99]. However, the strong oxidizer often causes the formation of a fairly thick interfacial layer because it also oxidizes the substrate [99-101]. The

additional growth of low permittivity interfacial layers makes it difficult to achieve low EOT values and excludes strong oxidizer processing as a good solution for high-k gate dielectric fabrication.

On the other hand, oxidizers like water and H_2O_2 rely on hydroxyl groups on the starting surface and high reactivity of the chemisorbed metal precursors. Otherwise the initial nucleation during deposition may be inhibited resulting in poor electrical properties of the films [78, 102].

In the metal-halide based process, replacing H_2O with O_3 decreases the Cl-content in the bulk of the film and improved most of the dielectric properties, including fixed charge, interface trap densities, and the leakage current characteristics [63]. However, the higher oxygen content in the ozone-processed films resulted in a thicker interfacial layer and thus increased EOT after rapid thermal annealing (RTA) at 750 ℃.

In the metal-alkylamide based process, ozone as the oxygen source instead of water has gained considerable interest to grow HfO_2 [55, 61, 101, 103, 104]. For example, using ozone instead of water with a $Hf(NMe_2)_4$ precursor at a relatively high growth temperature of 300 ℃ reduced the impurity contents and the films showed a more amorphous structure leading to better leakage current characteristics [105, 106]. However, in some studies the use of ozone did not significantly reduce impurities nor enhance electrical properties as compared to the use of water, but they did increase the thickness of the interfacial oxide layer [55, 103].

Section 4.4 ALD System

In our work, ALD of high-k dielectrics were performed in a home-made ALD system coupled to a commercial XPS system. Together with the metallization chambers which have the ability to deposit various metals as the metal gate, this integrated system makes in-situ study of advanced MOS devices possible.

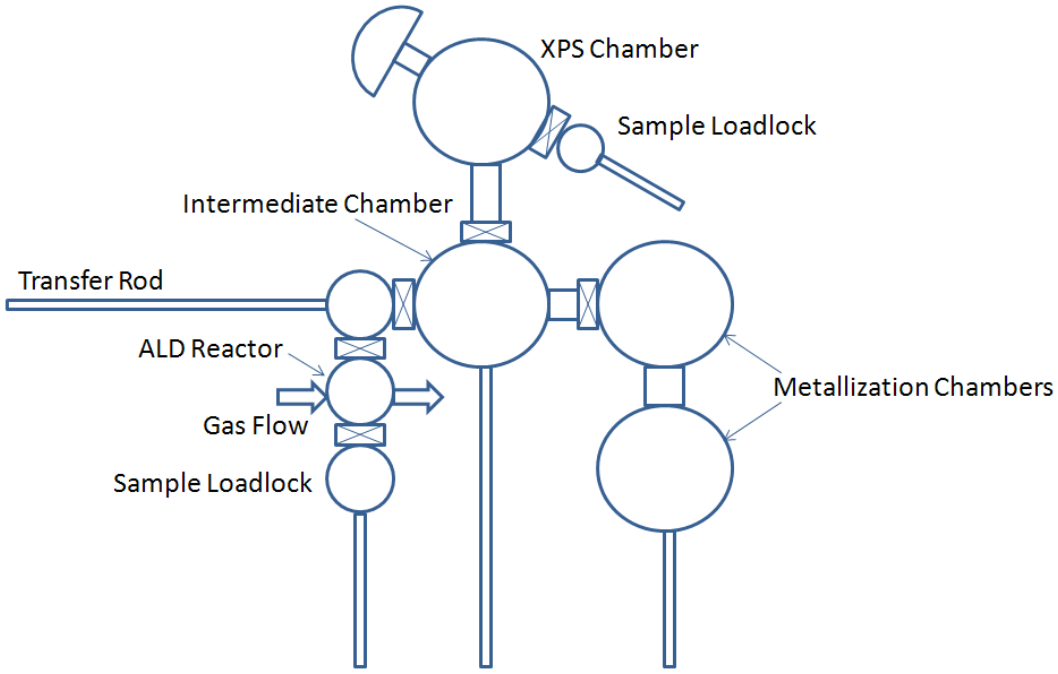


Figure 4-8: The integrated XPS system with ALD and metallization chambers.

The ALD system consists of a sample introduction chamber, a reactor with a sample heater and gas lines. A Ge wafer of 1" diameter or smaller is mounted onto the sample holder which is compatible with the sample holder of the XPS system and is then loaded into the system from the quick loadlock. The gate valve between the reactor and the loadlock makes it possible to load a sample without venting the reactor. The transfer rod is used to send the sample into the reactor and mount it onto a sample heating platform where a thermocouple is

mounted to monitor the temperature of the sample. The whole system including the sample is first preheated to 100-110 ℃ to desorb water and then pumped down to 10^{-6}-10^{-7} Torr for an hour before the deposition starts. Several pneumatic valves are installed to control the flow of gases and produce the alternative pulses of precursors in ALD. The flow rate of purging N_2 is set to 100 cc per minute by a mass flow controller. A scroll pump is used to avoid the back streaming of oil vapor from a mechanical pump. Together with an adjustable throttle valve, the pressure of the reactor with N_2 purging can be controlled to a constant between 0.1-1.0 Torr. During deposition, the reactor and all gas lines are heated with heating tapes and are maintained in a hot wall condition at fixed elevated temperature in order to prevent the condensation of chemicals on the chamber walls.

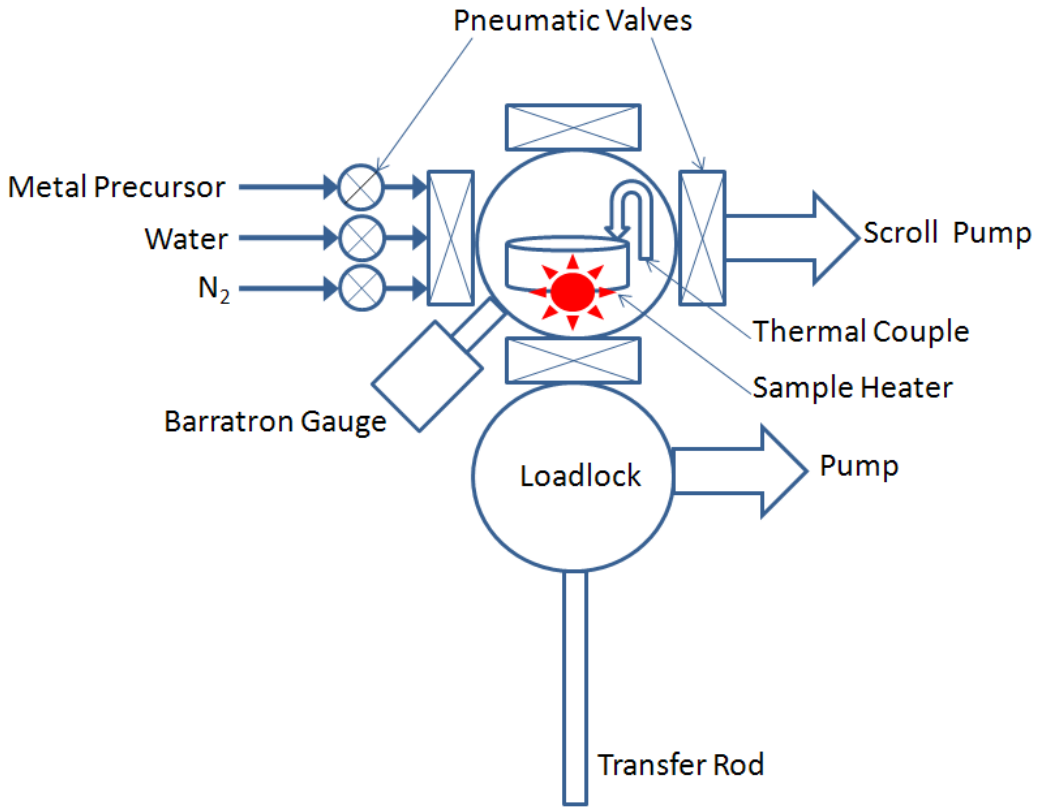


Figure 4-9: The schematic drawing of the ALD system.

The whole ALD system is monitored and controlled with a LabView program running on a PC with a USB 12-bit DAQ board. With the Baratron pressure gauge, and the thermocouples attached to the sample, the reactor, gas lines and precursor bottles, the pressure and temperatures are logged at all times. Using the LabView program, one can also easily configure temperature set points for each part of the system and design customized ALD growth parameters including gas pulse sequence, duration and number of cycles.

Section 4.5 Experimental Results of ALD Film Growths

In this section, experimental results of ALD growth of Al_2O_3 and HfO_2 on various substrates are presented. With the help of RBS, the deposited film thicknesses were determined as well as the growth rates per ALD cycle.

4.5.1 ALD of Al_2O_3

In this work, Al_2O_3 films are deposited using the ALD system mentioned above with TMA and water at 70-95 ℃. In an RBS ran dom spectrum, since Si and Ge are heavier than Al, the Al signal will usually be overwhelmed by the substrate background signal. Figure 4-10 shows the random incident RBS spectrum of Al_2O_3 films of the same thickness on Si and Ge substrates. On the Ge substrate, the Al peak is buried in the Ge background and this makes it difficult to precisely determine the thickness of Al_2O_3 films. In the case of Al_2O_3/Si, the Al peak in the RBS spectrum is near the edge of Si background. As long as the Al_2O_3 film is not too thin, one still can fit the spectra and extract the film thickness. A simulation using SIMNRA gives the atomic areal density 1.70×10^{17} atoms/cm^2 for the Al_2O_3 layer corresponding to a physical film thickness of 156 Å. In this specific deposition, the number of ALD cycles is 200 and this gives a growth rate of about 0.78 Å/cycle.

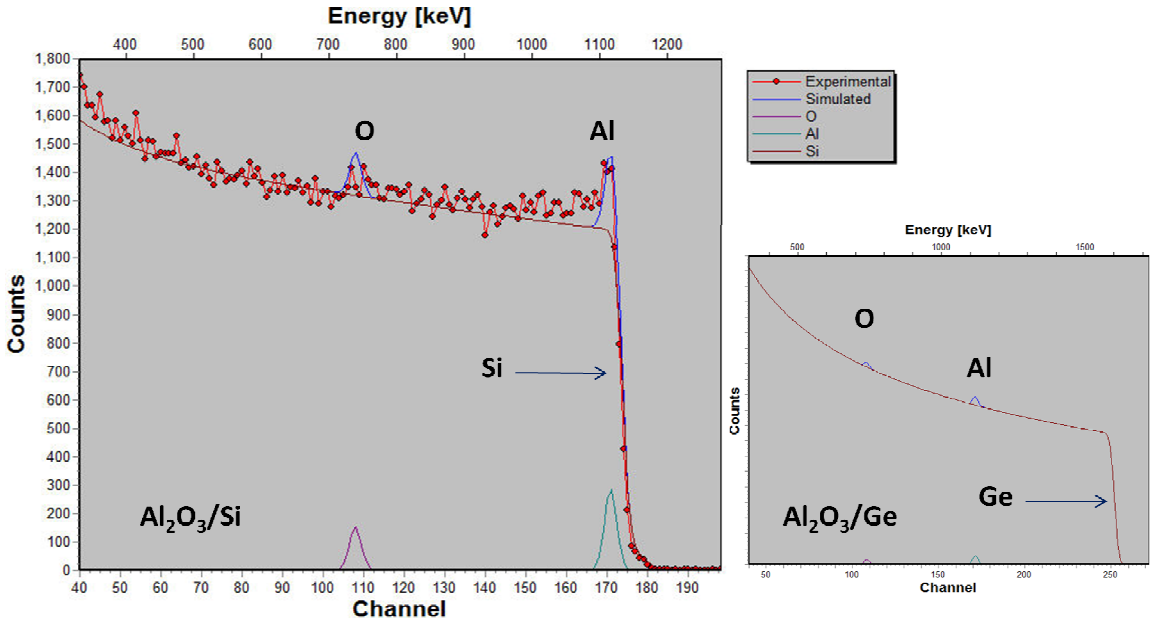


Figure 4-10: RBS random scattering spectrum of Al_2O_3 of the same thickness on Si (left) and Ge (right).

A better way to determine the physical film thickness is to utilize RBS channeling to suppress the background signal from the heavy substrate atoms. In Figure 4-11, a channeling RBS spectrum of Al_2O_3 on ITO (indium tin oxide or tin-doped indium oxide)/glass substrate is shown. Under the channeling condition, the Si signal from glass has been suppressed and this increases sensitivities of light elements like Al and O. Note that the O signal is not like a single peak in the previous Al_2O_3/Si spectrum. This is because O signals are not only from the Al_2O_3 layer on the top but also from ITO layer.

Since organic light emitting devices (OLEDs) [107] are extremely sensitive to moisture and oxygen [108], a perimeter seal inside the device is required as a protective barrier. UV-cured epoxy, the most commonly used method, is inadequate for top-emitter OLEDs because the emitted light has to pass through

the cover glass and the opaque desiccant. PVD and CVD based methods have been studied for the top-emitter encapsulation [109, 110]. Recently it has been shown that ALD can be used to deposit a thin Al_2O_3 film as a dense, light-weight and transparent encapsulating layer which can withstand accelerated testing at 85℃ and high relative humidity (85%) for more than 1000 hours [111].

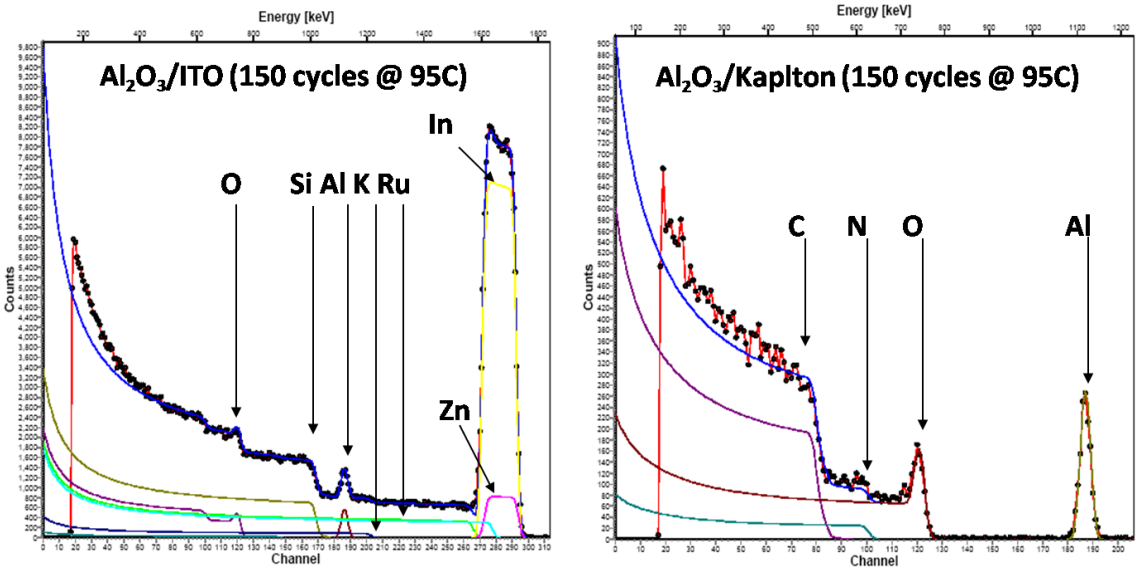


Figure 4-11: RBS spectra of Al_2O_3 on ITO (left) and Kapton (right).

Al_2O_3 has been deposited on ITO and DuPont Kapton E polyimide films. ITO is a mixture of indium oxide (In_2O_3) and tin oxide (SnO_2). Because of its electrical conductivity and optical transparency, ITO is commonly used in LCD/LED/plasma displays, solar cells and OLEDs. DuPont Kapton E polyimide film is a thermally stable dielectric film in a wide range of temperatures and this also makes it a popular choice for the base plate of displays and OLEDs. In Figure 4-12, it shows the growth rate is about 0.81 Å per ALD cycle.

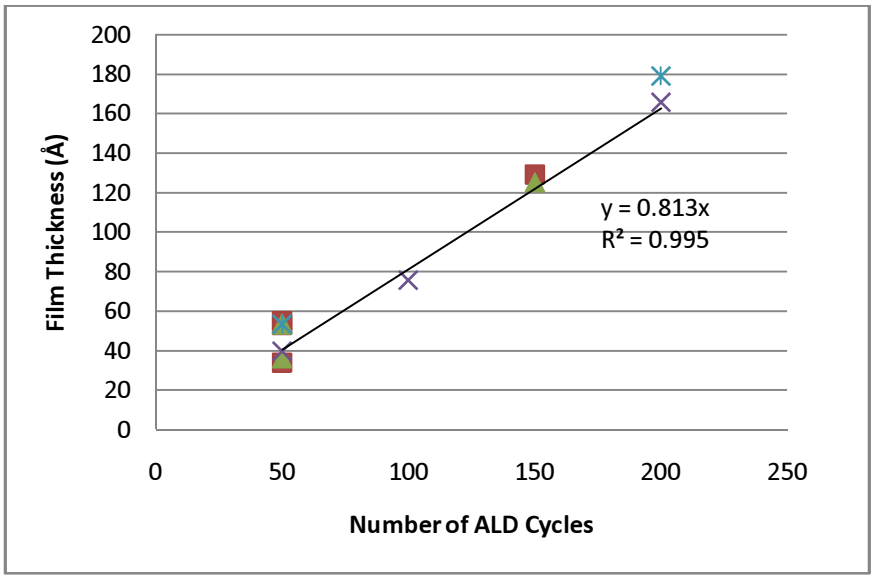


Figure 4-12: Film thickness of Al_2O_3 vs. number of ALD cycles.

4.5.2 ALD of HfO_2

HfO_2 films were deposited on various type of substrates with $Hf(NEtMe)_4$ and water in the 150-175 ℃ range. In Figure 4-13, a random incident RBS spectrum of HfO_2/GaAs is shown. Since Hf is heavy, the Hf peak is well separated from the substrate signals of Ga and As. If determination of HfO_x composition is desired, a channeling RBS study can be done to suppress the background and make the O peak more sensitive. In this spectrum, the simulation with atomic areal density makes the best fit with the experimental data and this suggests the physical film thickness is about 101 Å. There are 120 ALD cycles and thus the growth rate is 0.84 Å/cycle. Repeating ALD of HfO_2 with a different number of cycles at the same growth temperature and the same cycle settings gives a growth rate of about 0.83 Å/cycle shown in Figure 4-14.

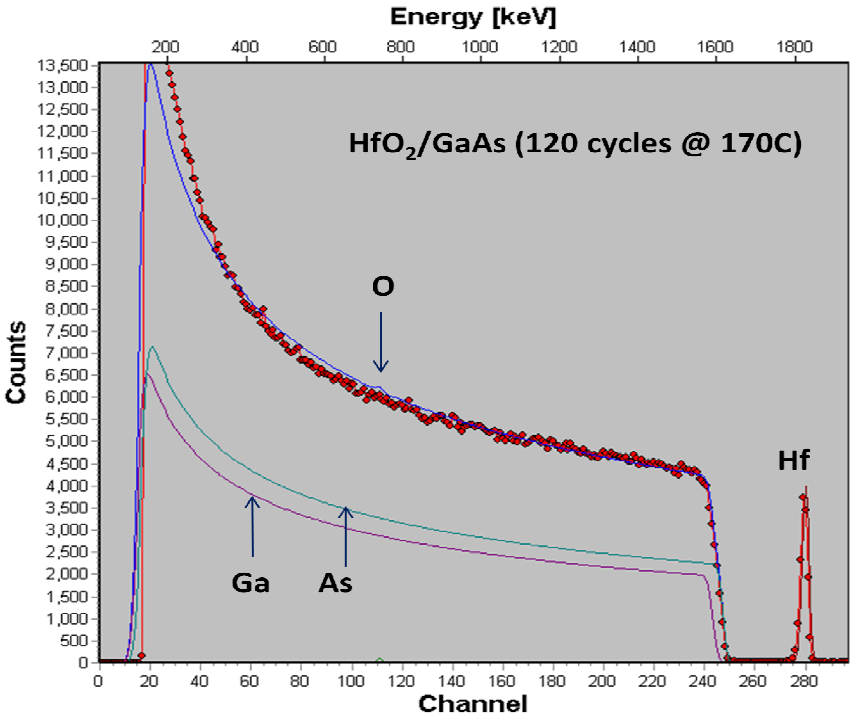


Figure 4-13: Random scattering RBS spectrum of HfO_2/GaAs.

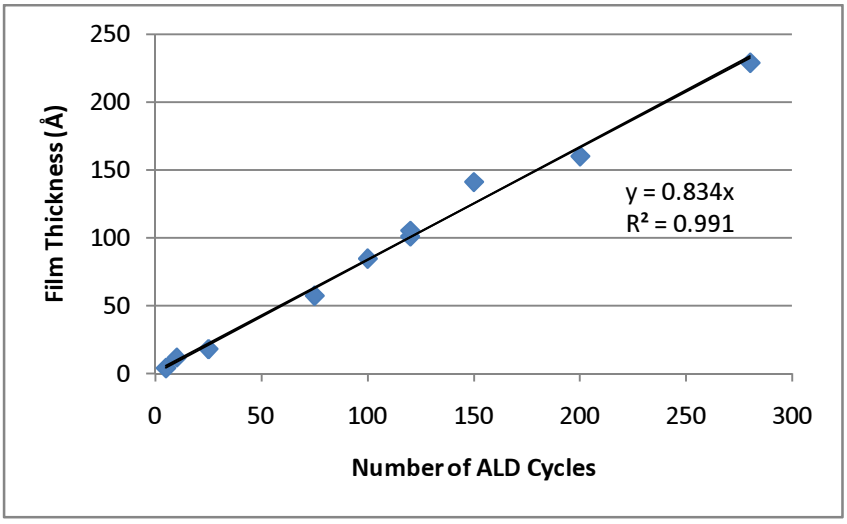


Figure 4-14: Film thickness of HfO_2 vs. number of ALD cycles.

ALD of HfO_2 on clean Ge(100) and Si(100) were also performed. In Figure 4-15, random scattering RBS spectra show that 35 ALD cycles deposited 29.9 Å of HfO_2 on Ge (~0.85 Å/cycle) and 30 ALD cycles deposited 23.8 Å of HfO_2 on

Ge (~0.79 Å/cycle). The overall growth rate is 0.86 Å/cycle and 0.81 Å/cycle for HfO_2 ALD on Ge and Si respectively (Figure 4-16).

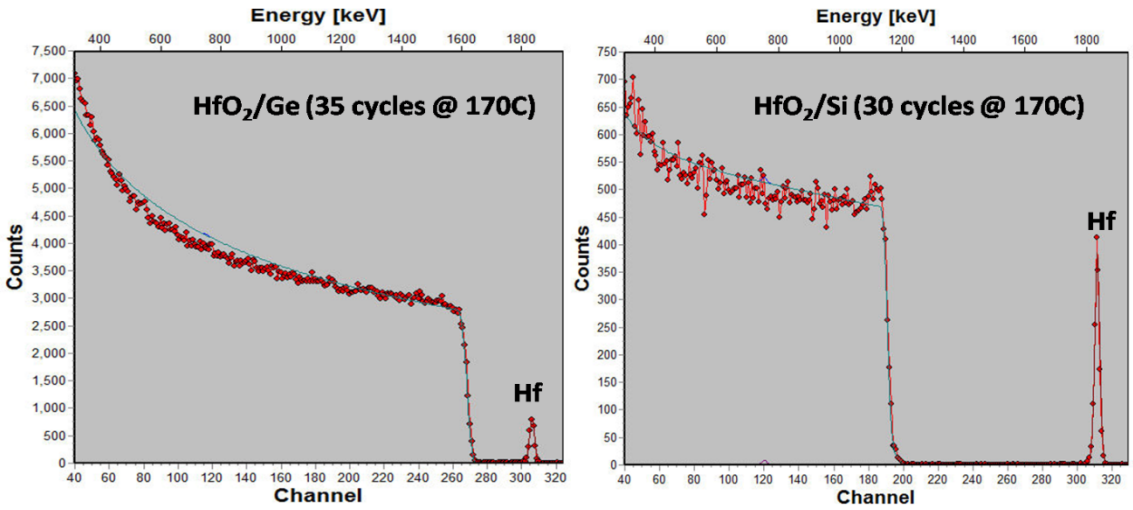


Figure 4-15: Random scattering RBS spectrum of HfO_2/Ge (left) and HfO_2/Si (right).

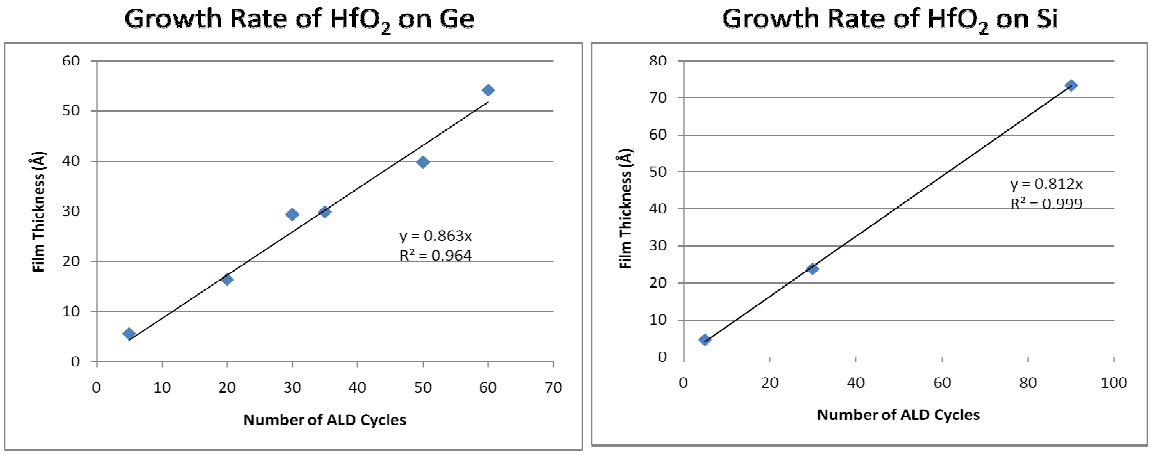


Figure 4-16: Film thickness of HfO_2 on Ge (left) and on Si (right) vs. number of ALD cycles.

Section 4.6 Reference

1. T. Suntola and J. Antson, *A method for producing compound thin films*. 1977: US Patent 4,058,430.
2. I.T.R.f. Semiconductors. Available from: http://www.itrs.net/.
3. A. Hand, *Industry begins to embrace ALD.* Semiconductor International, 2003. **26**(5): p. 46-51.
4. M. Ritala and M. Leskelä, in *Handbook of Thin Film Materials*, H.S. Nalwa, Editor. 2002, Academic Press: New York. p. 103-159.
5. L. Niinisto, M. Ritala, and M. Leskela, *Synthesis of oxide thin films and overlayers by atomic layer epitaxy for advanced applications.* Materials Science and Engineering B-Solid State Materials for Advanced Technology, 1996. **41**(1): p. 23-29.
6. M. Leskela and M. Ritala, *Atomic layer deposition chemistry: Recent developments and future challenges.* Angewandte Chemie-International Edition, 2003. **42**(45): p. 5548-5554.
7. L. Niinisto, J. Paivasaari, J. Niinisto, et al., *Advanced electronic and optoelectronic materials by Atomic Layer Deposition: An overview with special emphasis on recent progress in processing of high-k dielectrics and other oxide materials.* Physica Status Solidi A-Applied Research, 2004. **201**(7): p. 1443-1452.
8. M. Leskela and M. Ritala, *Atomic layer deposition (ALD): from precursors to thin film structures.* Thin Solid Films, 2002. **409**(1): p. 138-146.
9. L. Niinisto, *Atomic layer epitaxy.* Current Opinion in Solid State and Materials Science, 1998. **3**(2): p. 147-152.
10. R.L. Puurunen, *Surface chemistry of atomic layer deposition: A case study for the trimethylaluminum/water process.* Journal of Applied Physics, 2005. **97**(12): p. -.
11. A. Delabie, R.L. Puurunen, B. Brijs, et al., *Atomic layer deposition of hafnium oxide on germanium substrates.* Journal of Applied Physics, 2005. **97**(6): p. -.
12. J. Niinistö, *Atomic layer deposition of high-k dielectrics from novel cyclopentadienyl-type precursors*, in *Department of Chemical Technology*. 2006, Helsinki University of Technology: Espoo, Finland.
13. T. Suntola, *Surface chemistry of materials deposition at atomic layer level.* Applied Surface Science, 1996. **101**: p. 391-398.
14. M. Ritala and M. Leskela, *Atomic layer epitaxy - a valuable tool for nanotechnology?* Nanotechnology, 1999. **10**(1): p. 19-24.
15. T.S. Suntola, A.J. Pakkala, and S.G. Lindfors, *Method for performing growth of compound thin films*. 1983: U.S. Patent No. 4,413,022.
16. M. Pessa, R. Mäkelä, and T. Suntola, *Characterization of surface exchange reactions used to grow compound films.* Applied Physics Letters, 1981. **38**(3): p. 131-132.
17. G.D. Wilk, R.M. Wallace, and J.M. Anthony, *High-kappa gate dielectrics: Current status and materials properties considerations.* Journal of Applied Physics, 2001. **89**(10): p. 5243-5275.
18. R.M. Wallace and G.D. Wilk, *High-kappa dielectric materials for microelectronics.* Critical Reviews in Solid State and Materials Sciences, 2003. **28**(4): p. 231-285.
19. M. Ylilammi, *Monolayer thickness in atomic layer deposition.* Thin Solid Films, 1996. **279**(1-2): p. 124-130.

20. R.L. Puurunen, *Growth per cycle in atomic layer deposition: A theoretical model.* Chemical Vapor Deposition, 2003. **9**(5): p. 249-257.
21. L. Hiltunen, H. Kattelus, M. Leskelä, et al., *Growth and characterization of aluminium oxide thin films deposited from various source materials by atomic layer epitaxy and chemical vapor deposition processes.* Materials Chemistry and Physics 1991. **28**(4): p. 379-388.
22. M. Nieminen, L. Niinisto, and R. Lappalainen, *Determination of P/Al Ratio in Phosphorus-Doped Aluminum-Oxide Thin-Films by Xrf, Rbs and Ftir.* Mikrochimica Acta, 1995. **119**(1-2): p. 13-22.
23. M. Ritala, H. Saloniemi, M. Leskela, et al., *Studies on the morphology of Al2O3 thin films grown by atomic layer epitaxy.* Thin Solid Films, 1996. **286**(1-2): p. 54-58.
24. D. Riihela, M. Ritala, R. Matero, et al., *Introducing atomic layer epitaxy for the deposition of optical thin films.* Thin Solid Films, 1996. **289**(1-2): p. 250-255.
25. S.J. Yun, K.H. Lee, J. Skarp, et al., *Dependence of atomic layer-deposited Al2O3 films characteristics on growth temperature and Al precursors of Al(CH3)(3) and AlCl3.* Journal of Vacuum Science and Technology A, 1997. **15**(6): p. 2993-2997.
26. M. Nieminen and L. Niinisto, *Determination of aluminium in AlCl3 and Al2O3 modified silica catalyst supports.* Fresenius Journal of Analytical Chemistry, 1999. **364**(3): p. 224-227.
27. K. Kukli, M. Ritala, and M. Leskela, *Development of dielectric properties of niobium oxide, tantalum oxide, and aluminum oxide based nanolayered materials.* Journal of the Electrochemical Society, 2001. **148**(2): p. F35-F41.
28. M. Tiitta, E. Nykanen, P. Soininen, et al., *Preparation and characterization of phosphorus-doped aluminum oxide thin films.* Materials Research Bulletin, 1998. **33**(9): p. 1315-1323.
29. K.E. Elers, M. Ritala, M. Leskela, et al., *Nbcl(S) as a precursor in atomic layer epitaxy.* Applied Surface Science, 1994. **82-3**: p. 468-474.
30. J. Aarik, A. Aidla, K. Kukli, et al., *Deposition and etching of tantalum oxide-films in atomic layer epitaxy process.* Journal of Crystal Growth, 1994. **144**(1-2): p. 116-119.
31. K. Kukli, J. Aarik, A. Aidla, et al., *Atomic layer deposition of tantalum oxide thin films from iodide precursor.* Chemistry of Materials, 2001. **13**(1): p. 122-128.
32. H. Siimon and J. Aarik, *Thickness profiles of thin films caused by secondary reactions in flow-type atomic layer deposition reactors.* Journal of Physics D-Applied Physics, 1997. **30**(12): p. 1725-1728.
33. M.A. Tischler and S.M. Bedair, *Growth and characterization of compound semiconductors by atomic layer epitaxy.* Journal of Crystal Growth, 1986. **77**(1-3): p. 89-94.
34. J. Nishizawa, H. Abe, and T. Kurabayashi, *Molecular layer epitaxy.* Journal of the Electrochemical Society, 1985. **132**(5): p. 1197.
35. G.S. Higashi and L.J. Rothberg, *Surface photochemical phenomena in laser chemical vapor deposition* Journal of Vacuum Science and Technology B, 1985. **3**(5): p. 1460-1463.
36. M. Ozeki, K. Mochizuki, N. Ohtsuka, et al., *Kinetic processes in atomic-layer epitaxy of GaAs and AlAs using a pulsed vapor-phase method* Journal of Vacuum Science and Technology B, 1987. **5**(4): p. 1184-1186.
37. S.M. Bedair, M.A. Tischler, T. Katsuyama, et al., *Atomic layer epitaxy of III-V binary compounds.* Applied Physics Letters 1985. **47**(1): p. 51-53

38. A. Hunter and A.H. Kitai, *A novel atmospheric pressure technique for the deposition of ZnS by atomic layer epitaxy using dimethylzinc.* Journal of Crystal Growth, 1988. **91**(1-2): p. 111-118.
39. A. Doi, Y. Aoyagi, and S. Namba, *Stepwise monolayer growth of GaAs by switched laser metalorganic vapor phase epitaxy.* Applied Physics Letters 1986. **49**(13): p. 785-787
40. M. Putkonen, M. Nieminen, and L. Niinisto, *Magnesium aluminate thin films by atomic layer deposition from organometallic precursors and water.* Thin Solid Films, 2004. **466**(1-2): p. 103-107.
41. R. Matero, A. Rahtu, M. Ritala, et al., *Effect of water dose on the atomic layer deposition rate of oxide thin films.* Thin Solid Films, 2000. **368**(1): p. 1-7.
42. O. Sneh, R.B. Clark-Phelps, A.R. Londergan, et al., *Thin film atomic layer deposition equipment for semiconductor processing.* Thin Solid Films, 2002. **402**(1-2): p. 248-261.
43. M.D. Groner, J.W. Elam, F.H. Fabreguette, et al., *Electrical characterization of thin Al2O3 films grown by atomic layer deposition on silicon and various metal substrates.* Thin Solid Films, 2002. **413**(1-2): p. 186-197.
44. J.M. Jensen, A.B. Oelkers, R. Toivola, et al., *X-ray reflectivity characterization of ZnO/Al2O3 multilayers prepared by atomic layer deposition.* Chemistry of Materials, 2002. **14**(5): p. 2276-2282.
45. R.L. Puurunen, W. Vandervorst, W.F.A. Besling, et al., *Island growth in the atomic layer deposition of zirconium oxide and aluminum oxide on hydrogen-terminated silicon: Growth mode modeling and transmission electron microscopy.* Journal of Applied Physics, 2004. **96**(9): p. 4878-4889.
46. R.L. Puurunen, M. Lindblad, A. Root, et al., *Successive reactions of gaseous trimethylaluminium and ammonia on porous alumina.* Physical Chemistry Chemical Physics, 2001. **3**(6): p. 1093-1102.
47. M. Ritala, M. Leskela, L. Niinisto, et al., *Development of crystallinity and morphology in hafnium dioxide thin-films grown by atomic layer epitaxy.* Thin Solid Films, 1994. **250**(1-2): p. 72-80.
48. J. Aarik, A. Aidla, A.A. Kiisler, et al., *Influence of substrate temperature on atomic layer growth and properties of HfO2 thin films.* Thin Solid Films, 1999. **340**(1-2): p. 110-116.
49. J. Aarik, A. Aidla, H. Mandar, et al., *Texture development in nanocrystalline hafnium dioxide thin films grown by atomic layer deposition.* Journal of Crystal Growth, 2000. **220**(1-2): p. 105-113.
50. E.P. Gusev, C. Cabral, M. Copel, et al., *Ultrathin HfO2 films grown on silicon by atomic layer deposition for advanced gate dielectrics applications.* Microelectronic Engineering, 2003. **69**(2-4): p. 145-151.
51. V. Kaushik, M. Claes, A. Delabie, et al., *Observation and characterization of defects in HfO2 high-K gate dielectric layers.* Microelectronics Reliability, 2005. **45**(5-6): p. 798-801.
52. J.J. Ganem, I. Trimaille, I.C. Vickridge, et al., *Study of thin hafnium oxides deposited by atomic layer deposition.* Nuclear Instruments & Methods in Physics Research Section B-Beam Interactions with Materials and Atoms, 2004. **219-20**: p. 856-861.
53. P.S. Lysaght, B. Foran, G. Bersuker, et al., *Physicochemical properties of HfO2 in response to rapid thermal anneal.* Applied Physics Letters, 2003. **82**(8): p. 1266-1268.

54. M. Caymax, S. Van Elshocht, M. Houssa, et al., *HfO2 as gate dielectric on Ge: Interfaces and deposition techniques.* Materials Science and Engineering B-Solid State Materials for Advanced Technology, 2006. **135**(3): p. 256-260.
55. D.H. Triyoso, R.I. Hegde, B.E. White, et al., *Physical and electrical characteristics of atomic-layer-deposited hafnium dioxide formed using hafnium tetrachloride and tetrakis(ethylmethylaminohafnium).* Journal of Applied Physics, 2005. **97**(12): p. -.
56. J. Aarik, J. Sundqvist, A. Aidla, et al., *Hafnium tetraiodide and oxygen as precursors for atomic layer deposition of hafnium oxide thin films.* Thin Solid Films, 2002. **418**(2): p. 69-72.
57. K. Kukli, M. Ritala, J. Sundqvist, et al., *Properties of hafnium oxide films grown by atomic layer deposition from hafnium tetraiodide and oxygen.* Journal of Applied Physics, 2002. **92**(10): p. 5698-5703.
58. K. Kukli, M. Ritala, T. Sajavaara, et al., *Comparison of hafnium oxide films grown by atomic layer deposition from iodide and chloride precursors.* Thin Solid Films, 2002. **416**(1-2): p. 72-79.
59. D.M. Hausmann, E. Kim, J. Becker, et al., *Atomic layer deposition of hafnium and zirconium oxides using metal amide precursors.* Chemistry of Materials, 2002. **14**(10): p. 4350-4358.
60. K. Kukli, M. Ritala, J. Lu, et al., *Properties of HfO2 thin films grown by ALD from hafnium tetrakis(ethylmethylamide) and water.* Journal of the Electrochemical Society, 2004. **151**(8): p. F189-F193.
61. S. Kamiyama, T. Miura, and Y. Nara, *Electrical properties of ultrathin HfO2 films for replacement metal gate transistors, fabricated by atomic layer deposition using Hf(N(CH3)(C2H5))(4) and O-3.* Applied Physics Letters, 2005. **87**(13): p. -.
62. K. Kukli, M. Ritala, T. Sajavaara, et al., *Atomic layer deposition of hafnium dioxide films from hafnium tetrakis(ethylmethylamide) and water.* Chemical Vapor Deposition, 2002. **8**(5): p. 199-204.
63. H.B. Park, M.J. Cho, J. Park, et al., *Comparison of HfO2 films grown by atomic layer deposition using HfCl4 and H2O or O-3 as the oxidant.* Journal of Applied Physics, 2003. **94**(5): p. 3641-3647.
64. N. Takahashi, S. Nonobe, and T. Nakamura, *Growth of HfO2 films using an alternate reaction of HfCl4 and O-2 under atmospheric pressure.* Journal of Solid State Chemistry, 2004. **177**(11): p. 3944-3948.
65. J.F. Conley, Y. Ono, D.J. Tweet, et al., *Pulsed deposition of metal-oxide thin films using dual metal precursors.* Applied Physics Letters, 2004. **84**(3): p. 398-400.
66. S.I. Lee, J.S. Owyang, Y. Senzaki, et al., *High-k gate dielectric applications using ALD Hf-based oxides.* Solid State Technology, 2003. **46**(1): p. 45.
67. K. Kukli, T. Pilvi, M. Ritala, et al., *Atomic layer deposition of hafnium dioxide thin films from hafnium tetrakis(dimethylamide) and water.* Thin Solid Films, 2005. **491**(1-2): p. 328-338.
68. R.G. Gordon, J. Becker, D. Hausmann, et al., *Vapor deposition of metal oxides and silicates: Possible gate insulators for future microelectronics.* Chemistry of Materials, 2001. **13**(8): p. 2463-2464.
69. S. Choi, J. Koo, H. Jeon, et al., *Plasma-enhanced atomic-layer deposition of a HfO2 gate dielectric.* Journal of the Korean Physical Society, 2004. **44**(1): p. 35-38.

70. D.M. Hausmann and R.G. Gordon, *Surface morphology and crystallinity control in the atomic layer deposition (ALD) of hafnium and zirconium oxide thin films.* Journal of Crystal Growth, 2003. **249**(1-2): p. 251-261.
71. M. Cho, H.B. Park, J. Park, et al., *High-k properties of atomic-layer-deposited HfO2 films using a nitrogen-containing Hf[N(CH3)(2)](4) precursor and H2O oxidant.* Applied Physics Letters, 2003. **83**(26): p. 5503-5505.
72. A. Deshpande, R. Inman, G. Jursich, et al., *Atomic layer deposition and characterization of hafnium oxide grown on silicon from tetrakis(diethylamino)hafnium and water vapor.* Journal of Vacuum Science and Technology A, 2004. **22**(5): p. 2035-2040.
73. J. Kim, S. Kim, H. Jeon, et al., *Characteristics of HfO2 thin films grown by plasma atomic layer deposition.* Applied Physics Letters, 2005. **87**(5): p. -.
74. Y. Won, S. Park, J. Koo, et al., *Initial reaction of hafnium oxide deposited by remote plasma atomic layer deposition method.* Applied Physics Letters, 2005. **87**(26): p. -.
75. J. Kim, S. Kim, H. Kang, et al., *Composition, structure, and electrical characteristics of HfO2 gate dielectrics grown using the remote- and direct-plasma atomic layer deposition methods.* Journal of Applied Physics, 2005. **98**(9): p. -.
76. M. Ritala and M. Leskela, *Zirconium dioxide thin-films deposited by ALE using zirconium tetrachloride as precursor.* Applied Surface Science, 1994. **75**: p. 333-340.
77. V. Sammelselg, E. Rauhala, K. Arstila, et al., *Study of thin oxide films by electron, ion and synchrotron radiation beams.* Mikrochimica Acta, 2002. **139**(1-4): p. 165-169.
78. M. Copel, M. Gribelyuk, and E. Gusev, *Structure and stability of ultrathin zirconium oxide layers on Si(001).* Applied Physics Letters, 2000. **76**(4): p. 436-438.
79. C.M. Perkins, B.B. Triplett, P.C. McIntyre, et al., *Electrical and materials properties of ZrO2 gate dielectrics grown by atomic layer chemical vapor deposition.* Applied Physics Letters, 2001. **78**(16): p. 2357-2359.
80. K. Kukli, M. Ritala, J. Aarik, et al., *Influence of growth temperature on properties of zirconium dioxide films grown by atomic layer deposition.* Journal of Applied Physics, 2002. **92**(4): p. 1833-1840.
81. J. Aarik, A. Aidla, H. Mandar, et al., *Growth kinetics and structure formation of ZrO2 thin films in chloride-based atomic layer deposition process.* Thin Solid Films, 2002. **408**(1-2): p. 97-103.
82. H. Nohira, W. Tsai, W. Besling, et al., *Characterization of ALCVD-Al2O3 and ZrO2 layer using X-ray photoelectron spectroscopy.* Journal of Non-Crystalline Solids, 2002. **303**(1): p. 83-87.
83. A. Rahtu and M. Ritala, *Reaction mechanism studies on the zirconium chloride-water atomic layer deposition process.* Journal of Materials Chemistry, 2002. **12**(5): p. 1484-1489.
84. S. Ferrari, G. Scarel, C. Wiemer, et al., *Chlorine mobility during annealing in N-2 in ZrO2 and HfO2 films grown by atomic layer deposition.* Journal of Applied Physics, 2002. **92**(12): p. 7675-7677.
85. C. Zhao, G. Roebben, H. Bender, et al., *In situ crystallisation in ZrO2 thin films during high temperature X-ray diffraction.* Microelectronics Reliability, 2001. **41**(7): p. 995-998.
86. W.F.A. Besling, E. Young, T. Conard, et al., *Characterisation of ALCVD Al2O3-ZrO2 nanolaminates, link between electrical and structural properties.* Journal of Non-Crystalline Solids, 2002. **303**(1): p. 123-133.

87. K. Kukli, K. Forsgren, M. Ritala, et al., *Dielectric properties of zirconium oxide grown by atomic layer deposition from iodide precursor.* Journal of the Electrochemical Society, 2001. **148**(12): p. F227-F232.
88. K. Kukli, K. Forsgren, J. Aarik, et al., *Atomic layer deposition of zirconium oxide from zirconium tetraiodide, water and hydrogen peroxide.* Journal of Crystal Growth, 2001. **231**(1-2): p. 262-272.
89. K. Kukli, M. Ritala, T. Uustare, et al., *Influence of thickness and growth temperature on the properties of zirconium oxide films grown by atomic layer deposition on silicon.* Thin Solid Films, 2002. **410**(1-2): p. 53-60.
90. K. Forsgren, J. Westlinder, J. Lu, et al., *Iodide-based atomic layer deposition of ZrO2: Aspects of phase stability and dielectric properties.* Chemical Vapor Deposition, 2002. **8**(3): p. 105-109.
91. K. Kukli, M. Ritala, M. Leskela, et al., *Atomic layer deposition of HfO2 thin films and nanolayered HfO2-Al2O3-Nb2O5 dielectrics.* Journal of Materials Science-Materials in Electronics, 2003. **14**(5-7): p. 361-367.
92. T. Conard, W. Vandervorst, J. Petry, et al., *TOF-SIMS as a rapid diagnostic tool to monitor the growth mode of thin (high k) films.* Applied Surface Science, 2003. **203**: p. 400-403.
93. N. Takahashi, N. Yoshii, S. Nonobe, et al., *Self-limiting growth of ZrO2 films on a Si(100) substrate using ZrCl4 and O-2 under atmospheric pressure.* Journal of Electronic Materials, 2003. **32**(10): p. 1107-1110.
94. N. Yoshii, N. Takahashi, T. Nakamura, et al., *Preparation of ZrO2 nano-films by an alternate reaction using ZrCl4 and O-2 under atmospheric pressure.* Electrochemical and Solid State Letters, 2002. **5**(9): p. C85-C86.
95. S.J. Yun, J.W. Lim, and J.H. Lee, *PEALD of zirconium oxide using tetrakis(ethylmethylamino)zirconium and oxygen.* Electrochemical and Solid State Letters, 2004. **7**(12): p. F81-F84.
96. Y. Kim, J. Koo, J.W. Han, et al., *Characteristics of ZrO2 gate dielectric deposited using Zr t-butoxide and Zr(NEt2)(4) precursors by plasma enhanced atomic layer deposition method.* Journal of Applied Physics, 2002. **92**(9): p. 5443-5447.
97. S.J. Yun, J.W. Lim, and J.H. Lee, *Effect of plasma on characteristics of zirconium oxide films deposited by plasma-enhanced atomic layer deposition.* Electrochemical and Solid State Letters, 2005. **8**(11): p. F47-F50.
98. J.Y. Kim, S.H. Kim, H. Seo, et al., *Deposition and plasma measurements of Zr-oxide films with low impurity concentrations by remote PEALD.* Electrochemical and Solid State Letters, 2005. **8**(3): p. G82-G84.
99. S.C. Ha, E. Choi, S.H. Kim, et al., *Influence of oxidant source on the property of atomic layer deposited Al2O3 on hydrogen-terminated Si substrate.* Thin Solid Films, 2005. **476**(2): p. 252-257.
100. E.P. Gusev, E. Cartier, D.A. Buchanan, et al., *Ultrathin high-K metal oxides on silicon: processing, characterization and integration issues.* Microelectronic Engineering, 2001. **59**(1-4): p. 341-349.
101. C.S. Park, N. Moumen, J.H. Sim, et al., *Performance of HfO2/TiN gate stacks with in situ grown and O-3 chemical interfacial oxide layers.* Applied Physics Letters, 2005. **87**(25): p. -.

102. M.L. Green, A.J. Allen, X. Li, et al., *Nucleation of atomic-layer-deposited HfO2 films, and evolution of their microstructure, studied by grazing incidence small angle x-ray scattering using synchrotron radiation.* Applied Physics Letters, 2006. **88**(3): p. -.
103. X.Y. Liu, S. Ramanathan, A. Longdergan, et al., *AID of hafnium oxide thin film from tetrakis(ethylmethylamino)hafnium and ozone.* Journal of the Electrochemical Society, 2005. **152**(3): p. G213-G219.
104. Y. Senzaki, S. Park, H. Chatham, et al., *Atomic layer deposition of hafnium oxide and hafnium silicate thin films using liquid precursors and ozone.* Journal of Vacuum Science and Technology A, 2004. **22**(4): p. 1175-1181.
105. M.J. Cho, D.S. Jeong, J. Park, et al., *Comparison between atomic-layer-deposited HfO2 films using O-3 or H2O oxidant and Hf[N(CH3)(2)](4) precursor.* Applied Physics Letters, 2004. **85**(24): p. 5953-5955.
106. J. Park, M. Cho, S.K. Kim, et al., *Influence of the oxygen concentration of atomic-layer-deposited HfO2 films on the dielectric property and interface trap density.* Applied Physics Letters, 2005. **86**(11): p. -.
107. S.A. VanSlyke, C.H. Chen, and C.W. Tang, *Organic electroluminescent devices with improved stability.* Applied Physics Letters, 1996. **69**(15): p. 2160-2162.
108. J. McElvain, H. Antoniadis, M.R. Hueschen, et al., *Formation and growth of black spots in organic light-emitting diodes.* Journal of Applied Physics, 1996. **80**(10): p. 6002-6007.
109. J.D. Affinito, M.E. Gross, C.A. Coronado, et al., *A new method for fabricating transparent barrier layers.* Thin Solid Films, 1996. **291**: p. 63-67.
110. F. J. H. van Assche, R. T. Vangheluwe, J. W. C. Maes, et al., Digest of Technical Papers, 2004. **XXXV**: p. 696.
111. A.P. Ghosh, L.J. Gerenser, C.M. Jarman, et al., *Thin-film encapsulation of organic light-emitting devices.* Applied Physics Letters, 2005. **86**(22): p. -.

Chapter 5 High-k/Ge MOS Capacitors

In this work, ALD of high-k dielectrics have been deposited on Ge with various surface treatments including sulfur passivation as described above. The interfacial properties are investigated using electrical characterization techniques. A brief introduction to capacitance-voltage measurement methods will be presented along with a few selected results from our work that demonstrate the improvements of MOS devices due to our cleaning and passivation methods.

Section 5.1 C-V Measurements

Electrical characterization is an important part of gate stack research. Because of the simplicity of operation and informative results, capacitance-voltage measurements (CV) are one of the most popular methods to screen potential dielectric and metal gate candidate materials [1]. This method is rather straightforward and requires only a simple measurement.

5.1.1 Energy Band Diagrams of MOS Stacks and Flat-Band Voltage

C-V measurements require a capacitor, which is equivalent to the gate stack part of a MOSFET. Figure 5-1 shows the band diagram of an ideal MOS structure on a p-type semiconductor substrate. The work function of the metal ϕ_m is the energy required for an electron inside the metal to move from the Fermi level to the vacuum level. The work function of the semiconductor, ϕ_s, is

determined by the electron affinity, χ, the band gap, E_g, and the Fermi potential ψ_B:

$$q\phi_s = \chi - \frac{1}{2}E_g + q\psi_B$$

The Fermi potential depends on the ratio of the doping density, N_a, and the intrinsic carrier density, n_i:

$$\psi_B = k_B T \ln\frac{N_a}{n_i}$$

Assume that the two work functions are the same in this ideal MOS structure: $\phi_{ms} \equiv \phi_m - \phi_s = 0$. The energy band diagram of the ideal MOS capacitor at equilibrium is shown in Figure 5-1.

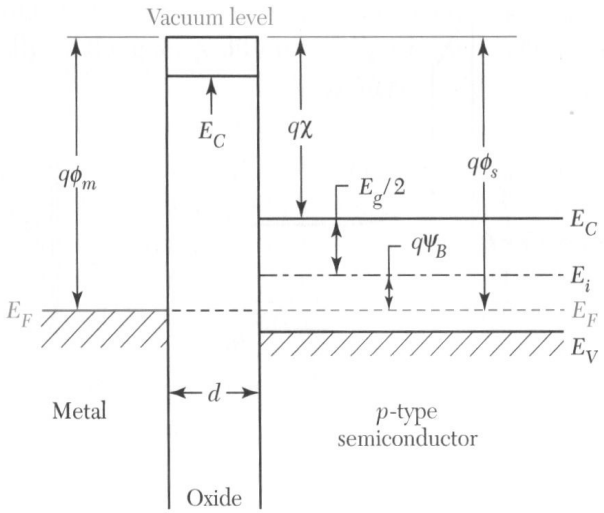


Figure 5-1: Energy band diagram of an ideal MOS capacitor [1].

When an ideal MOS capacitor is biased, several different cases exist at the semiconductor surface (Figure 5-3). Consider a p-type semiconductor; when a negative voltage is applied to the metal gate, the band bending causes an accumulation of majority p-type carriers and negative surface potential ψ_S near

the semiconductor surface. This is the accumulation case. When a small positive voltage is applied, the bands bend downward and the surface potential becomes more positive. This is called the depletion case because the majority carriers are depleted. Further increasing of the gate voltage in the positive direction causes the bands to bend even more and the charge of the minority and majority carriers at the surface switches. The surface becomes “inverted” with electrons accumulating near the interface; this is the inversion case.

Theoretically, the potential, $\psi_p(x)$, with respect to the bulk of the p-type semiconductor, together with the space-charge density, Q_S, can be obtained by solving the one-dimensional Poisson equation [1]:

$$\frac{d^2\psi_p(x)}{dx^2} = -\frac{\rho(x)}{\varepsilon_S}$$

At the surface of the semiconductor, ψ_S is the surface potential ($\psi_S \equiv \psi_p(0)$) and it depends only on the properties of the semiconductors (band gap, dielectric constant and doping level). Figure 5-2 shows a typical variation of the space-charge density in a semiconductor as a function of the surface potential: $Q_S(\psi_S)$ for a p-type Ge with $N_A = 2.5 \times 10^{22}$ cm^{-3} at room temperature. Note that the exponential term $\sim\exp(-q\,\psi_S/2k_BT)$ dominates in both the accumulation and the strong inversion cases, and the space-charge density, Q_S, for small positive surface potential increases as $\sim\sqrt{\psi_S}$. This is directly related to the voltage-dependent semiconductor capacitance:

$$C_S = \frac{dQ_S}{d\psi_S}$$

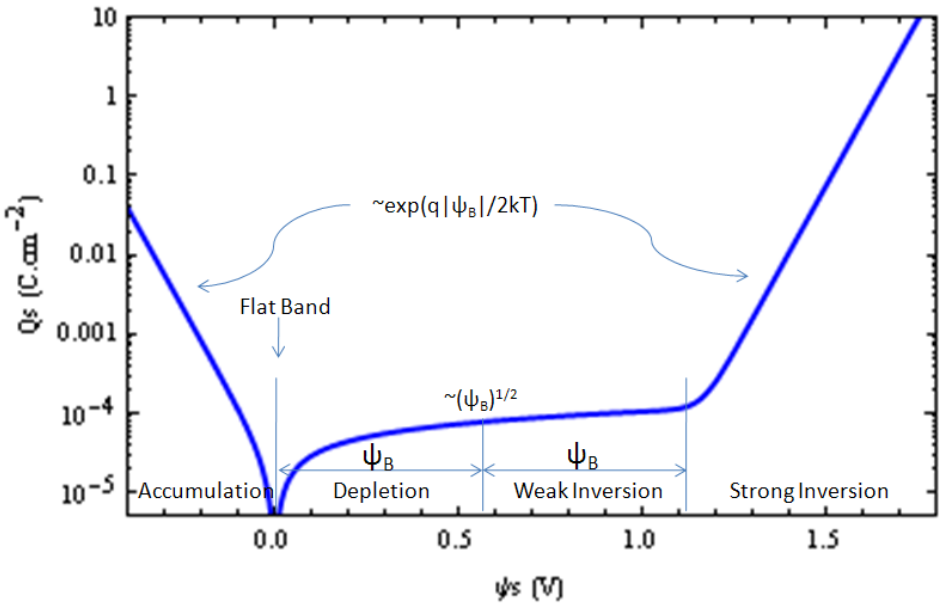


Figure 5-2: Space-charge density as a function of the surface potential for p-type Ge with N_A=2.5x10^{22} cm^{-3} at room temperature.

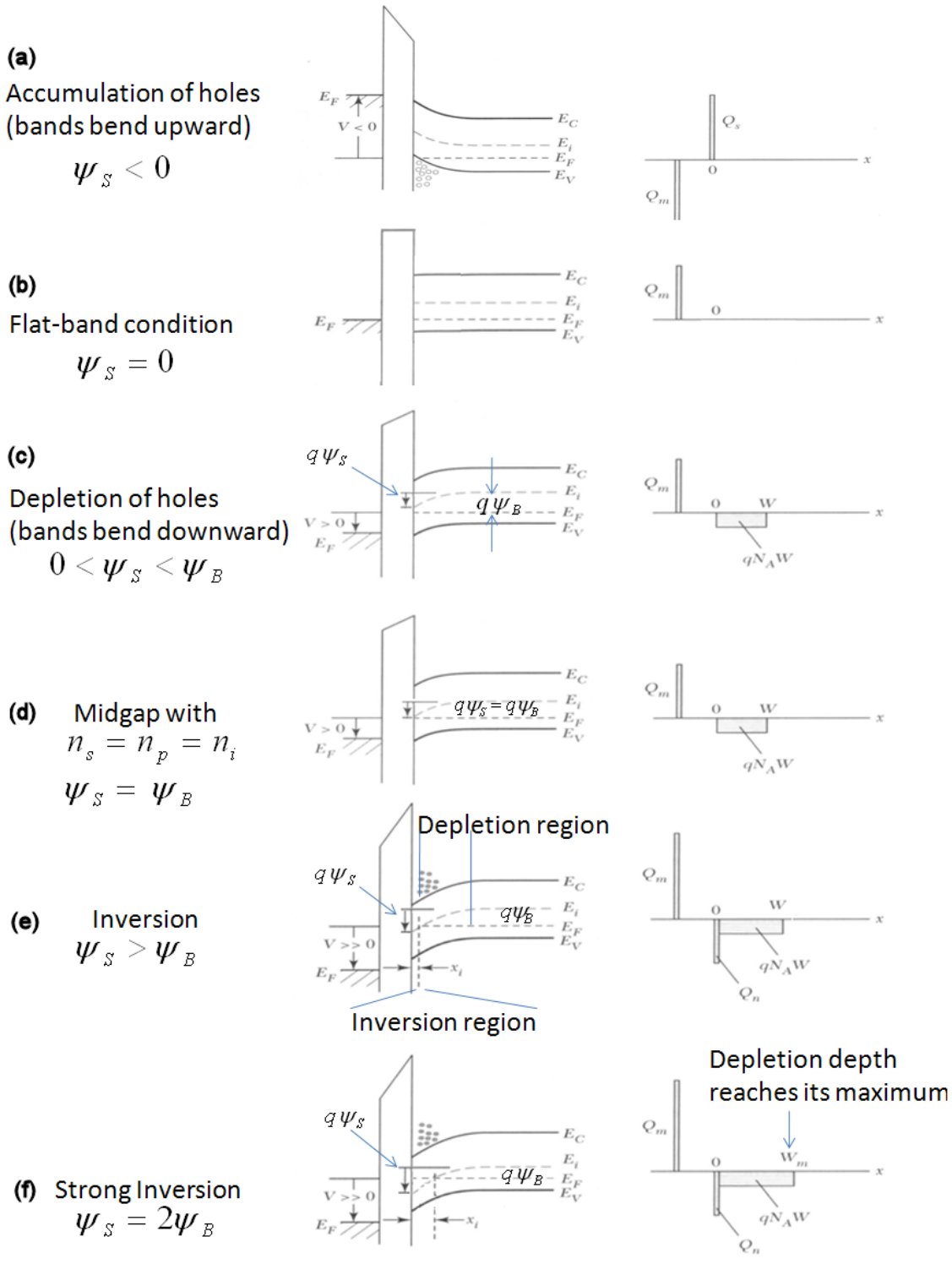


Figure 5-3: Band diagrams for an ideal p-substrate MOS structure in different surface-charge conditions (adapted from [1-3]).

When dealing with practical MOS systems, one needs to consider the effects of real surfaces. First, there is a non-zero work function difference resulting from the choice of the metal and the semiconductor as well as the doping level of the semiconductor. Second, there are charges within the oxide and at the oxide-semiconductor interface.

In the case of a non-zero, ϕ_{ms}, the band diagram at equilibrium has a tilt in the oxide conduction band in order to align the Fermi levels shown in Figure 5-4a and Figure 5-4b. As a result, the bands bend near the semiconductor surface to accommodate the work function difference. In order to reach the flat-band condition in which the surface potential, ψ_s, on the top of the semiconductor vanishes, a bias is required on the gate (Figure 5-4c). This bias is the flat-band voltage $V_{FB} = \phi_{ms}$.

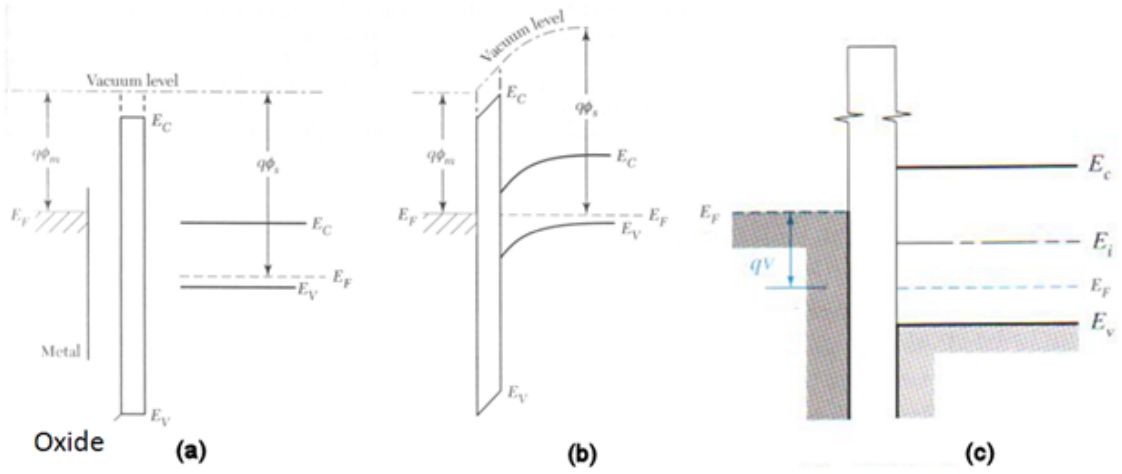


Figure 5-4: Band diagrams of MOS (a) at separation, (b) at equilibrium and (c) in flat-band condition [3].

The equilibrium MOS structure is also affected by the existence of charges in the insulator and at the interface between the oxide and semiconductor (Figure 5-5). In earlier studies [1], the charges inside the oxide layer were classified into (1) fixed oxide charges at or near the interface which are immobile under an external electric field, (2) oxide trapped charges distributed inside the oxide layer, and (3) mobile ionic charges such as sodium ions. In the case of ultrathin oxide films, this classification needs to be revised and currently there are still numerous studies on this issue. For simplicity, one can include all of the charges inside the oxide in Q_{ox}.

The interface trapped charge, Q_{it}, located in the high-k/semiconductor interface, can be either positive or negative and are electrically active due to interactions with the substrate. Studies have shown that the existence of the interface charges, Q_{it}, within the forbidden gap results from the interruption of the periodic lattice structure by impurities and defects in the interface [4-6]. With the assumption that every interface has both acceptor and donor interface traps within the forbidden-gap energies and the interface trapping levels are distributed with an equivalent interface state density, D_{it}, with an neutral level, E_0 (the so-called charge neutrality level, CNL) above which the states are of acceptor type and below which are of donor type, then the interface trapped charges can be calculated by

$$Q_{it} = q\int_{E_F}^{E_0} D_{it}\, dE = -q\int_{E_0}^{E_F} D_{it}\, dE$$

Even on a clean surface in an UHV system, Q_{it} can be very high. Proper surface passivation and post deposition annealing can help reduce Q_{it}.

The effective trapped charge, Q_i, is then defined as the sum of various oxide and interface charges ($Q_i = Q_{ox} + Q_{it}$) and it shifts the flat-band voltage:

$$V_{FB} = \phi_{ms} - \frac{Q_i}{C_{ox}}$$

where C_{ox} is the oxide capacitance. The next section will explain how to obtain V_{FB} experimentally from a C-V measurement.

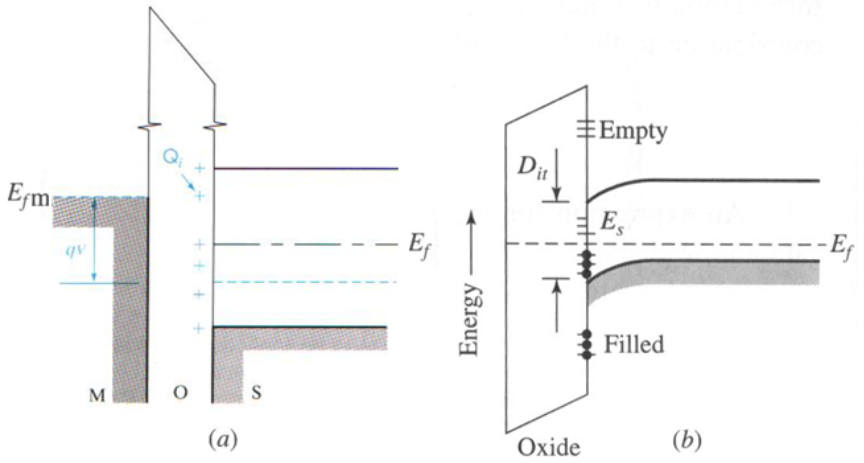


Figure 5-5: (a) Charges represented as a sheet of effective charge [2]; (b) interface traps [7].

5.1.2 C-V Curves of MOS Capacitors and Threshold Voltage

When the gate voltage is varied, the MOS capacitance varies due to the accumulation, depletion and inversion of charge carriers in the semiconductor substrate near the dielectric interface. The equivalent capacitance of a MOS capacitor can be regarded as a combination of a fixed, voltage-independent

oxide capacitance and a contribution from the semiconductor substrate. In a practical MOS system, trapped charges also contribute to this voltage-dependent capacitance in the inversion region. The equivalent circuits are shown in Figure 5-6 to illustrate this idea.

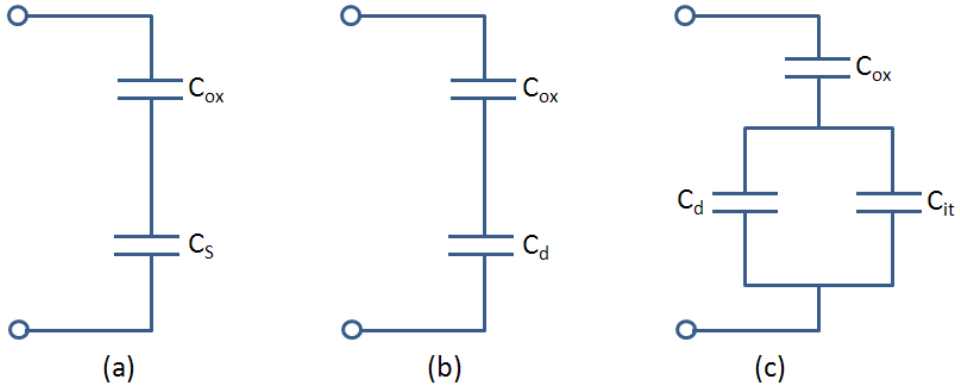


Figure 5-6: Equivalent circuits including interface-trapped effects (a), at high (b) and low frequency (c).

In the accumulation case, the semiconductor capacitance, C_S, is very high because the slope of the space-charge density, Q_S, versus ψ_S plot is very steep as shown in Figure 5-2. Hence, the series capacitance in the accumulation case is just the oxide capacitance, C_{ox} (Figure 5-6a). The capacitance extreme, C_{ox}, in the accumulation case from a C-V measurement can be used to calculate the dielectric constant of the oxide if the physical thickness d of the oxide is obtained by another method like RBS:

$$C_{ox} = \frac{\varepsilon_{ox}}{d}$$

As the gate voltage becomes less negative, the semiconductor surface is depleted. The depletion-layer capacitance, C_d, is added in series with C_{ox} (Figure 5-6b):

$$\frac{1}{C} = \frac{1}{C_{ox}} + \frac{1}{C_d}$$

$$C_d = \frac{\varepsilon_S}{W}$$

where W is the depletion width in the semiconductor substrate and is given by

$$W = 2\sqrt{\frac{\varepsilon_S \psi_S}{qN_a}}$$

In the depletion region, the MOS capacitance decreases as $1/\sqrt{\psi_S}$, while the depletion width W grows with increasing gate voltage across the capacitor. When the flat-band condition is reached, the MOS capacitance, C_{FB}, is given by:

$$\frac{1}{C_{FB}} = \frac{1}{C_{ox}} + \frac{1}{C_{Debye}}$$

where C_{Debye} is the Debye length capacitance of the substrate and is determined by the extrinsic Debye length, L_D:

$$C_{Debye} = \frac{\varepsilon_s}{L_D}$$

$$L_D = \sqrt{\frac{\varepsilon_s K_B T}{q^2 N_a}}$$

While the gate voltage becomes more positive than the flat-band voltage, the MOS capacitance keeps decreasing until strong inversion is reached at the

threshold voltage, V_T. At this point, the surface potential is twice the Fermi potential:

$$\psi_S(inv) = 2\psi_B$$

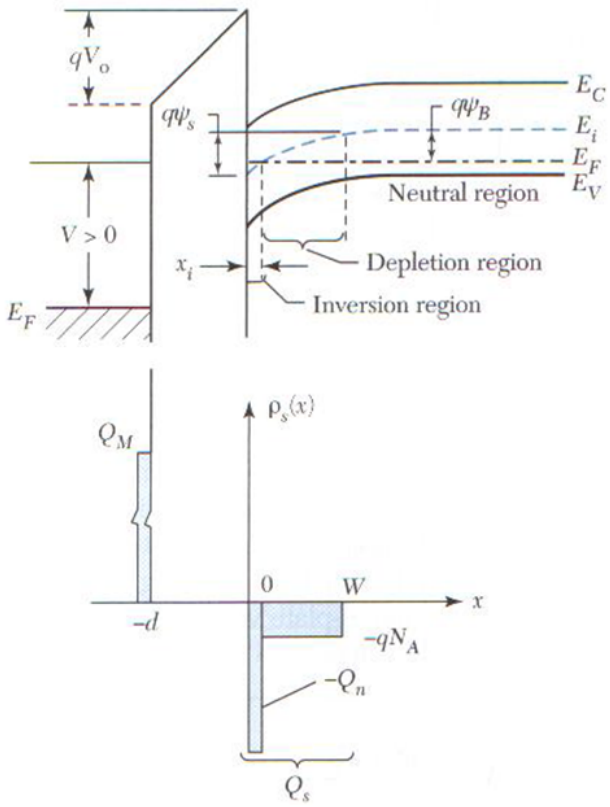


Figure 5-7: Band diagram and distribution of charge density in inversion [1, 3].

Figure 5-7 shows the details of the energy bands and the distribution of charges. The inversion charge Q_n is negligible compared to the depletion charge, Q_d, in the inversion case, so the total surface charge, Q_S, is mostly due to the depletion charge:

$$Q_S = Q_n + Q_d \approx Q_d = -qN_aW_D$$

The threshold voltage, V_T, required for strong inversion, using the above equations, is then given by:

$$V_T = V_{FB} + \psi_s(inv) - \frac{Q_s}{C_{ox}} \approx V_{FB} + 2\psi_B - \frac{Q_d}{C_{ox}}$$

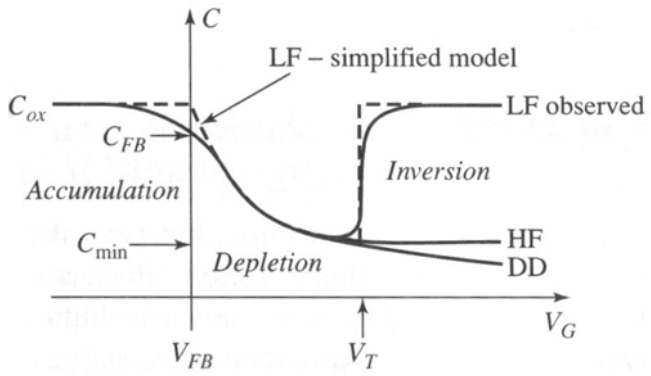


Figure 5-8: C-V curve for an ideal p-substrate MOS capacitor at high (HF) and low (LF) frequency [7].

Further increases in the voltage beyond the threshold voltage, V_T, result in strong inversion with a maximum depletion width, W_D. The small signal capacitance now depends on the frequency at which the measurement is made. In a high-frequency measurement, a small-signal measuring voltage at high frequency (100 kHz in this work) is applied. The gate voltage varies faster than the generation-recombination rate of the minority carriers in the inversion layer. The charge in the inversion layer cannot change in response, so it does not contribute to the capacitance. Hence the MOS capacitance remains at its minimum, C_{min}, corresponding to the minimum depletion-layer capacitance, $C_{d\,min}$, resulting from the maximum depletion width W_D (Figure 5-7):

$$\frac{1}{C_{min}} = \frac{1}{C_{ox}} + \frac{1}{C_{d\,min}}$$

This capacitive behavior is shown as the high frequency “HF” curve in Figure 5-8. $C_{d\,min}$ extracted from a high-frequency C-V measurement can be used to determine the value of the depletion width maximum, W_m, the substrate doping, N_a, the Debye length capacitance, L_D, flat-band capacitance, C_{FB}, and the flat-band voltage, V_{FB} .

If the C-V measurements are done at low frequency, the MOS capacitance in the strong inversion case at low-frequency will become very different from that obtained by high-frequency measurements. Because the gate voltage changes slowly at low frequency, there is enough time for minority carriers to be generated in the bulk, drift across the depletion region to the inversion layer, or go back to the substrate and recombine. The charge in the inversion layer also contributes to the capacitance. In an ideal MOS capacitor, this is the space charge, Q_S, induced by the electric field. Now the semiconductor capacitance $C_S = dQ_S/d\psi_S$ is very large in the strong inversion case because the space-charge density grows exponentially (Figure 5-2). Again the MOS series capacitance at low frequency is C_{ox}. The low frequency “LF” curve in Figure 5-8 shows C_{ox} in the strong inversion region. In a practical MOS system, the interface charge also contributes to the capacitance in the strong inversion case. The equivalent circuit is shown in Figure 5-6c.

The deep-depletion region is shown as the “DD” curve in Figure 5-8. This corresponds to the experimental situation in which both the gate voltage and the small-signal measuring voltage vary too rapidly to form an inversion layer in the

surface depletion region. As a result, the depletion layer becomes wider than W_D and there is no capacitance minimum in deep depletion.

Section 5.2 Effects of Trapped Charges on C-V Curves

One goal of this work is to minimize the trapped charges using the sulfur passivation of Ge before the deposition of high-k dielectrics. As mentioned in the previous section, there are two sources of the trapped charges: the trapped charges in the oxide layer and the interface traps.

5.2.1 Shifts of Flat-Band Voltage and Hysteresis of C-V Curves

In an ideal MOS capacitor without trapped charges, the flat-band voltage is given by the work function difference of the metal and the semiconductor, ϕ_{ms}, which shifts the flat-band voltage without distortion (the dashed line in Figure 5-9).

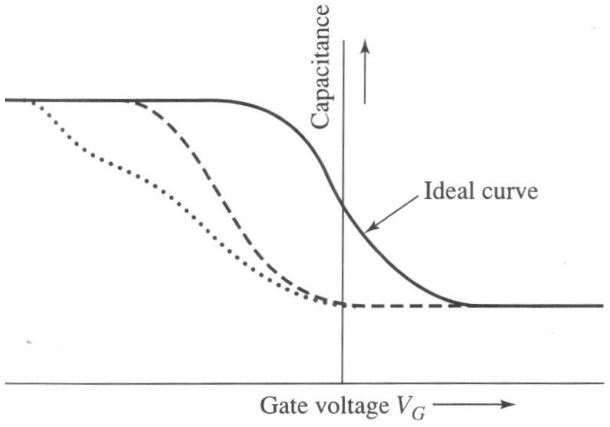


Figure 5-9: C-V curve with nonzero work function difference (dashed) and trapped charges (dotted) [7].

However, the C-V curve is shifted as well as distorted in the presence of the trapped charges (the dotted line in Figure 5-9). The flat-band voltage can be extracted from the C-V curve and compared to an ideal C-V curve. This shift is directly related to the amount of the effective trapped charge, Q_i, by:

$$\Delta V_{FB} = -\frac{Q_i}{C_{ox}}$$

In practical MOS systems, C-V measurements might exhibit hysteresis effects as shown in Figure 5-10. These measurements are made when the gate voltage is swept back and forth with a very low frequency of a triangular wave (~1Hz) and a high-frequency ac measurement (1kHz or higher). The hysteresis can help differentiate between two common non-ideal behavior patterns: (1) the field-aided movement of the positive ions in the oxide layer, and (2) the trapping of free carriers from the channel in traps at the oxide/semiconductor interface Q_{it}.

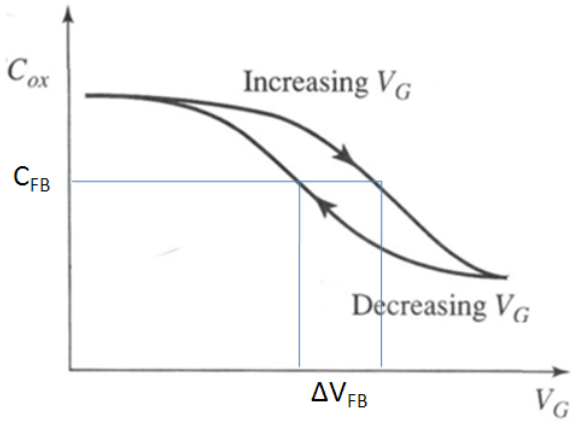


Figure 5-10: Hysteresis of a C-V curve [7].

5.2.2 Determination of Interface Traps

There are several methods to determine the interface state density, D_{it}: (1) comparison of the measured C-V curve at low frequency with the theoretical ideal curve [8]; (2) comparison of the measured C-V curve at high frequency with the theoretical ideal curve [9]; and (3) comparison of measurements of the C-V curves at low and high frequency [2, 10].

In this work, the high-low-frequency capacitance method is used because it does not require complicated theoretical calculations for comparison. From the C-V curves, C_{HF} and C_{LF} can be extracted at threshold voltage as shown in Figure 5-11 and can be used in the calculation of D_{it} [2]:

$$D_{it} = \frac{1}{q^2}\left(\frac{C_{ox}C_{LF}}{C_{ox} - C_{LF}} - \frac{C_{ox}C_{ox}}{C_{ox} - C_{HF}}\right)$$

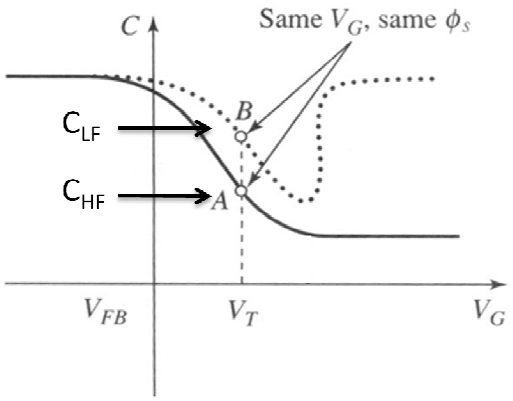


Figure 5-11: C-V curves at high (solid line) and low (dotted line) frequencies [7].

Section 5.3 Experimental Results

The Ge-based MOS capacitors studied in this work were fabricated on p-type Ge(100) wafers with $N_A = 2.5 \times 10^{22}$ cm^{-3}. The Ge surface pretreatments included degreasing, wet chemical cleaning (HF etches and/or H_2SO_4/H_2O_2 oxidation) and optional passivation with sulfur using $(NH_4)_2S$ solution as shown in Section 5.3. A thin layer of HfO_2 was deposited in our home-made ALD system with $Hf(NEtMe)_4$ and DIW as precursors. The film growth conditions are given in Section 4.5. The physical film thickness of the HfO_2 layer has been determined by RBS to be 4.0 nm after 50 ALD cycles. An array of 200 nm-thick Au dots (100 μm in diameter) as metal gates were e-beam sputtered onto the high-k layer. All samples were annealed at 500 ℃ for 30 seconds befo re the C-V measurements. The sweeping dc bias is applied on the gate from -2 to 2 volts with a small ac signal (20 mV) at high and low frequencies (1M and 100k Hz). Figure 5-12 shows

the stack structures of the Ge-based MOS capacitors and the setup of the C-V measurement.

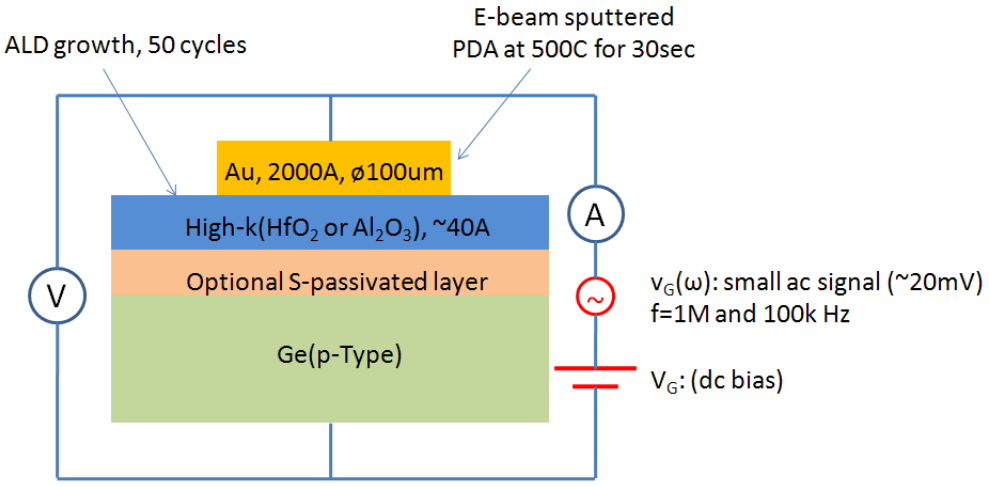


Figure 5-12: Schematic drawing of the C-V measurement setup.

5.3.1 HfO_2/Ge

C-V measurements have been performed on Au/HfO_2/p-Ge(100) MOS capacitors with different surface treatments on the Ge substrates. Figure 5-13 shows the C-V curves of such a sample with an HF-last Ge substrate. Comparing the measurements with the calculated ideal C-V curve, the effective trapped charge, Q_i, can be obtained as shown in Section 5.2.1 and has a value of 4×10^{13} $e^{-1}cm^{-2}$. After the flat-band capacitance, C_{FB}, is determined, the amount of the offset of the corresponding voltages, ΔV_{FB_HS}, from the dual sweep C-V curve (Figure 5-10) can be used as a quantitative measure of how big the hysteresis is. For this sample, it is 0.31 V. The value of the interface state density, D_{it}, has been extracted using the method in Section 5.2.2 and has a

value of 3.80×10^{12} cm^{-2}/eV. With such a large effective charge and big C-V hysteresis, this MOS capacitor is unacceptable, in this condition, due to its electrical performance.

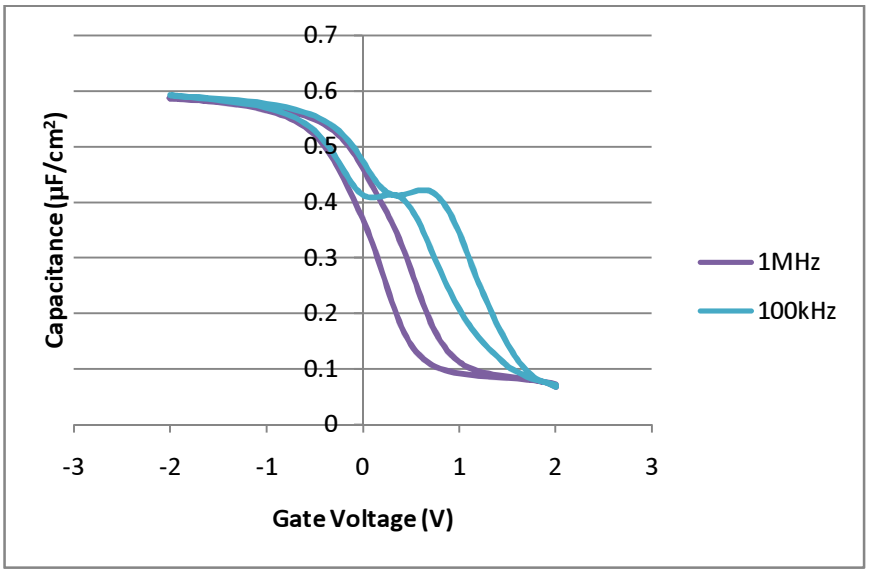


Figure 5-13: C-V curves of a Au dot capacitor with 4 nm HfO_2 on HF-last p-Ge(100).

We now compare the electrical characteristics of Au/HfO_2/p-Ge(100) MOS capacitors fabricated with and without the sulfur passivation. Figure 5-14 shows the C-V curves of a Au/HfO_2/p-Ge(100) MOS capacitor on a sulfur-passivated Ge substrate. Comparing with Figure 5-13, the C-V hysteresis is smaller ($\Delta V_{FB_HS} = 0.29$ V) and the C-V curve is less distorted. This implies that the amount of the effective trapped charge is smaller ($Q_i = 4.17 \times 10^{12}$ e^{-1}cm^{-2}). The value of the interface state density, D_{it}, is 1.67×10^{11} cm^{-2}/eV. This great reduction on D_{it} is due to the sulfur passivation which terminates the dangling bonds on Ge surfaces [11].

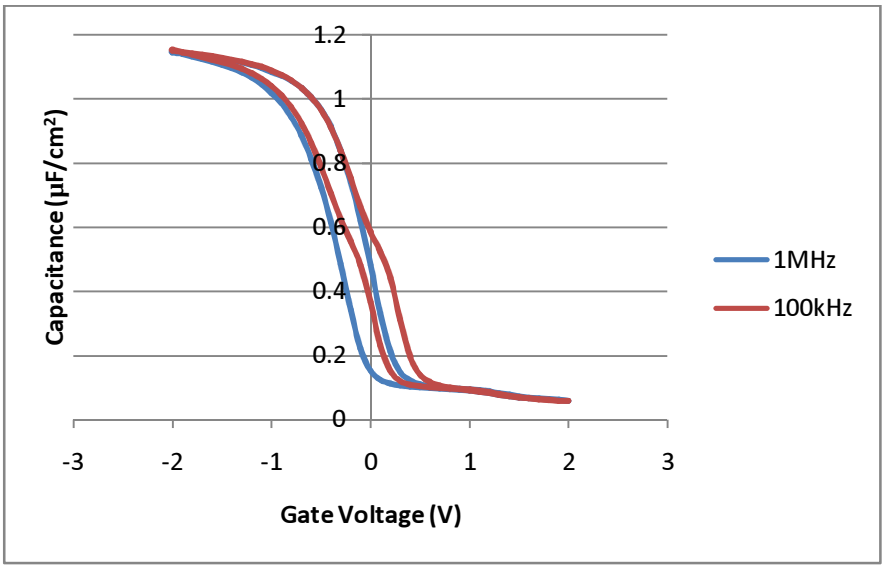


Figure 5-14: C-V curves of a Au dot capacitor with 4 nm HfO_2 on HF/DIW/H_2O_2-treated S-passivated p-Ge(100).

Figure 5-15 shows the C-V curves of a Au/HfO_2/p-Ge(100) MOS capacitor on a sulfur-passivated Ge substrate. The degreased Ge substrate was first cleaned using the H_2SO_4/H_2O_2 oxidation method. Before being passivated in $(NH_4)_2S$ solution, the substrate was etched by HF to remove the chemical oxide formed in the previous step. Both the C-V hysteresis and the amount of the effective trapped charge are further reduced ($\Delta V_{FB_HS} = 0.22$ V and $Q_i = 3.56 \times 10^{12}$ $e^{-1}cm^{-2}$). Comparing this to the C-V curves from the previous two samples in Figure 5-13 and Figure 5-14, the shoulder due to the distortion becomes less noticeable. The value of the interface state density, D_{it}, is 8.91×10^{10} cm^{-2}/eV.

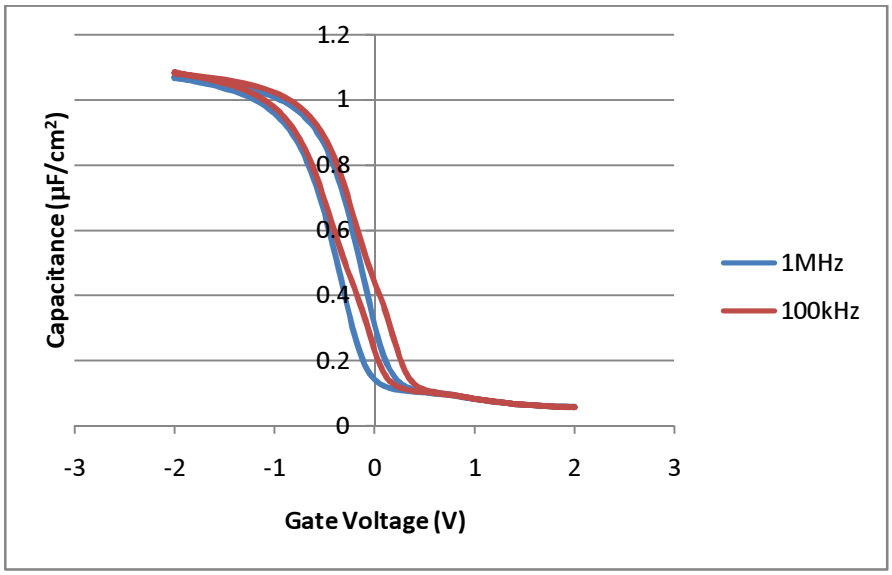


Figure 5-15: C-V curves of a Au dot capacitor with 4 nm HfO_2 on H_2SO_4/H_2O_2 oxidized, HF-etched S-passivated p-Ge(100).

In Section 3.1, we have shown that using HF should be avoided in order to minimize the amount of hydrocarbons after the protective chemical oxide is formed on the Ge surface. Figure 5-16 shows the C-V curves of another Au/HfO_2/p-Ge(100) MOS capacitor. It is similar to the previous one, except that the HF etching step is omitted during the surface preparation (degreasing, H_2SO_4/H_2O_2 oxidation and sulfur passivation). Among these four samples, it has the smallest C-V hysteresis, the least amount of effective trapped charge ($\Delta V_{FB_HS} = 0.15$ V and $Q_i = 3.19 \times 10^{12}$ $e^{-1}cm^{-2}$) and the lowest value of interface state density D_{it} (6.23×10^{10} cm^{-2}/eV).

The values of Q_i, ΔV_{FB_HS} and D_{it} obtained from these samples are listed in Table 5-1 for easy comparison.

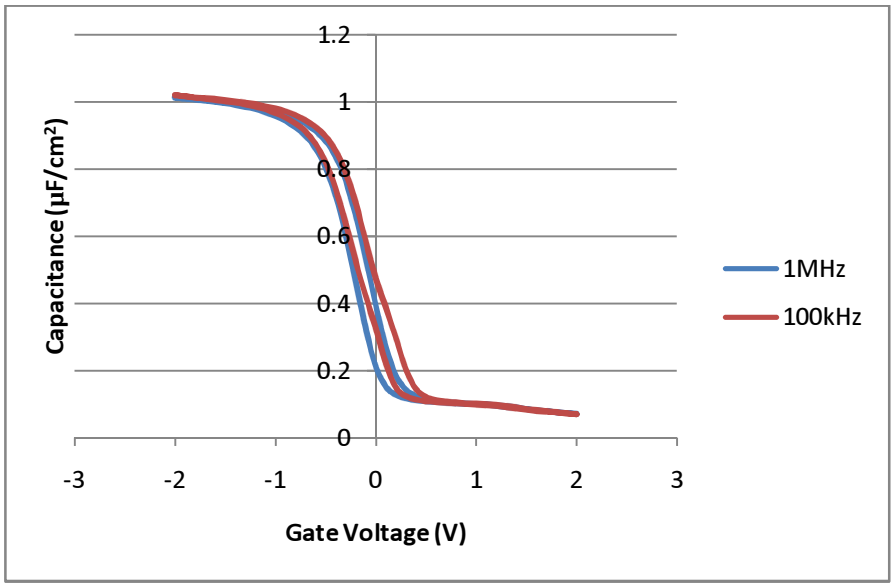


Figure 5-16: C-V curves of a Au dot capacitor with 4 nm HfO_2 on H_2SO_4/H_2O_2 oxidized, S-passivated p-Ge(100).

Cleaning	HF	HF/DIW/H_2O_2	H_2SO_4/H_2O_2 HF	H_2SO_4/H_2O_2
S-passivation	No	Yes	Yes	Yes
Q_i/e (cm^{-2})	$4.00x10^{13}$	$4.17x10^{12}$	$3.56x10^{12}$	$3.19x10^{12}$
Q_{HS}/e (cm^{-2})	$1.15x10^{13}$	$2.09x10^{12}$	$1.5x10^{12}$	$9.72x10^{11}$
ΔV_{FB_HS}(V)	0.31	0.29	0.22	0.15
D_{it} (eV^{-1} cm^{-2})	$3.80x10^{12}$	$1.66x10^{11}$	$8.91x10^{10}$	$6.23x10^{10}$

Table 5-1: Comparison of the C-V measurements on Au/HfO_2/p-Ge(100) capacitors.

Our results are significantly better than those reported in the literatures to date. Figure 5-17 shows the C-V curves from a Al dot capacitor with 7.7 nm HfO_2 on sulfur passivated n-Ge(100) from a recent study [12]. The minimum, extracted from their C-V measurement, is 2.4×10^{12} cm^{-2}/eV which is about 40 times larger than our best results (Table 5-1).

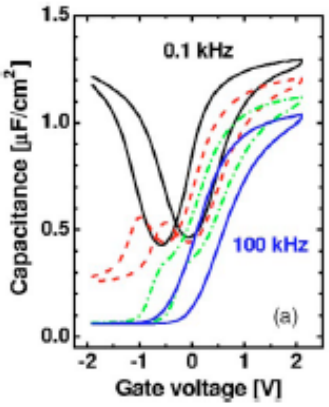


Figure 5-17: C-V curves of Al dot capacitors with 7.7 nm HfO_2 on S-passivated n-Ge(100) [12].

5.3.2 Al_2O_3/Ge

The improvement of the electrical properties due to the sulfur passivation was also observed on Ge-based MOS capacitors with Al_2O_3 as a dielectric. For comparison, ALD-grown Al_2O_3 was deposited on p-Ge(100) with and without a sulfur passivated layer. Figure 5-18 shows the C-V curves obtained from such two Au/Al_2O_3/p-Ge(100) capacitors. The capacitor with the sulfur passivation has smaller C-V hysteresis and lower D_{it} than the one without the sulfur passivation.

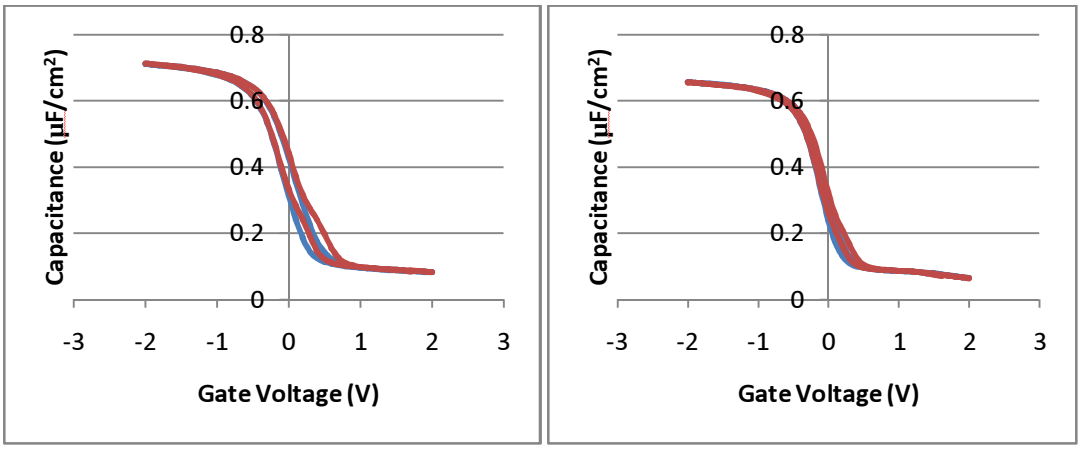


Figure 5-18: C-V curves of Au/Al_2O_3/p-Ge(100) with (right) and without (left) the sulfur passivation.

In summary, the C-V measurements show that the Ge-based MOS capacitors with the sulfur passivation exhibit lower D_{it} and smaller flat-band voltage shifts than the ones without the sulfur passivation. This indicates that sulfur passivation can efficiently reduce the trapped charge density and improve electrical properties. The same trend has been observed on capacitors with HfO_2 as well as Al_2O_3 as the high-k dielectric. Moreover, different wet chemical pretreatments of the Ge substrates affect the C-V characteristics differently. From our studies, the MOS capacitor on S-passivated Ge substrates which were cleaned with H_2SO_4/H_2O_2 oxidation without following HF etches gives the best electrical measurement results.

Section 5.4 Reference

1. S.M. Sze, *Physics of Semiconductor Devices*. 2nd ed. 1981, New York: Wiley.
2. B.G. Streetman and S.K. Banerjee, *Solid State Electronic Devices*. 6th ed. 2005: Prentice Hall.
3. R. Pierret, *Semiconductor Device Fundamentals*. 2003: Pearson Higher Education.
4. I. Tamm, Phys. Z. Sowjetunion, 1933. **1**: p. 733.
5. W. Shockley, *On the surfaces states associated with a periodic potential.* Physics Review, 1939. **56**: p. 317.
6. E.H. Nicollian and J.R. Brews, *MOS Physics and Technology*. 1982, New York: Wiley.
7. R.S. Muller, T.I. Kamins, and M. Chan, *Device Electronics for Integrated Circuits*. 3rd ed. 2002: John Wiley & Sons.
8. L.M. Terman, *An investigation of surface states at a silicon/silicon dioxide interface employing metal-oxide-silicon diodes.* Solid-State Electron, 1962. **5**: p. 285.
9. C.N. Berglund, *Surface state at steam-grown silicon-silicon dioxide interface.* IEEE Transactions on Electron Devices, 1966. **ED-13**: p. 701.
10. R. Castagne and A. Vapaolle, *Description of the SiO2-Si interface properties by means of very low frequency MOS capacitance measurements.* Surface Science, 1971. **28**: p. 157.
11. T. Maeda, S. Takagi, T. Ohnishi, et al., *Sulfur passivation of Ge (001) surfaces and its effects on Schottky barrier contact.* Materials Science in Semiconductor Processing, 2006. **9**(4-5): p. 706-710.
12. M.M. Frank, S.J. Koester, M. Copel, et al., *Hafnium oxide gate dielectrics on sulfur-passivated germanium.* Applied Physics Letters, 2006. **89**(11): p. -.

Chapter 6 Conclusion

Scaling CMOS devices is key to the development of semiconductor technology. However, further reduction in the thickness of the traditional SiO_2 dielectric, now ~1 nm, would result in a dramatic increase in the leakage current and hence degrade the device performance and increasing power consumption well beyond what is acceptable. High-k dielectric materials like HfO_2 and Al_2O_3 have been examined as replacements to SiO_2 and are beginning to appear in commercial devices just as this thesis work is finished. With SiO_2 on the way out, the need for Si also becomes a hindrance, and other higher performance semiconductor are being suggested, with Ge showing some advantages such as higher mobility relative to Si.

Because of the low thermal and chemical stability of Ge oxides, surface cleaning and preparation on germanium is not as straightforward as it is for Si. In this work, different wet-chemical cleaning methods on Ge substrates have been studied. Unfortunately, none of them appear to fully remove all the hydrocarbon and germanium carbides from the surface. By chemical oxidation, we can convert these into other chemical species, which are more easily removed. This approach seems to be a very promising solution. We have demonstrated that H_2SO_4/H_2O_2 oxidation not only can greatly reduce the amount of the hydrocarbons and germanium carbides, but it can also form a protective oxide to prevent the surface from further contamination in ambient conditions. After the

chemical oxide is formed, we also found that HF etches should be avoided in order to reduce the amount of carbon remaining or adsorbing on the surface.

Surface passivation is another crucial step for the success of the Ge-based MOS devices. In this work, two different passivation chemistries (with hydrogen and sulfur) have been studied and compared. S-passivated Ge surfaces prepared in hot $(NH_4)_2S$ solution are more stable than H-terminated Ge surfaces. We have demonstrated that the combination of H_2SO_4/H_2O_2 oxidation and the sulfur passivation with $(NH_4)_2S$ have produced a clean Ge surface with the least amount of carbons and Ge oxides.

Atomic layer deposition proves to be a very useful technique for the growth of ultra-thin high-k films. In our home-built ALD system, ALD-grown HfO_2 and Al_2O_3 have been deposited on Ge as well as other substrates including Si and glass. The physical thickness and the growth rate have been determined by RBS.

Combining our work of the wet-chemical cleaning, the surface passivation and ALD of high-k films, we are able to optimize the fabrication of novel Au/high-k/Ge-based MOS capacitors. The interfacial properties have been investigated using the electrical characterization techniques, including capacitance-voltage measurements. The trap state density and the effective trapped charge have been extracted from the results of the C-V measurements and have been used to compare the effects of different surface preparation on Ge substrates. A great improvement of MOS devices due to the sulfur passivation has been observed. The future work should be focus on the further reduction of trapped charges and

interface state density and improvement of high-k film quality in order to minimize leakage current and increase the MOS capacitance.

Curriculum Vista

Chien-Lan Hsueh

1997	B.S. in physics, National Tsing Hua University, Taiwan
1997-1998	Research assistant, National Synchrotron Radiation Research Center, Taiwan
2000	M.S. in physics, National Taiwan University, Taiwan
2008	Ph.D., Department of Physics and Astronomy, Rutgers, The State University of New Jersey.

Publications:

1. X.G. He, C.-L. Hsueh and J.Q. Shi, “Constraints on the phase gamma and new physics from B -> K pi decays”, Physical Review Letters 84 (1): 18-21 JAN 3 2000

2. J.B. Neaton, C.-L. Hsueh, and K.M. Rabe 2002, ”Enhanced polarization in strained BaTiO3 from first principles”, Materials Research Society (MRS) Proceedings 718: D10.26

3. M.M. Frank, H. Shang, S. Rivillon, F. Amy, C.-L. Hsueh, V. Paruchuri, R.T. Mo, M. Copel, E.P. Gusev, M.A. Gribelyuk, Y.J. Chabal, “High-kappa gate dielectrics on silicon and germanium: Impact of surface preparation”, Solid State Phenomena 103-104: 3-6 2005

4. E. Garfunkel, L. Goncharova, S. Rangan, C.-L. Hsueh, O. Celik, R. Bartynski and T. Gustafsson, “Interface Characaterization in Nanoelectronics", The E4 Symposium "High Dielectric Constant Materials and Gate Stack 5," of the 212th Meeting of the Electrochemical Society. Washington, DC. 2007